Magnetic and Transport Properties of Colossal Magnetoresistance Manganites and Magnetic Semiconductors

by

Wanjun Jiang

A Thesis
Submitted to the Faculty of Graduate Studies of
The University of Manitoba
in Partial Fulfilment of the Requirements
for the degree of

DOCTOR OF PHILOSOPHY

Department of Physics & Astronomy
University of Manitoba
Winnipeg, Manitoba, Canada

Abstract

The magnetic and transport properties of various doped manganites from the series $(La,Pr)_{1-x}(Ca,Ba)_xMnO_3$, and of the magnetic semiconductors $Fe_{0.8}Co_{0.2}Si$ and $Ga_{0.98}Mn_{0.02}As$, have been investigated.

In the manganites, the influence of doping on; (**i**) the evolution of the metal-insulator transition (MIT) with composition; (**ii**) the universality class of the magnetic critical behavior accompanying colossal magnetoresistance (CMR) in the vicinity of the MIT; (**iii**) the mechanisms underlying ferromagnetism across the MIT; and (**iv**) the correlation between a Griffiths-like phase and colossal magnetoresistance (CMR) has been investigated. Four different systems have been studied: $La_{1-x}Ca_xMnO_3$ ($0.18 \leq x \leq 0.27$), $La_{1-x}Ba_xMnO_3$ ($x \leq 0.33$), $(La_{1-y}Pr_y)_{0.7}Ca_{0.3}Mn^{16/18}O_3$ ($y \leq 0.85$), and $Pr_{1-x}Ca_xMnO_3$ ($x = 0.27, 0.29$). In $La_{1-x}Ca_xMnO_3$ ($0.18 \leq x \leq 0.27$), (magneto)resistance measurements narrow the compositionally modulated MIT to lie between $0.19 \leq x_c \leq 0.20$ in the series studied. Comparisons between the latter and magnetic data provide the first unequivocal demonstration that (**a**) the presence of a Griffiths-like phase does not guarantee CMR, while (**b**) nor are the appearance of such features a prerequisite for CMR. These data also reveal that (**c**) whereas continuous magnetic transitions occur for $0.18 \leq x \leq 0.25$, the universality class of these transitions belong to that of nearest neighbor 3-D Heisenberg model only for $x \leq 0.20$; beyond this composition, complications due to the emergence of a Griffiths-like phase occurs. In addition, (**d**) the

evolution of the MIT with composition supports the assertion that the dominant mechanism underlying ferromagnetism across the MIT changes from the ferromagnetic Super Exchange stabilized by orbital ordering in the insulating phase to Double Exchange in the orbitally disordered metallic regime. In $La_{1-x}Ba_xMnO_3$ ($x \leq 0.33$), a phase diagram is constructed to include the occurrence of a Griffiths-like phase, and comparisons with the random bond diluted ferromagnetic ±J Ising model are presented. In $(La_{1-y}Pr_y)_{0.7}Ca_{0.3}Mn^{16/18}O_3$ ($y \leq 0.85$), the origin of a Griffiths-like phase has been discussed in combination with previous neutron diffraction measurements, yielding a correlation between the emergence of such a phase and the relative volume fractions of the phase separated antiferromagnetic and ferromagnetic components. This correlation persists even when the recently estimated Double Exchange linked percolation threshold for manganites is exceeded. Finally in $Pr_{1-x}Ca_xMnO_3$ ($x = 0.27, 0.29$) the coexistence of ferromagnetism and insulating phases is discussed, and provides indirect support for the suggestion that the origin of ferromagnetism in the insulating regime is Super Exchange induced when Double Exchange is not dominant.

In the magnetic semiconductors $Fe_{0.8}Co_{0.2}Si$ and $Ga_{0.98}Mn_{0.02}As$, the scaling between magnetization and conductivity has been the subject of ongoing debate. In bulk polycrystalline $Fe_{0.8}Co_{0.2}Si$, a novel scaling between the anomalous Hall effect and the magnetization enables the anomalous Hall coefficient R_S to be accurately determined. In turn, this enables the universality class for the transition to ferromagnetism to be established independently from the anomalous Hall conductivity. In an epitaxial

(metallic) $Ga_{0.98}Mn_{0.02}As$ microstructure, the magnetization has been indirectly determined from the anomalous Hall effect. Subsequent analysis yields magnetic critical exponents consistent with the Mean-Field model, direct support for which had previously been lacking; the underlying interactions can indeed be treated within the framework of Landau Mean-Field theory. This in turn, validates the frequently adopted theoretical approach which predicts an intrinsic origin for the anomalous Hall effect in this system.

Acknowledgements

I would like to express the deepest appreciation to my supervisor, Dr. G. Williams for the free but the inspiring working environment which he had created, which benefited me in many ways.

The invaluable assistances from Dr. X. Z. Zhou, Mr. G. Roy, Dr. H. P. Kunkel are appreciated. Thanks are also due to Dr. Y. S. Gui, Dr. C.-M. Hu, Dr. R.-M. Roshko for lots of meaningful discussions and suggestions made during this study. The help from the main office, Ms. W. Klassen, Ms. S. Beshta and Ms. R. Baluta is gratefully acknowledged. I also need to thank Dr. Pomjakushin for sharing the data, Dr. Page for the access to the diamond wire saw.

Finally, I want to thank the continual support from my family.

List of Figures

List of Tables

List of Copyrighted Materials

Table of Content

Chapter 1

Introduction

Transition metal and related compounds have been extensively studied over the past several decades, particularly their structural, thermal, magnetic and transport properties. Such investigations revealed a range of responses, encompassing high-T_C superconductivity [1], colossal magnetoresistance (CMR) [2-4], multiferroicity [5], and magnetic semiconductivity [6, 7], all of which continue to present fundamental challenges to the understanding of these complex materials. Figure 1.1 summarizes transport measurements on a number of these compounds, and serves to demonstrate not only the unusual response of these systems, but also their complexity.

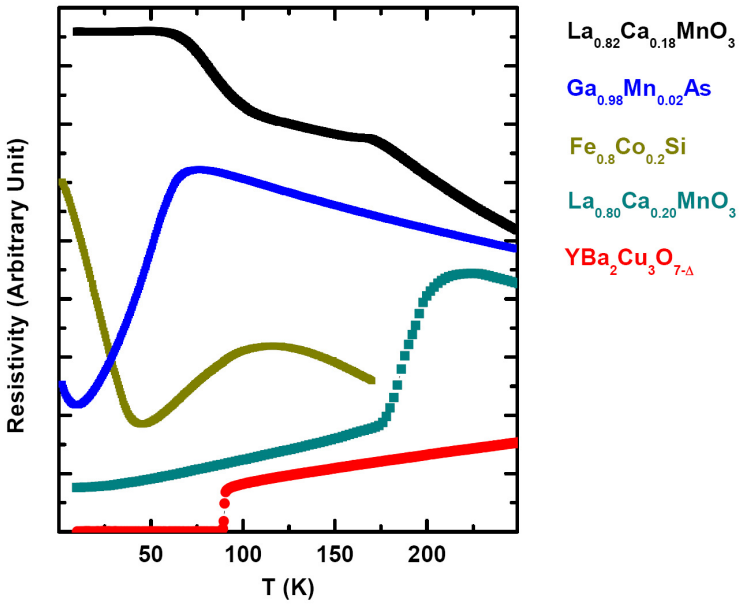

Figure 1.1 *Temperature-dependent zero-field resistivity of various magnetic systems. The superconductor, $YBa_2Cu_3O_{7-\Delta}$, was prepared by Dr. X. Zhou.*

Nevertheless, there is a close correlation between such resistive characteristics and the ordered state that emerges at low temperature, particularly magnetic order. This correlation underlies the present study, which focuses on the magnetic and transport behavior of various Manganese (Mn), Iron (Fe) and Cobalt (Co) containing materials, with particular emphasis on the nature of the magnetic order they display and the critical exponents that characterize the accompanying phase transition. The two specific topics that will be covered include: first, CMR in manganese oxides, and second, the effects of doping semiconductors such as GaAs and Si with magnetic elements Mn, Fe, and Co.

1.1 Colossal Magnetoresistance Manganites

In 1856, Lord Kelvin (William Thomson) discovered the magnetoresistance effect (MR) in Fe and Ni, viz., a resistance change induced by the application of an external magnetic field. This observation was qualitatively explained as follows: the application of a magnetic field in ferromagnets (partially) confines the magnetic moments in the direction of the field, consequently decreasing the scattering probability. This leads to the suppression of resistivity; hence the associated MR, $\Delta\rho = [\rho(H) - \rho(0)]/\rho(H)$, is negative [7]. More recently, considerable effort has been devoted to searching for systems which exhibit a large MR, as such materials would have a tremendous impact on modern electronics, particularly to the magnetic recording industry [8].

In conventional (magnetic) metals (Mn, Fe, Ni, Co, rare-earths, etc.), the MR is relatively small (typically < 5%) even at room temperature, which is far below the magnetic ordering temperature for the ferromagnetic transition elements. Consequently there are two areas of contemporary interest, the so-called giant and colossal MR materials; the MR in both of these systems has been interpreted using spin related mechanisms. "Giant" magnetoresistive structures are usually fabricated from alternating ferromagnetic and nonmagnetic layers, termed heterostructures, and their MR arises from a field-induced change of magnetization/spin direction of adjacent layers from parallel (low resistance) to antiparallel (high resistance) [9]. The pioneering work by Grünberg and Fert in this area led to them being awarded the 2007 Nobel Prize in Physics [10]. In contrast, CMR materials display a very large change in resistance induced by the application of a magnetic field in the vicinity of a metal-insulator transition (MIT), the temperature of which displays a marked field dependence as a consequence of the accompanying ferromagnetic to paramagnetic (FM-PM) phase transition [2-4]. A complete picture of CMR may also be important for the understanding of high temperature superconductivity, as CMR materials share considerable structural similarities (viz., a perovskites structure) with the high temperature superconducting cuprates (for instance the $YBa_2Cu_3O_{7-\Delta}$ system), and both classes of materials often display semiconducting behavior at higher temperatures [11]. However, the superconductivity of the cuprates is replaced, typically, by a magnetically ordered ground state in the manganites [3, 4].

An illustration of CMR behavior is reproduced in Figure 1.2 for a sample which forms part of the present study.

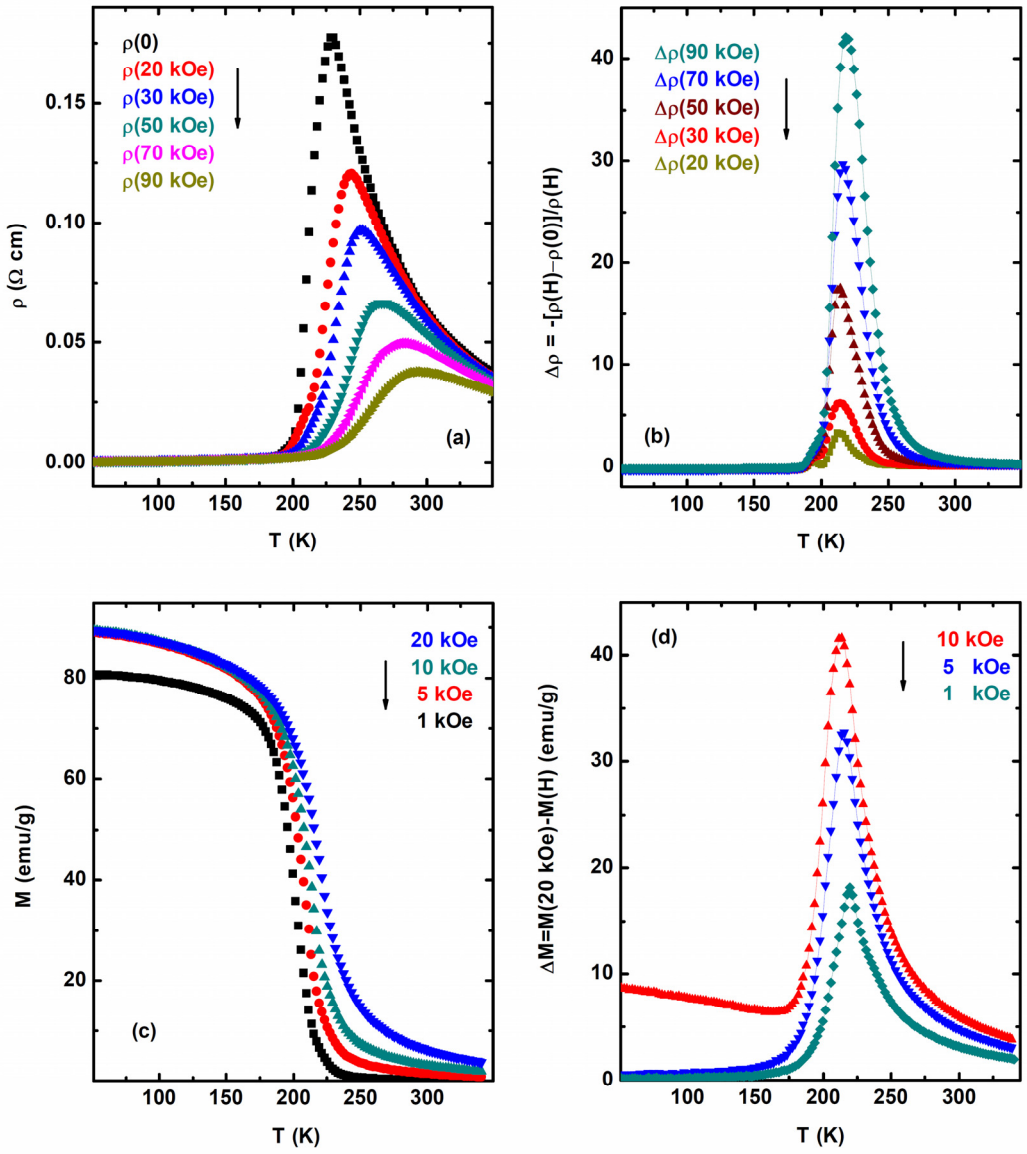

Figure 1.2 *Observation of CMR in single crystal* $La_{0.79}Ca_{0.21}MnO_3$. *(a) The temperature dependent resistivity measured in various static magnetic fields indicates the occurrence of CMR. (b) The corresponding MR* $\Delta\rho=[\rho(H)-\rho(0)]/\rho(H)$. *(c) The measured temperature dependent magnetization under various magnetic fields, indicating the appearance of a FM-PM phase transition in close proximity to the occurrence of CMR. (d) The magnetization difference* ΔM *between the various measuring fields. Such peaks are essentially coincidental with the corresponding peaks in resistivity and MR.*

CMR has been widely studied in manganese based oxides, particularly perovskite manganites characterized by the general formula $A_{1-x}B_xMnO_3$, A being a trivalent rare-earth ion (i.e., La, Nd, Pr…) and B a divalent alkaline earth cation (i.e., Ba, Ca, Sr…) which substitutes randomly at the trivalent rare-earth ion "A" sites; x represents the substitution/doping level [3, 4]. Changes in doping level modulates some of the Mn valence states form 3+ to 4+ (to maintain charge neutrality), leading to various interesting physical phenomena, CMR especially, an explanation of which remains contentious.

A qualitative explanation of CMR in the manganites was originally provided some 50 years ago by Zener based on a spin-dependent transfer picture for charge carriers, the so-called Double Exchange mechanism (DE) [12], illustrated in Figure 1.3. In this introductory section a brief summary of this approach is given, the detailed physics of the manganites will be discussed in Chapter 4.

The physics underlying this mechanism is based on a picture of charge carriers (in essence, an e_g electrons) hopping from Mn^{3+} ions to neighboring Mn^{4+} ions through the intervening O^{2-} ion. This process is thus envisioned as the jump of an electron from a Mn^{3+} ion to an intervening O^{2-} ion, accompanied by the simultaneous transition of an electron hopping from the O^{2-} ion to the adjacent Mn^{4+} ion. There is, however, no mechanism through which the participating spin(s) can change orientation. In consequence, if the Mn spins are aligned parallel (as in a FM state), the transfer of conduction electrons occurs with a higher probability than in a disordered PM state, as

depicted below. As electron hopping underlies conductivity, the onset of ferromagnetism and metallicity are linked in this model [13].

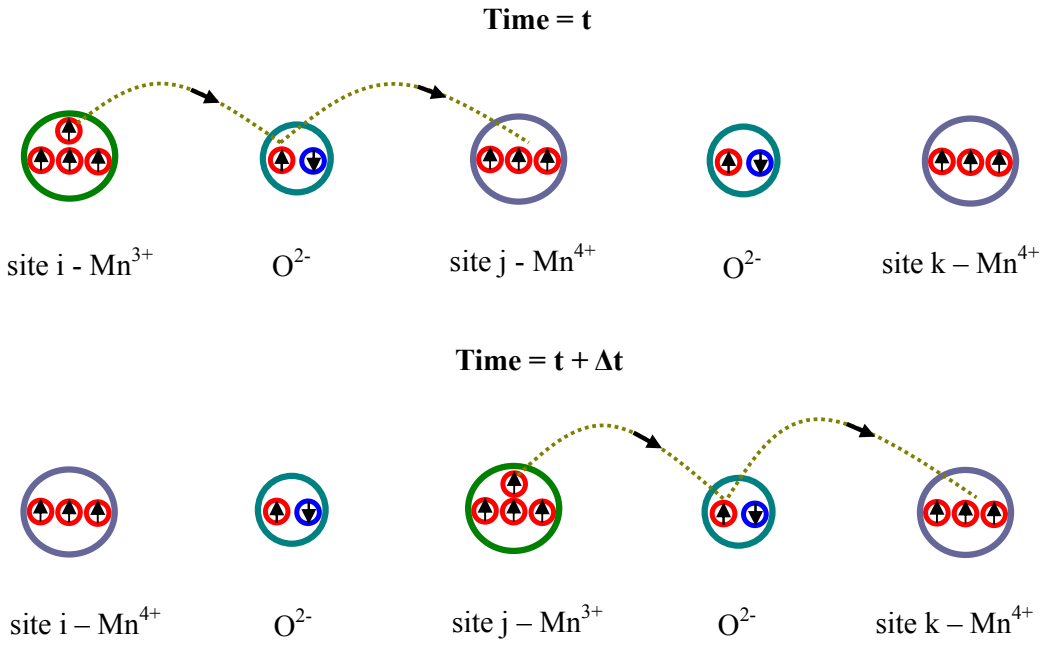

Figure 1.3 *Schematic picture of the spin-dependent Double Exchange mechanism in* $Mn^{3+} – O^{2-} – Mn^{4+}$ *chains.*

The disordered (PM) state, in which such electron hopping occurs with low probability, corresponds to the insulating/semiconducting state. As a corollary, the "brute force" alignment of spins by an applied field close to the FM ordering/MIT temperature, enhances the hopping probability considerably, thus the resistivity decreases dramatically with field in this regime, leading to the occurrence of a large/colossal MR. Thus one of, if not the most important predictions of the DE mechanism, is the coincident emergence of ferromagnetism and metallicity.

While DE thus provides a qualitative explanation of CMR, more recent experiments indicate that this model fails at a quantitative level. In particular, DE alone has been shown to be unable to reproduce the large resistivity/low conductivity that characterizes the high temperature, disordered PM phase [14]. Moreover, it certainly does *not* provide an explanation of the coexistence of ferromagnetism and insulating behavior that is observed in some doped Mn perovskites [15]. Subsequently, explanations of CMR behavior have invoked spin-lattice coupling [16], spontaneous nanoscale electronic phase separation [3, 17], the emergence of a Griffiths-like phase [18-20], amongst others [3, 4], as physical mechanisms that contribute, if not underlie, this phenomenon. Nevertheless, while there appears to be current agreement that this is a percolation controlled effect, with much current attention, both theoretical (based on Monte Carlo simulations) [17] and experimental (using the optical or spectroscopic investigations, illustrated in Figures 1.4 and 1.5) [21-23], being focused on inhomogeneous, competing antiferromagnetic (AFM) and FM states, the precise mechanism responsible for CMR remains controversial. What is clear, however, is that manganese perovskite oxides possess strong electron-phonon interactions [24] and this has led to the conclusion that such materials represent an important class of strongly correlated electronic system, displaying a fascinating combination of coupling between charge, spin, orbital and vibrational degree of freedom [3, 4]. Correspondingly, there is a close connection between magnetic order and transport behavior, summarized in Figures 1.2, 1.4 and 1.5, a connection on which a substantial part of the present work focuses.

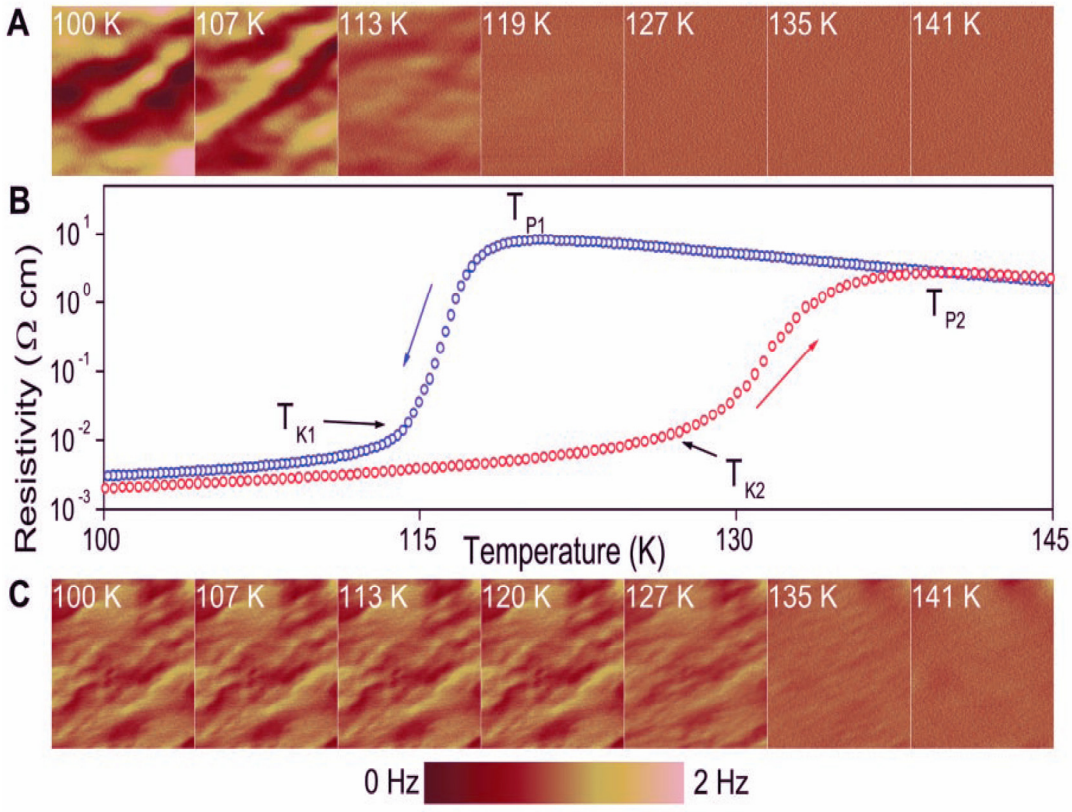

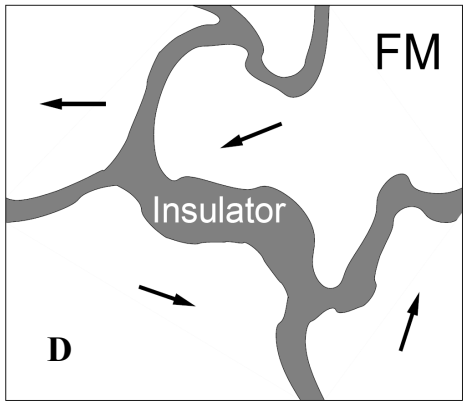

Figure 1.4 *Experimental and theoretical proposals for nanoscale phase separation. Figures (a) – (c) for* $La_{0.33}Pr_{0.34}Ca_{0.33}MnO_3$ *[21]. (a) The magnetic force microscopy images for cooling while (c) is for warming. (b) The resistivity measured on warming and cooling. (d) Proposed theoretical state for manganites in the CMR regime. FM clusters are locally formed, but with the random orientation of the order parameter. The insulator forms walls between the FM metallic regions.*

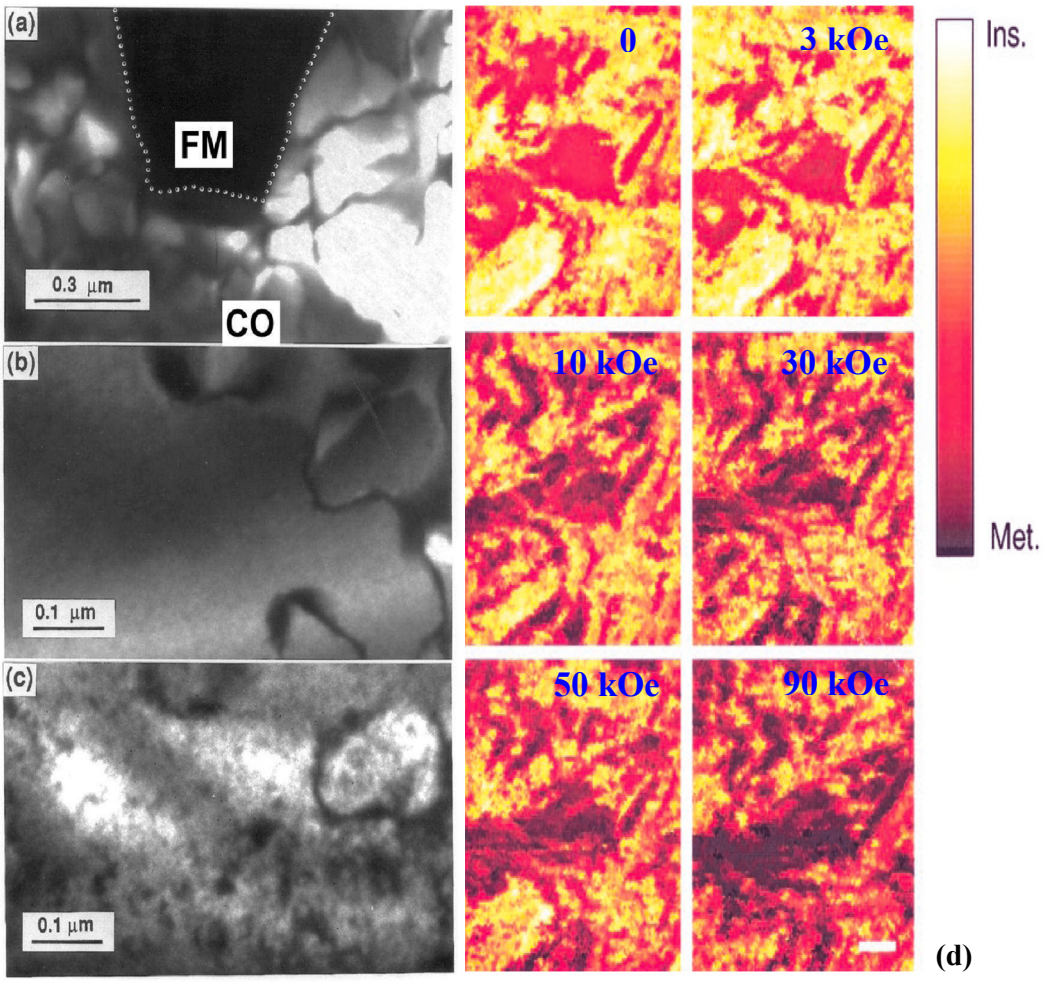

Figure 1.5 *Application of imaging techniques to CMR compounds. Figures (a) – (c) are the dark-field images for* $(La_{1-y}Pr_y)_{1-x}Ca_xMnO_3$*, from [22]. (a) The coexistence of insulating and metallic regions at 20 K for y = 0.375. Figure (b) corresponds to y = 0.4 at T = 17 K while (c) for y = 0.4 at 120 K. The latter shows the development of nanoscale charged-ordering (CO) domains at* $T > T_C$*. (d) The Scanning Tunneling Spectroscopy images of the local electronic structure of* $La_{0.67}Ca_{0.33}MnO_3$ *thin film from [23], obtained just below* T_C *in magnetic fields of 0, 3, 10, 30, 50, 90 kOe from left to right and top to bottom.*

1.2 Magnetic Semiconductors

A second topic, less extensively covered in this thesis, concerns magnetic semiconductors. Traditional Si, GaAs, Ge, or InAs based integrated circuit/semiconductor electronic devices function via the manipulation of the charge of the electron, whereas, in storage technology (magnetic tapes, hard disks, etc.) the relevant degree of freedom is the electron spin. Attempts to combine both the charge and spin of electrons have led to the emergence of the so-called field of "spintronics" [25]. Such a combination could have the important advantage of enabling the storage and processing of information to be performed simultaneously. The prototypical example is the use of electric current/field to control magnetization [26]. In this context, the effects of doping the magnetic elements Mn into GaAs [27] and Fe, Co into Si [28] have been the subject of numerous studies. The focus of the present work is on the physical (magnetic and magneto-transport) properties of materials, rather than specific devices such as diodes, transistors, etc.

One of the materials that has been investigated is formed by the doping of the magnetic elements Fe and Co into Si, i.e., $Fe_{1-x}Co_xSi$. This family of compounds is not only interesting from the point of view of understanding complex materials, but it also has the potential for applications. Of the parent compounds, FeSi is a non-magnetic, narrow-gap (30 meV) semiconductor, with the latter term being adopted in the present work based simple on the criterion used by Faraday, viz., a negative temperature

derivative of the resistivity ($d\rho/dT < 0$); CoSi is a diamagnetic semimetal with a temperature independent susceptibility [29]; however, the combined substitution of Fe and Co into Si leads to various types of magnetic order [29]. These ternary compounds also exhibit a large anomalous Hall effect, suggesting their use as magnetic field sensors. They also display a positive MR, $\Delta\rho = [\rho(H) - \rho(0)]/\rho(H) > 0$, over a broad temperature range around the magnetic ordering temperature. The origin of this positive MR is controversial as it does not appear to be explained by current theories. Initially its origin was attributed to quantum interference effects rather than simple scattering [28]. This was based on the fact that $Fe_{1-x}Co_xSi$ is a highly disordered ferromagnet with a low carrier density, so that the same electrons were responsible for both electrical conduction and magnetism. This was challenged subsequently by consideration of the Zeeman modification of exchange-split spin-up and spin-down bands [30]. The issue remains open.

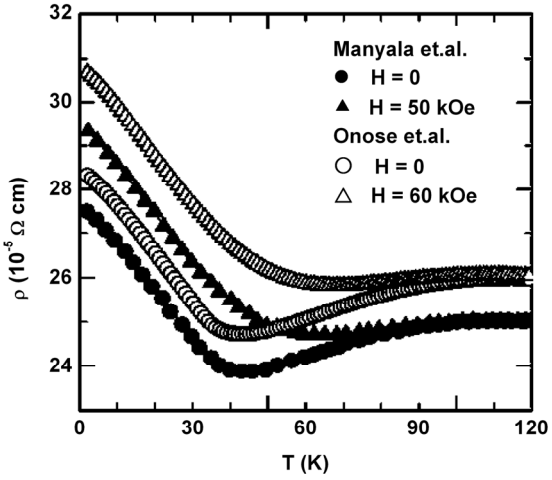

Figure 1.6 *Observation of positive MR in $Fe_{1-x}Co_xSi$ with x = 0.2. Zero field temperature dependent resistivity of $Fe_{0.8}Co_{0.2}Si$ for both poly- (Manyala, et.al., [28]) and single-crystals (Onose, et.al., [30]). These data clearly confirm the presence of positive MR.*

A second, sub-category of materials considered here is formed by doping Mn into GaAs, so-called dilute magnetic semiconductors [6, 31]. This particular system is probably one of the most well studied magnetic semiconductors. Initial work in this field was performed by Ohno and co-workers at Tohoku University using Molecular Beam Epitaxy (MBE) techniques for introducing relatively small concentrations of magnetic elements into nonmagnetic semiconducting hosts [26, 27, 31, 32]. This led to dramatic modifications of the magnetic, transport, and optical properties in the presence of magnetic fields. Figure 1.7 (a) summarizes some of the structural changes accompanying doping in $(Ga_{1-x}Mn_x)As$. On substitution, the spin S = 5/2 Mn ions provide both a magnetic moment and act as acceptor levels, providing holes in the valence band. These holes, in turn, facilitate Mn-Mn interactions, leading to the presence of carrier mediated ferromagnetism [6, 27, 33]. The phase diagram characterizing the relationship between carrier density and ordering temperature for various doping levels [31] is given in Figure 1.7 (b).

Following the work by Ohno, numerous papers were published on this topic, including, for example, the idea of using electric fields to control ferromagnetism in $(Ga_{1-x}Mn_x)As$ [26]. Such experiments demonstrated conclusively that the application of a biasing voltage can change FM properties (specifically, the magnetic ordering temperature). From a technological standpoint, however, the widespread use of such materials in spintronic circuits/devices can only be achieved through the realization of room temperature ferromagnetism in them. A promising direction currently being

pursued is fabricating Fe/($Ga_{1-x}Mn_x$)As heterostructures, experiments on which have demonstrated the existence of a room temperature magnetization [34].

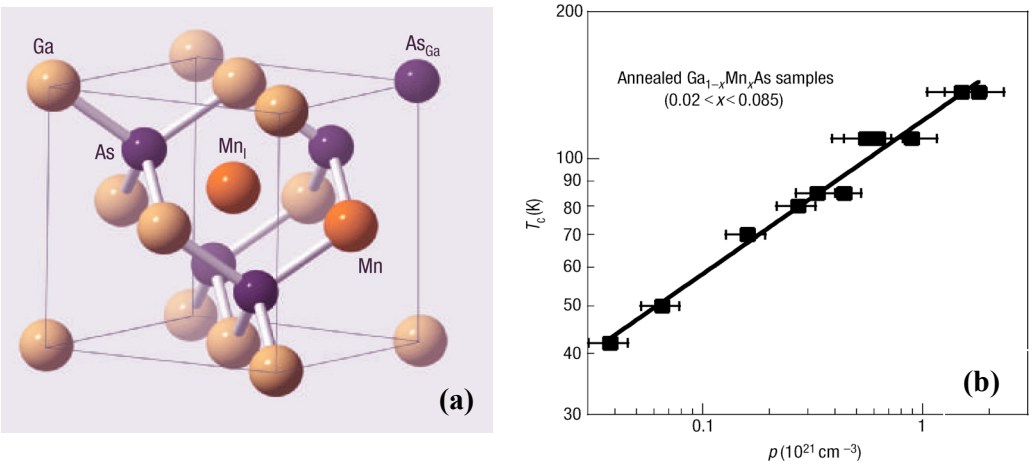

Figure 1.7 *Crystal structure and phase diagram for ($Ga_{1-x}Mn_x$)As. Figure (a) shows Mn ions substitute directly into Ga ion sites. Figure (b) reproduces the phase diagram that characterizes the correlation between the ordering temperature T_C and the charge carrier density, indicating carrier mediated ferromagnetism.*

The onset of ferromagnetism in ($Ga_{1-x}Mn_x$)As, particularly at low Mn doping levels, has been treated traditionally within the framework of a long range interaction model, i.e., the Landau Mean-Field model [6, 33]; such interactions arise from the itinerant nature of the charge carriers, discussed in more detail in Chapter 5. However, prior to the present study, there has been no *direct* confirmation of the Mean-Field nature of the prevailing interactions; specifically, measured critical exponents that conform with the corresponding model predictions. This thesis will, in part, address this issue, in particular for a photo-lithographically prepared microstructure, using detailed magneto-transport measurements.

In summary, this thesis focuses principally on the subject of CMR in manganites, and to a lesser extent, magnetic semiconductors, with emphasis on their magnetic and transport properties, and correlations between them. Following this introduction, a second chapter reviews the theoretical background, concentrating on magnetic phase transition theory and its prediction for measured parameters such as the dc magnetization and ac susceptibility; this is complemented by a discussion of a proposal for an "unconventional" approach to scaling behavior based on magneto-transport measurements, specifically, the anomalous Hall effect (AHE). The third chapter surveys the use of a Quantum Design Physical Property Measurement System (PPMS) Model 7000 Magnetometer in measuring dc/ac magnetic properties, along with the longitudinal resistivity and the Hall effect. This is followed by a fourth chapter which presents the main results obtained on CMR manganites $La_{1-x}Ca_xMnO_3$, $La_{1-x}Ba_xMnO_3$, $(La_{1-y}Pr_y)_{0.7}Ca_{0.3}Mn^{16/18}O_3$ and $Pr_{1-x}Ca_xMnO_3$. These include the influence of the doping level (x) on the MIT, the emergence of a Griffiths-like phase, and the critical exponents/universality class accompanying ferromagnetism. The next chapter presents work on the magnetic semiconductors $Fe_{0.8}Co_{0.2}Si$ and $Ga_{0.98}Mn_{0.02}As$, where emphasis is placed on establishing the correlation between magnetism and transport behavior and the acquisition of critical exponents from magneto-transport measurements. The thesis concludes with a summary of the principal conclusions and the outlook for future work.

Chapter 2

Phase Transition Theory

Given the close proximity of the magnetic transition temperature with characteristic features in the transport properties (the first order derivative resistivity $d\rho/dT$, for example) in a wide range of magnetic systems, including doped manganese perovskites and magnetic semiconductors, the influence of the nature of the former on the latter – particularly its field dependence – has emerged as an important topic of study.

2.1 Conventional Approaches for the Determination of Critical Exponents and Universality Class

A phase transition, the transformation of a system from one phase to another, is often accompanied by an abrupt change in one or more physical parameters, such as the specific heat, magnetization, susceptibility, resistivity, etc. Generally, two phases will coexist if the free energies (F) of the phases are equal; however the derivative(s) of this free energy will not in general be equal in the two phases. Early characterization of phase transitions by Ehrenfest was based on which derivative of F inherited a discontinuity at the transition; current approaches classify transitions as discontinuous (if a first derivative of F exhibits a discontinuity), otherwise as continuous [35].

2.1.1 Landau Mean-Field Theory

Based on the assumptions that the free energy of a system is analytic and displays the symmetry of the Hamiltonian, Landau argued [36] that the free energy, $F(T,m)$, as a function of temperature (T) and (reduced) magnetization (m) (where $m = M_{Spon}(T)/M_{Spon}(0)$, $M_{Spon}(T)$ being the spontaneous magnetization at different temperatures) near a continuous/second order magnetic phase transition could be expressed as a Taylor-like series expansion in m. The latter (m) assumes the role of the order parameter near such a transition (a convenient property of the system, being zero above the ordering temperature, T_C, and non-zero below it). The presence of inversion symmetry dictates that this power series is even, so that the free energy – the Helmholtz free energy in this case – reads:

$$F(T,m) = F_0(T) + a_2(T)m^2 + a_4(T)m^4 + a_6(T)m^6 ..... \quad 2\text{-}1$$

Since m is small in the "critical" region near T_C, this series can be truncated to:

$$F(T,m) = a_2(T)m^2 + a_4(T)m^4 \quad 2\text{-}2$$

The equilibrium condition then yielding:

$$\left.\frac{\partial F}{\partial m}\right|_T = 2a_2(T)m + 4a_4(T)m^3 = 0 \Rightarrow a_2(T) = -2a_4(T)m^2 \quad 2\text{-}3$$

The condition for stability (correspondingly) reads:

$$\left.\frac{\partial^2 F}{\partial^2 m}\right|_T = a_2(T) + 6a_4(T)m^2 > 0 \quad 2\text{-}4$$

At temperatures below the ordering temperature T_C, hence m > 0, a simple

resubstitution of equation (2-3) into equation (2-4) yields:

$$-2a_4(T)m^2 + 6a_4(T)m^2 > 0 \Rightarrow a_4(T)m^2 > 0 \Rightarrow a_4(T) > 0 \qquad 2\text{-}5$$

Resubstitution back to equation (2-3) then indicates $a_2(T) < 0$ for $T < T_C$ ($m > 0$). Immediately above T_C, where the random alignment of moments yields $m = 0$, the stability condition reads:

$$\left.\frac{\partial^2 F}{\partial^2 m}\right|_T = a_2(T) + 6a_4(T)m^2 > 0 \Rightarrow a_2(T) > 0 \qquad 2\text{-}6$$

These arguments then indicate that $a_2(T)$ changes sign at T_C, hence, in the spirit of a Taylor-like expansion, it can be written as:

$$a_2(T) = \alpha_0(T - T_C), \quad \alpha_0 > 0 \qquad 2\text{-}7$$

With the application of an external magnetic field H, the corresponding (Gibbs) free energy becomes:

$$G(T,m) = F_0(T) + a_2(T)m^2 + a_4(T)m^4 + a_6(T)m^6 ..... - Hm \qquad 2\text{-}8$$

in which the last term represents the energy of interaction of the magnetization M with the applied field H. Following the same procedure indicated above, the so-called equation of state becomes:

$$H/m = 2\alpha_0(T - T_C) + 4a_4(T)m^2 \qquad 2\text{-}9$$

Thus plots of H/M versus M^2 – referred to as Arrott plots [37] – should display a positive slope to ensure the stability condition ($a_4(T) > 0$), viz., the stability of the continuous (second order) transition. Failing to satisfy this criterion results in the occurrence of a first order/discontinuous transition. The Arrott plot criterion thus enables the order of the transition to be established directly from magnetization data.

This latter criterion, also referred to as the Banerjee Criterion [38], has seen wide use. Other criteria used to confirm the presence of a first order/discontinuous transition include the observation of hysteresis in the transition itself (which can be seen in both the magnetic and transport data), and the appearance of "S"-shaped magnetization curves near the transition [38, 39]. The above discussion, incidentally, is also applicable to ferroelectric systems, in which the relevant experimental variable in free energy is the electrical polarization (P) [40]. The application of the above – or some suitable modification – might generate new insights into the recently discovered multiferroic materials (materials that simultaneously exhibit ferromagnetism and ferroelectricity).

Another key use of Arrott-plots is in establishing the appropriate equation of state, specifically by the observation that plots of H/M versus M^2 result in a series of parallel straight lines in some systems, the itinerant ferromagnet $ZrZn_2$ [41], for example, Figure 2.1 (a). Further, in such plots, the intercepts on the vertical axis yield the spontaneous magnetization at the appropriate temperature, while those on the horizontal axis the inverse initial susceptibility; the isotherm passing through origin, the critical isotherm, corresponds to T_C, The latter can be used subsequently to confirm the applicability of a Mean-Field approach, as follows. Below T_C, in zero applied field (H = 0), the left side of equation (2-9) vanishes, so:

$$m^2 \propto (T - T_C) \Rightarrow m \propto (T - T_C)^{\beta}, \beta = 1/2 \qquad 2\text{-}10$$

i.e., the temperature dependence of the spontaneous magnetization.

At the ordering temperature $T = T_C$, where $2\alpha_0(T - T_C) = 0$:

$$H \propto m^3 \Rightarrow m \propto H^{1/\delta}, \delta = 3 \qquad 2\text{-}11$$

yielding the field-dependence of the magnetization along the critical isotherm.

Finally, above the ordering temperature in small applied fields, so $m^2 \approx 0$:

$$H / m = 1/\chi_i(T) \propto (T - T_C)^{\gamma}, \gamma = 1 \qquad 2\text{-}12$$

predicting a linear dependence of the inverse initial susceptibility on temperature immediately above T_C in the disordered PM phase. Equations (2-10) – (2-12) yield various power-law exponents, more generally termed critical exponents, with $\beta = 1/2$, $\delta = 3$, $\gamma = 1$ in the Mean-Field approach. $ZrZn_2$ is a ferromagnet that has been shown to display such Mean-Field characteristics [41].

It is possible to express all three of the above results in a single equation [42], viz.,

$$M(H_i, t_m) = |t_m|^{1/2} \cdot F_{\pm}\left(\frac{H_i}{|t_m|^{3/2}}\right) \qquad 2\text{-}13$$

However, the general behavior of the function $F_{\pm}(x)$ – referred to as the scaling function – cannot be determined, simply its *asymptotic* behavior in the limits $t_m \rightarrow 0$ (where $t_m = (T–T_C)/T_C$ is the reduced temperature) and $H_i \rightarrow 0$ ($H_i = H_a–N_DM$ being the internal field, H_a the applied field and N_D the demagnetization factor). Specifically, for $T < T_C$ and $H_i = 0$, the argument of the function F_- is a constant (albeit zero), thus the function itself is a constant, yielding:

$$M \propto t_m^{1/2}, \beta = 1/2 \qquad 2\text{-}14$$

as in equation (2-10). Immediately above T_C in *small* applied fields, a linear response of the magnetization to field is expected, i.e., the leading term in F_+ is linear in its argument, so that

$$M(H_i, t_m) = t_m^{1/2} \cdot \frac{H_i}{t_m^{3/2}}, t_m > 0, H_i > 0 \qquad 2\text{-}15$$

Thus:

$$\left(\frac{M}{H_i}\right)_{H_i \to 0} = \chi_i(T) \propto t_m^{-1}, \gamma = 1 \qquad 2\text{-}16$$

in agreement with equation (2-12) for the temperature dependence of the inverse initial susceptibility ($1/\chi_i$). Finally at T_C, i.e., along the critical isotherm, where $t_m = 0$, for the magnetization M to assume a definite form (i.e., to be measurable), the dependence on t_m must vanish, leading to:

$$M(H_i, t_m = 0) = t_m^{1/2} \cdot \left(\frac{H_i}{t_m^{3/2}}\right)^{1/3} = H_i^{1/3}, \delta = 3 \qquad 2\text{-}17$$

as deduced earlier (equation (2-11)) for the dependence of magnetization on field along the critical isotherm.

While the general dependence of the function $F_{\pm}(x)$ on its argument cannot be found theoretically, it can be deduced experimentally by plotting $M/t_m^{1/2}$ against the argument $H_i/t_m^{3/2}$ of the scaling function. Such plots, reproduced in Figure 2.1 (b) for $ZrZn_2$ [41], are not only regarded as a final, comprehensive test of the applicability of the chosen exponents, but the form of the two "branches" (one for data acquired above T_C (+) and the other below (-)) yield the general form of this scaling function. Note that, in general, these critical exponents β, γ and δ are related using the so-called Widom relation $\gamma = \beta(\delta - 1)$ [35], clearly satisfied for Mean-Field exponents. This relationship, essentially ensuring thermodynamic stability (actually $\gamma \geq \beta(\delta - 1)$) is satisfied as an equality if the scaling hypothesis assumptions are satisfied.

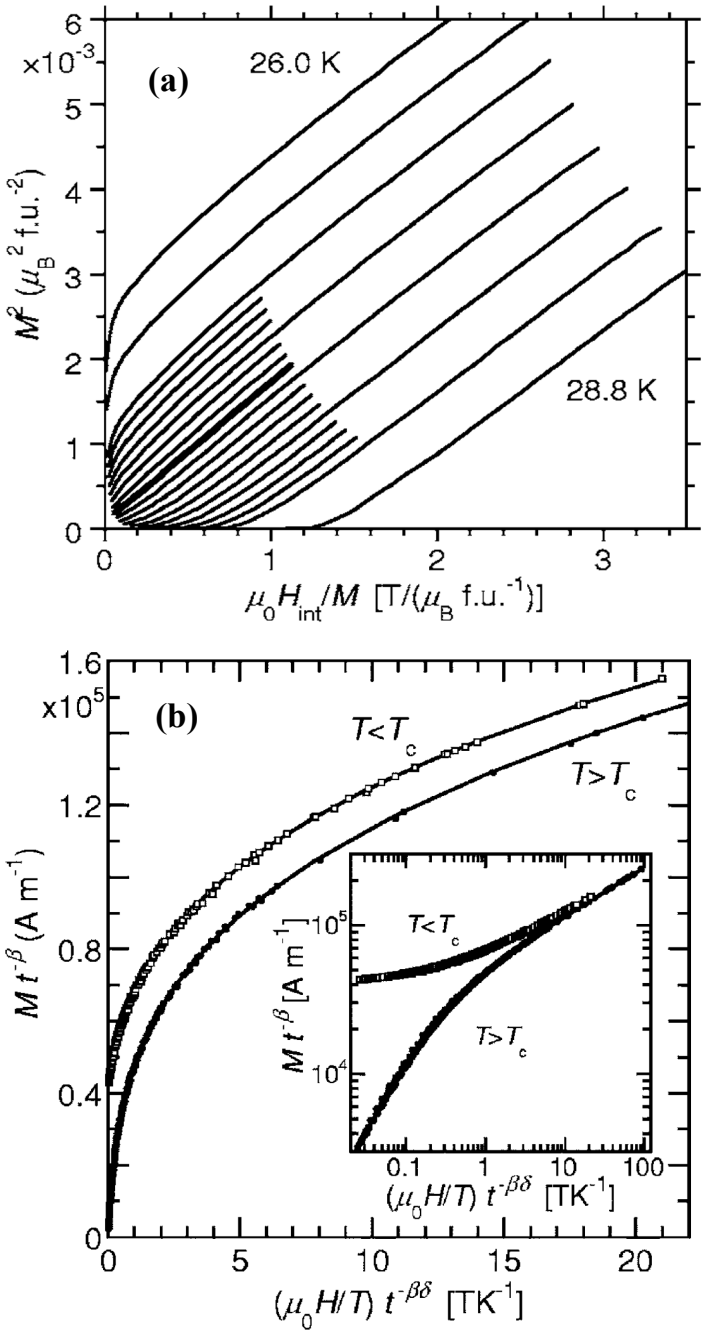

Figure 2.1 *Arrott plot and scaling testing of the magnetic isotherms near T_C for $ZrZn_2$. (a) The isotherms are measured in 0.4 K intervals and 0.2 K near T_C. The bond line passing through the origin yields $T_C \approx 27.5$ K. (b) Scaling test using T_C and Mean-Field exponents. The region $H < 50$ Oe has been excluded to avoid systematic errors due to multiple FM domains inside the sample. The correct choice of T_C, β, and δ causes the data to collapse onto single curves for $T < T_C$ and $T > T_C$.*

2.1.2 Modification to Mean-Field Theory

The Mean-Field model, however, frequently fails to quantify the onset of ferromagnetism, hence magnetic critical behavior in many systems, pure Ni and Fe, for example. This failure is usually attributed to the fact that the relevant interaction are of a finite range, rather than being infinite range as underlies the Mean-Field approach. In attempt to modify equation (2-9) to account for such differences, Arrott and Noakes suggested a modified equation of state of the form [43]:

$$\left(\frac{M}{M_1}\right)^{1/\beta} = \frac{T_C - T}{T_C} + \left(\frac{H_i}{M}\right)^{1/\gamma} \qquad 2\text{-}18$$

where M_1 is a material specific constant. The appropriate choice of the "modified" exponents β and γ are those that result in plots of $(M/M_1)^{1/\beta}$ versus $(H_i/M)^{1/\gamma}$ being linear, enabling estimates of the spontaneous magnetization, the inverse initial susceptibility and the Curie/ordering temperature T_C to be estimated in an analogous manner to that outlined earlier. These are subsequently utilized in the following way.

In a more comprehensive approach to the problem of the magnetic response near a continuous PM-FM transitions, Kadanoff [42], Widom [44] and amongst others [45], proposed a general scaling equation of state – a generalization of equation [35, 42] – relating the (reduced) magnetization m to the linear scaling fields t_m and $h_i \sim H_i/T_C$:

$$m(h_i, t_m) = |t_m|^{\beta} \cdot F_{\pm}\left(\frac{h_i}{|t_m|^{\gamma+\beta}}\right) \qquad 2\text{-}19$$

As previous, the general behavior of function $F_{\pm}(x)$ remains unspecified, although, using

the corresponding arguments to those presented earlier, its asymptotic behavior for small values of the scaling fields t_m and h_i predict the following power-law dependences:

For the spontaneous magnetization $M_S(T) = M_S(H_i=0, T)$, and reduced m in the ordering temperature range:

$$M_S(T) = M_S(0)\left(1 - \frac{T}{T_C}\right)^{\beta} \; ; \quad m(0,t) \propto B\left|t_m\right|^{\beta} \; (T < T_C, t_m \rightarrow 0) \qquad 2\text{-}20$$

Along the critical isotherm ($T = T_C$, $t_m = 0$), by using the Widom equality ($\gamma + \beta = \beta\delta$):

$$M(H_i, T = T_C) = M_0 H_i^{\,1/\delta} ; m(h_i,0) \propto E\, h_i^{\,1/\delta} \qquad 2\text{-}21$$

While for the dependence of the initial susceptibility $\chi_i(T) = (\partial M / \partial H_i)_{H_i=0}$ on the reduced temperature (t_m):

$$\chi_i(T) = \chi_0\left(\frac{T}{T_C} - 1\right)^{-\gamma} \; ; \quad \chi_i(t_m) = \frac{\partial m}{\partial h} \propto C t_m^{\,-\gamma} \; (T > T_C) \qquad 2\text{-}22$$

These power laws also follow from the corresponding limits of the modified Arrott-Noakes equation of state. The estimates of $M_S(T)$, $M(H_i,T)$ and $\chi_i(T)$ deduced above are then tested against these power-laws predictions, enabling "refined" estimates for the exponents to be made. This whole process is repeated, with *small* adjustments in T_C, until self consistency is achieved [46]. A final comprehensive test of both exponent values and ordering temperature T_C estimates is provided by plotting $M / t_m^{\,\gamma}$ against the argument of the scaling function, $M / t_m^{\,\beta\delta}$, with good data collapse onto two branches (one for data acquired above T_C (+) and the other below (-)), providing final confirmation. While it is well recognized that the scaling law behavior is asymptotic in

nature, viz., $h_i \rightarrow 0$, $t_m \rightarrow 0$, experimental data in this region is usually excluded from analyses. There are two specific reasons for doing this. First, scaling law behavior is based on the contributions from critical fluctuations, while the measured response includes contributions from both critical and regular/technical contributions. The former – designated the singular contribution – underlies equations (2-19) – (2-22) – with which the relevant data should be compared; the latter, which arise from technical processes such as domain wall motion and coherent rotation, thus need to be excluded. This is accomplished by applying fields which drive the system to technical saturation (as might be anticipated), extrapolations from which eliminate the corresponding contribution. The necessity of this procedure notwithstanding, there is no quantitative criterion that can be utilized in this context that ensures that such conditions have been achieved (at least for magnetization data; the corresponding problem in ac susceptibility data is discussed later). Second, for samples of non-uniform shape (not ellipsoids of revolution, for example), uncertainties related to inaccurate demagnetization factors/fields arise, which impact primarily data at low field. Again no quantitative criterion has been articulated, but typically data for which the demagnetization field exceeds between 25 to 40% of the applied field are excluded.

An independent appraisal of scaling behavior near a continuous/second order PM-FM transitions can also be obtained through measurements of the ac susceptibility in various superimposed static magnetic fields (H_a) [46-48]. The application of such fields enables a series of critical susceptibility maxima to be resolved, the temperature

(T_m) of which increases while the amplitude ($\chi(H_a,T_m)$) decreases as H_a is increased. Such behavior agrees with the general predictions of the fluctuation-dissipation theorem [35], while the specific field/temperature-dependence of these susceptibility maxima can be deduced from equation (2-19). The latter, used in conjunction with the Widom equality, yields:

$$\chi(h_i, t_m) = \frac{\partial m}{\partial h_i} = |t_m|^{-\gamma} \cdot G_{\pm}\left(\frac{h_i}{|t_m|^{\gamma+\beta}}\right) = (h_i)^{1/\delta-1} \cdot Y_{\pm}\left(\frac{h_i}{|t_m|^{\gamma+\beta}}\right) \qquad 2\text{-}23$$

Here $G_{\pm}(x)$ is the derivative of $F_{\pm}(x)$ with respect to its argument, and $Y_{\pm}\left(\frac{h_i}{|t_m|^{\gamma+\beta}}\right) = G_{\pm}\left(\frac{h_i}{|t_m|^{\gamma+\beta}}\right) \cdot |t_m|^{-\gamma} \cdot (h_i)^{\frac{\gamma}{\gamma+\beta}}$. Equation (2-23) predicts that the locus of these susceptibility maxima (maxima emerging when the susceptibility is measured as a function of temperature in *fixed* applied field, so H_i/h_i = constant) in the (H-T) plane is given by:

$$\left(\frac{\partial \chi}{\partial t_m}\right)_{h_i} = 0 \text{ , i.e. } \quad \dot{Y}_{\pm} = 0 \qquad 2\text{-}24$$

This condition is satisfied if the argument of the function – and hence the function itself – is a constant, leading to:

$$\chi(h_i, t_m) \propto h_i^{1/\delta-1} \qquad 2\text{-}25$$

This power-law dependence of the susceptibility *peak* amplitude on internal field H_i/h_i enables the critical exponent δ to be estimated direct, i.e., it is independent of the choice of T_C. Such a result represents a distinct advantage over conventional magnetization-based approaches, for which the determination of T_C is a prerequisite prior to extracting estimate for δ from the data take along critical isotherm. This result

also plays a pivotal role in assessing the behavior of systems displaying a Griffiths-like phase, as discussed in Chapter 4.

It also follows from equation (2-24) and the subsequent discussion that $h_i / |t_m|^{\gamma+\beta}$ is a constant at the susceptibility peak, thus the field dependence of the (reduced) peak temperature is given by:

$$t_m = (T_m - T_C)/T_C \propto (h_i)^{1/(\gamma+\beta)} \qquad 2\text{-}26$$

This power-law prediction enables the "cross-over" exponent ($\gamma + \beta$) to be estimated, although here a value for T_C is obviously needed. As mentioned earlier, in the context of the fluctuation-dissipation theorem, the response is thermally dominated above the temperature of the susceptibility maximum, as opposed to being field dominated below it. Finally for $H_i/h_i = 0$, $G_{\pm}(0)$ is a constant, thus equation (2-23) lead to the temperature dependence of the peak susceptibility being given by:

$$\chi_m \propto t_m^{-\gamma} \qquad 2\text{-}27$$

providing a third power-law prediction from which the exponent γ can be estimated, again once a value for T_C has been made.

A comprehensive assessment of both the critical exponents and ordering temperature T_C acquired from ac susceptibility data can be made in an analogous manner to that carried out for magnetization data. Here, the scaling form summarized in equation (2-23) predicts that such data, when normalized to its peak value ($\chi(h_i,T_m)$), should fall on a universal curve when plotted against the argument ($h_i / |t_m|^{\gamma+\beta}$) of the scaling function (actually, its inverse, $t_m /(h_i)^{1/(\gamma+\beta)}$, which preserves the peak structure

[46, 47]).

$$\frac{\chi(h_i, T)}{\chi(h_i, T_m)} = |t_m| \cdot (h_i)^{-1/(\gamma+\beta)} \qquad 2\text{-}28$$

These exponent estimates can also be assessed in terms of the Widom equality $\gamma = \beta(\delta\text{-}1)$.

The types of measurements described above, and their subsequent analysis, are used extensively in later chapters. For the present, Figure 2.2 (b) illustrates the use of equation (2-28) to the corresponding data acquired on the colossal magnetoresistive pyrochlore $Tl_2Mn_2O_7$ [47]. Here the inclusion of data for which the critical peak structure is well resolved (specifically for applied fields exceeding about 500 Oe in this material) ensures that the critical contribution dominates the measured response.

In summary, the above discussion details the manner in which self consistent estimates for both critical exponents and ordering temperatures can be extracted from conventional magnetization data, and less widely exploited temperature and field-dependent ac susceptibility measurements. Similar ideas can also be applied to ferroelectric systems, where the appropriate variables are electrical polarization and susceptibility/dielectric constant.

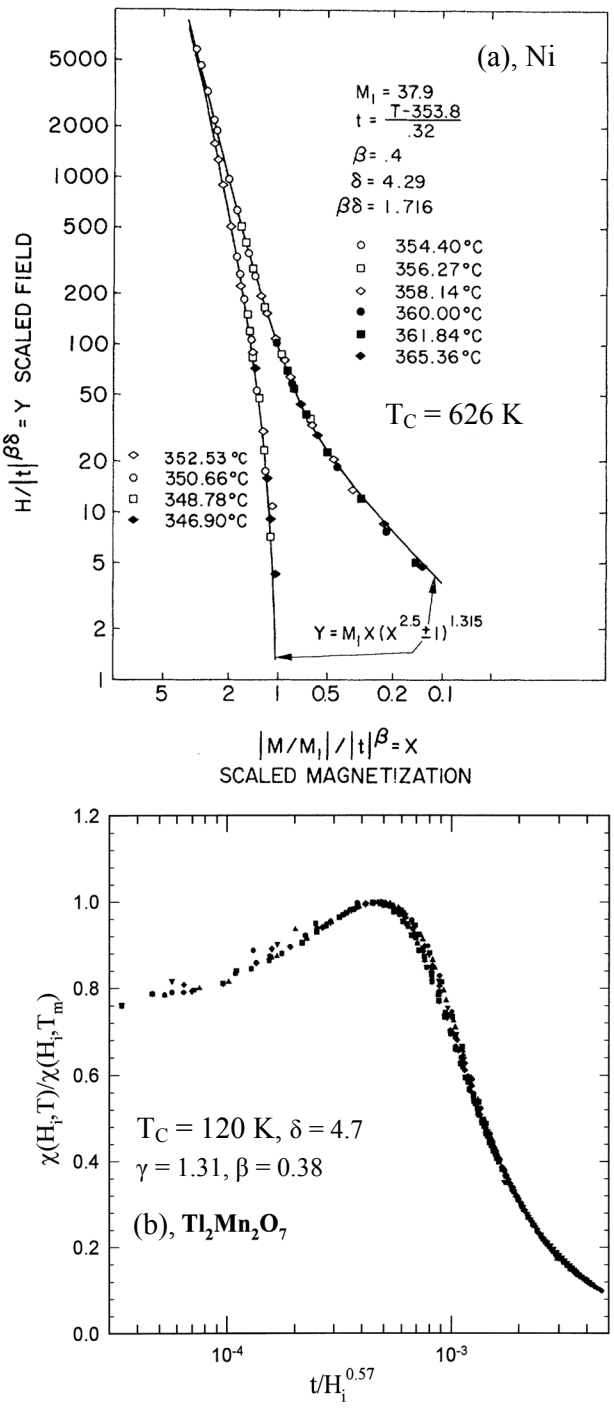

Figure 2.2 *Scaling behavior from magnetization and ac susceptibility in two selected magnetic systems. (a) Magnetization scaling in Ni with T_C = 626 K, δ = 4.4, γ = 1.31, β = 0.39, the curve on the left-hand side is for $T < T_C$ while the right-hand side is for $T > T_C$ [37]. (b) Ac susceptibility scaling in the CMR $Tl_2Mn_2O_7$ pyrochlore compound with T_C = 120 K, δ = 4.7, γ = 1.31, β = 0.38 [47].*

2.1.3 The Specific Heat and the Correlation Length

While not the principal focus of the present work, for completeness it should also be mentioned that specific heat and correlation function measurements are also important techniques, frequently used to characterize magnetic phase transitions with an accompanying set of critical exponents.

Specific heat measured at a constant pressure, $C_P(T)$, typically displays what is termed a λ-shaped anomaly near a phase transition [40]. The most well-known example probably is the ^{4}He system, in which the term "λ" transition was used to characterize the normal fluid ^{4}He-I to superfluid ^{4}He-II transition [49]. Similar characteristics also appear in magnetic systems. Near the ordering temperature T_C, $C_P(T)$ varies essentially logarithmically with temperature away from the critical temperature, T_C, viz., $C_P(T) \propto \ln|T - T_C|$. Specifically:

$$C_P(T) \propto \begin{cases} A_+ |T - T_C|^{-\alpha} (T > T_C) \\ A_- |T - T_C|^{-\alpha} (T < T_C) \end{cases} \qquad 2\text{-}29$$

Here α is the associated critical exponent (again characteristic of the predominant interactions in different magnetic systems). It should be noted, within the context of the present work, that the critical exponent deduced from resistive anomalies (dρ/dT) near the magnetic critical point, viz., $\ln(d\rho/dT) \propto -\alpha \cdot \ln|T - T_C|$ [50], has been demonstrated to be consistent with the heat capacity exponent [35, 49].

The correlation between spins located at different lattice sites in magnetic systems is characterized by the so-called spin-spin correlation length ξ. The correlation length

provides a measure of the range of spin order in a magnetic system at a given temperature, i.e., if the distance r between two spins is smaller than the scale set by ξ, the motion of these spins be correlated. Clearly as the temperature is lowered towards Tc from above, the correlation length ξ becomes larger, as confirmed indirectly from the neutron scattering experiment [35]. Near a continuous/second order magnetic phase transition, the spin-spin correlation length $\xi(T)$ exhibits – as do other characterisitc quantities – a power-law dependence on reduced temperature t_m, diverges at T_C:

$$\xi(T) \propto t_m^{-\nu} \qquad 2\text{-}30$$

In summary, the critical exponent values predicted by various model approached – Mean-Field, nearest-neighbor isotropic 3-Dimensional Heisenberg model, etc., are listed in Table 2.1 [51-53]. Magnetic systems which display the same exponents are said to lie in the same universality class, a situation that occurs despite such systems having quite different structural properties and ordering temperatures. The latter illustrates the unifying nature of the scaling concept outlined above.

Table 2.1 *Critical exponents predicted for various models.*

Critical Exponents	B	γ	δ
Acquisition Method	$\log M_S = \beta \cdot \log\lvert t_m \rvert$ $T < T_C$	$\log \chi = -\gamma \cdot \log\lvert t_m \rvert$ $T > T_C$	$\log M = -\frac{1}{\delta} \cdot \log\lvert H_i \rvert$ $T = T_C$
Mean-Field	0.5	1	3
3D Heisenberg	0.367	1.388	4.783
3D Ising	0.326	1.238	4.789
3D XY	0.349	1.318	4.780
Experimental value	0.3-0.4	1.2-1.4	4.2-5.0

2.2 Existence of a Griffiths-like Phase and its Influence on the Universality Class

For "uniform" ferromagnets, the power-law predictions described earlier have been tested extensively, and a range of values estimated for the corresponding critical exponents, as summarized in Table 2.1. However, there are a growing number of examples of FM system which display continuous PM-FM transitions accompanied by pseudo-critical behavior for which the accompanying "exponents" do not following any specific model predictions [18, 19, 54, 55]: the universality class is unknown. Such is the response of systems displaying a so-called Griffiths-like phase (GP) [56], a behavior linked with the presence of disorder.

In Griffiths' original treatment of a diluted two/three dimensional Ising ferromagnet [56], nearest neighbor exchange bonds of strength J occurred with probability p, with disorder being introduced via bonds of zero strength and probability (1-p). Below the percolation threshold, p_c, of the relevant lattice there is zero probability of establishing an infinite percolating "backbone" (in the language of continuous transitions, the correlation length does not diverge), correspondingly cooperative ferromagnetism is not established. However, for $p > p_c$, FM order is established, but not unexpectedly at a temperature $T_C(p)$ below that of the undiluted system [$T_C(p=1) = T_G$]. The temperature interval $T_C(p) < T < T_G$ defines a so-called Griffiths regime, a regime in which the system response is neither simply PM/Curie-Weiss (CW)-like nor is an

infinite percolating chain (the equivalent of a divergent correlation length) established; here the response is dominated by the largest cluster/correlated volume, leading to a temperature-dependence for the inverse susceptibility regarded as characteristic of such a phase [57], viz.:

$$\chi^{-1} \propto (T - T_C^{Rand})^{1-\lambda}, \quad \lambda < 0 < 1 \qquad 2\text{-}31$$

Here T_C^{Rand} is the associated random transition temperature, and λ is an exponent characterizing the strength of the Griffiths-like phase. Experimentally, the inverse dc/ac susceptibilities ($1/\chi(T)$) (measured in both zero field and in various small static biasing fields) are frequently employed to identify such a behavior via a characteristic depression evident for some of these data below the higher temperature CW line; an example of such behavior is shown in Figure 2.3 [58, 59]. However, as there is an ongoing debate as to whether such characteristics originate from magnetic disorder of the type originally envisaged by Griffiths, rather than from, or example, a polaron liquid [18 -20, 58], the term Griffiths-like has been adopted in related discussion.

This figure also shows the suppression of this Griffiths-like phase character by external fields of various strengths, a result can be understood in the following way. As the external field in the conjugate field for uniform ferromagnetism, increasing its magnitude promotes the growth of the latter at the expense of its disordered Griffiths counterpart. Increasing the external applied field thus causes the response to eventually revert to a conventional CW form. Another feature of Griffiths' original (nearest neighbor) model is that the growth of the correlation length necessarily terminates at a

missing bond. The application of external fields *near* the ordering temperature can, on the basis of the same conjugate field argument presented above, facilitate "frustrated" correlations to hop over the missing/unoccupied site, viz., the uniform applied field causes the magnetization in two regions adjacent to the site of a missing bond to become aligned/correlated. This effect is manifested by a sharp increase in magnetization in low applied magnetic fields along the critical isotherm. Experimentally, this low field regime is usually excluded from critical analysis for technical reasons (uncertainties in demagnetization corrections, domain wall effects, etc.,) [46], and the slower increasing of the magnetization with field (once technical saturation has been achieved beyond this low field region) translates into significantly increased estimates for the "exponent" δ (for example, $\delta = 28$ has been reported in a $La_{0.7}Ca_{0.3}MnO_3$ single crystal displaying GP-like features [18]).

While the disorder relevant to the formation of a Griffiths-like phase in $Tb_5Si_2Ge_2$ [58] (Figure 2.3 (a) summarizes its response) has been linked to the presence of FM clusters embedded into the PM background in the relevant (Griffiths) region, its origin in other systems such as doped manganites perovskites [55, 59-61], remains a subject of discussion. This issue is returned to later.

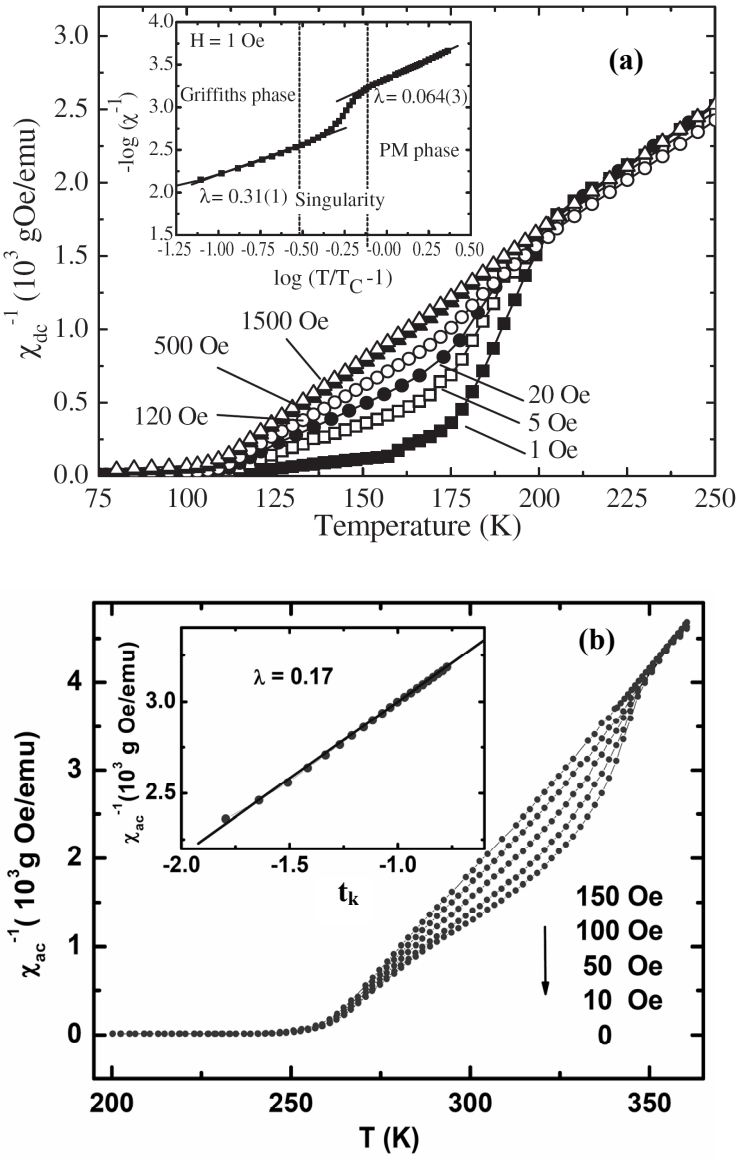

Figure 2.3 *The observation of Griffiths-like phase in different systems. (a) In magnetocaloric compound* $Tb_5Si_2Ge_2$ *[58], temperature dependent inverse susceptibilities measured under various static fields, as indicated in the figure, measured on warming. The inset shows the fitting to the Griffiths-like phase and PM states respectively at 1 Oe. (b) The inverse ac susceptibility, measured on warming following zero-field cooling under various (nominal) applied fields in* $La_{0.73}Ba_{0.27}MnO_3$ *[59]. The insert reproduces the zero field data on a log-log scale, with* $t_k = (T - T_C^{Rand}) / T_C^{Rand}$ *and* T_C^{Rand} *= 261 K; this form tests the power-law, equation (2-31), and yields* $\lambda \sim 0.17$.

2.3 Scaling the Anomalous Hall Effect

Thus far discussions regarding the nature of the phase transition and its universality class have focused on conventional approaches based on measurements of the magnetization and ac susceptibility, heat capacity and correlation length. As an intriguing corollary, the question arises as to whether magnetic critical behavior – specifically the universality class – can be deduced from magneto-transport data. In this context, following initial work by Craig, et.al., [50], numerous attempts have been made to establish such links in a variety of systems, including Ni [50] and (GaMn)As [62], amongst others [63]. Such studies, however, have focused almost exclusively on the temperature dependent of the zero-field resistivity, from which estimates of a single exponent – that describing the behavior of the heat capacity, mentioned earlier – have been deduced [50]. However, no comprehensive appraisal of the universality class of a magnetic phase transition, i.e., one comparable to that provided by the techniques mentioned earlier, has been made to date based solely on magneto-transport data.

This question is a fundamental one in the characterizing of correlations between magnetism and transport in the magnetic materials. Microscopically, such a correlation can be understood by introducing a coupling between, typically, itinerant s electrons (responsible for electrical conduction) and localized d electrons (responsible for the magnetization), viz., the s-d exchange interaction [64].

Such issues are timely, indeed controversial, as recent debate centered on scaling between magnetization and resistivity/conductivity [28, 30, 65] confirms. The latter frequently focus on the occurrence of the Hall effect in magnets as it reflects contributions from the magnetization, as, for example, in discussions on manganites [65]. A concern central in this debate is whether the Hall resistivity/conductivity or the *anomalous* Hall conductivity is the parameter linked directly with the magnetization, and, subsequently, how to best characterize this link/proportionality. These topics play a key role in any discussion of the correlation between magnetism and transport in magnetic materials, and form the basis of part of this thesis.

The Hall effect continues to be an important topic in condensed matter physics (two Nobel Prizes have been awarded for research on the topic of the Integer/Fractional Quantum Hall Effect [10]), and also plays an important role in modern electronics. It was discovered by Edwin Hall in 1879 at Johns Hopkins University [66]; Hall demonstrated the appearance of a transverse voltage or electric field in a metal in response to a longitudinal electric current and a perpendicular magnetic field. In 1880 Lord Kelvin [67] stated that "this is by far the greatest discovery that has been made to the electrical properties of metal since the time of Faraday – a discovery comparable with the greatest made by Faraday."

Such a transverse voltage arises in all materials – at least in part – from the deflection of charge carriers by the Lorentz force [40, 49, 64]:

$$\mathbf{F} = q(\mathbf{E} + \mathbf{v_d} \times \mathbf{B}) \qquad 2\text{-}32$$

Here q is the carrier charge, frequently the electronic charge, **E** is the electric field, $\mathbf{v_d}$ is the drift velocity, and **B** is the magnetic induction. This deflection leads to the accumulation of charge carriers on edges of the sample, which generates an electric field $\mathbf{E}_{\text{Hall}}$. When charge carriers experience a force from this latter electric field that balances the Lorentz force, the system is in a quasistatic equilibrium state.

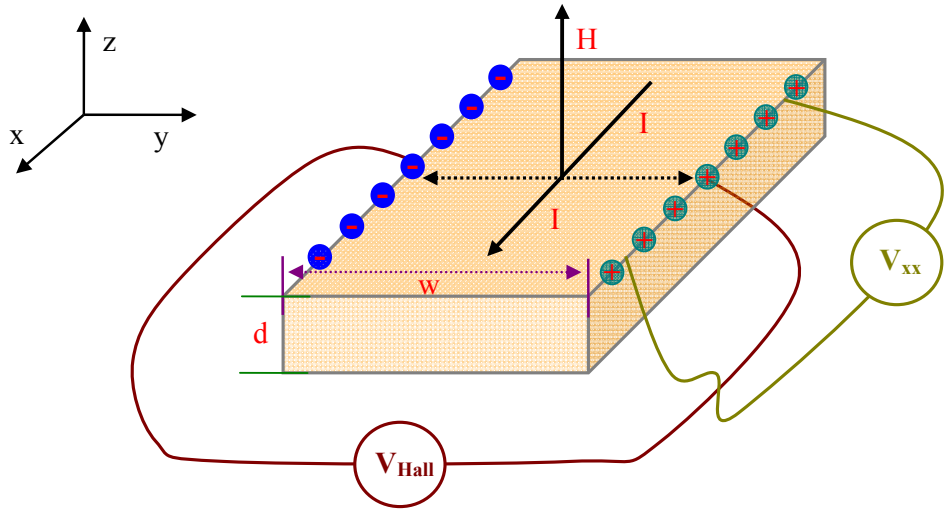

Figure 2.4 *Schematic illustration of magneto-transport measurements.* $V_{Hall}(\mathbf{H})$ *represents the Hall voltage,* $V_{xx}(\mathbf{H})$ *is the longitudinal voltage which yields the corresponding longitudinal resistivity* ρ_{xx}*, as mentioned in the text.*

In a semi-microscopic approach, the electric current **I** can be can be expressed as $\mathbf{I} = nqA\mathbf{v_d}$, where n is the carrier density, A = wd is the cross sectional area of a sample with width w and thickness d; with q = -e for electron conduction. With $\mathbf{v_d} = \dfrac{\mathbf{I}}{nqA}$, the Lorentz force $\mathbf{F_l} = q\mathbf{v_d}\mathbf{B}$ in the above geometry can be rewritten as:

$$\mathbf{F_1} = \frac{e\mathbf{BI}}{nqA} = \frac{\mathbf{BI}}{nwd} \qquad 2\text{-}33$$

The presence of the Hall electric field, $\mathbf{E}_{Hall}$, and the accompanying Hall voltage $V_{Hall}(\mathbf{H})$, due to carrier accumulation, results in a force $\mathbf{F_2}$:

$$\mathbf{F_2} = q\mathbf{E}_{Hall} == \frac{qV_{Hall}(\mathbf{H})}{w} \qquad 2\text{-}34$$

In equilibrium $\mathbf{F_1} = \mathbf{F_2}$, so:

$$\mathbf{F_1} = \mathbf{F_2} = \frac{\mathbf{BI}}{nwd} = \frac{qV_{Hall}(\mathbf{H})}{w} \qquad 2\text{-}35$$

Thus Hall voltage $V_{Hall}(\mathbf{H})$ reads:

$$V_{Hall}(\mathbf{H}) = \frac{\mathbf{BI}}{nqd} \qquad 2\text{-}36$$

This yields the Hall resistivity ρ_{xy}:

$$\rho_{xy} = \frac{V_{Hall}(\mathbf{H})}{\mathbf{I}} d = \frac{\mathbf{B}}{nq} = R_0\mathbf{B} \qquad 2\text{-}37$$

Here the Hall coefficient $R_0 = \frac{1}{nq}$ yields information on both the carrier type (R_0 will be negative (n-type) when q = -e and conduction by electrons dominate; in contrast, hole conduction (q = +e) yields a positive R_0 (p-type)), and density, n, from the magnitude of R_0 [40, 49, 64]. Its measurement thus plays an important role in the modern materials analysis.

Subsequently to the initial discovery, Hall (1881) found that the "Hall" resistivity (ρ_{xy}) in FM metals (Ni and Co) acquired an extra term which depended on the magnetic moments/magnetization of the samples; this extra term contribution is referred to as the anomalous Hall effect (AHE) [66]. The precise nature of this latter contribution,

however, remains controversial, as recent reports confirm [68]. Nevertheless, the evolution of AHE with temperature/field can be linked empirically – but directly – with the behavior of magnetization, M, via [69]:

$$\rho_{xy} = R_0 B + 4\pi R_S M \qquad 2\text{-}38$$

In this equation, B = [H + $4\pi(1-N_D)$M], and with the applied field H oriented perpendicular to the current flow, the demagnetization factor $N_D \approx 1$ for the typical Hall sample geometry measurement, when B ≈ H. R_S is the anomalous Hall coefficient; it exhibits strongly temperature/field-dependent features, reflecting various types of magnetic order [68-70]. As the parameter central to the later analysis, its' accurate evaluation is imperative; this, in turn, implies a careful subtraction of the contribution from R_0, a procedure outlined in detail below. Certainly, estimates for R_0 can be made with reasonable accuracy using a simple extrapolation technique in systems where the magnetization can be saturated by available field over the region of interest. However, when such a situation is not realized, a modified approach has to be adopted, as discussed in detail later for the $Fe_{0.8}Co_{0.2}Si$ system.

Using Ohm's law based expressions for the components of the conductivity tensor relevant for the Hall/longitudinal conductivity measurements [49, 70], viz.,

$$\sigma_{xy} = \frac{\rho_{xy}}{\rho_{xy}^2 + \rho_{xx}^2}; \rho_{xy} = \frac{\sigma_{xy}}{\sigma_{xy}^2 + \sigma_{xx}^2}$$
$$\sigma_{xx} = \frac{\rho_{xx}}{\rho_{xy}^2 + \rho_{xx}^2}; \rho_{xx} = \frac{\sigma_{xx}}{\sigma_{xy}^2 + \sigma_{xx}^2} \qquad 2\text{-}39$$

then in situations where $\rho_{xy} << \rho_{xx}$, these equation can be simplified: for the Hall

conductivity to $\sigma_{xy} \approx \frac{\rho_{xy}}{\rho_{xx}^2}$, and longitudinal conductivity to $\sigma_{xx} \approx \frac{\rho_{xx}}{\rho_{xx}^2} = \frac{1}{\rho_{xx}}$, suggesting the Hall conductivity (σ_{xy}) in magnetic systems can be expressed as:

$$\sigma_{xy} \approx \frac{\rho_{xy}}{\rho_{xx}^2} = \frac{R_0 H + 4\pi R_S M}{\rho_{xx}^2} \qquad 2\text{-}40$$

(Note that in the case where ρ_{xy} is comparable to ρ_{xx}, a higher order Taylor-like expansion has to be employed). Thus in ferromagnets, the total Hall conductivity σ_{xy} can be written as [70, 71]:

$$\sigma_{xy} = \sigma_{xy}^{O} + \sigma_{xy}^{A} \qquad 2\text{-}41$$

Here $\sigma_{xy}^{O} = R_0 H \Big/ \rho_{xx}^2$ is the ordinary Hall conductivity, so that the following expression for anomalous Hall conductivity σ_{xy}^{A} ensues:

$$\sigma_{xy}^{A} = \sigma_{xy} - \sigma_{xy}^{O} = \frac{4\pi R_S M}{\rho_{xx}^2} \qquad 2\text{-}42$$

As is clear from this equation, an accurate determination of the anomalous component σ_{xy}^{A} – and hence an evaluation of its dependence on the magnetization M – relies on a careful subtraction of the ordinary component, $\sigma_{xy}^{O} = \frac{R_0 H}{\rho_{xx}^2}$, an issue discussed below. Two additional – and important – points also emerge for this equation.

First, once the system's magnetization is measured, it provides a means of identifying the dependence of R_S on ρ_{xx}, a result can be used to establish the dominant mechanism underlying the AHE in the system [72]. This will be demonstrated for the magnetic semiconductor $Fe_{0.8}Co_{0.2}Si$ later in this thesis. To proceed further, the issue of the dependence (or lack thereof) of R_S on the longitudinal resistivity, ρ_{xx}, also needs to

be addressed. This concern has been raised repeatedly since the initial reports of AHE; R_S has various been taken as constant [73], or to display either a linear [74] or a quadratic [75, 76] dependence on ρ_{xx}, reflecting the dominant mechanism involved. As demonstrated below, this issue can be addressed in a manner analogous to that used in scaling approaches for the magnetization, viz., by introducing a function:

$$G(R_S, \rho_{xx}) = 4\pi R_S/\rho_{xx}^2 \qquad 2\text{-}43$$

then equation (2-42) can be rewritten as $\sigma_{xy}^A = M \cdot G(R_S, \rho_{xx})$. Correspondingly, a plot of σ_{xy}^A versus M will not only yields the functional form of $G(R_S, \rho_{xx})$ directly, but will also indicate the appropriate dependence (if any) of R_S on ρ_{xx} (i.e., if R_S varies as ρ_{xx}^Q, a plot of $\log(\sigma_{xy}^A / M)$ versus $\log(\rho_{xx})$ will yield the index Q, and hence the required dependence of R_S). The detailed application of this approach is demonstrated for $Fe_{0.8}Co_{0.2}Si$ in the first section of Chapter 5.

Second, essentially the converse of the above, if the dependence of R_S on ρ_{xx} can be, or has been, established by other means [77], then it is possible to determine the behavior of the magnetization M from measurements of σ_{xy}^A. The latter has important consequences in systems with reduced dimensions/dimensionality for which the associated magnetic signal is weak. This approach will be applied to an epitaxial $Ga_{0.98}Mn_{0.02}As$ microstructure (with approximate thickness 50 nm, width 240 μm and length 1600 μm) in the second section of Chapter 5; in this material theoretical predictions (based on a Mean-Field model) yield a quadratic dependence R_S on ρ_{xx} arising from an intrinsic AHE. The objective here is to use the above idea to link the

anomalous Hall conductivity directly to the magnetization; such a link facilitates the use of a novel modification of the conventional form critical analysis outlined earlier in this chapter.

Specifically, such proportionality would lead to the usual Arrott-Noakes/scaling equation of state equation (2-18) being expressed in terms of the anomalous Hall conductivity σ_{xy}^{A}, viz.,

$$\left(\frac{\sigma_{xy}^{A}}{\sigma_1}\right)^{1/\beta} = \frac{T_C - T}{T_C} + \left(\frac{H_i}{\sigma_{xy}^{A}}\right)^{1/\gamma} \qquad 2\text{-}44$$

in which σ_1, as M_1 in equation (2-18), is a material specific constant. The critical exponents appropriate for the corresponding transition will then be those which linearize the anomalous Hall conductivity – field data plotted in the above form. Correspondingly, the intercepts of such linearized plots on the perpendicular axis ($(\sigma_{xy}^{A}/\sigma_1)^{1/\beta}$), i.e., at $H_i = 0$, should then provide estimates of the "spontaneous" anomalous Hall conductivity $\sigma_{xy-Spon}^{A}$, equivalent to the spontaneous magnetization, while those on the ordinate axis ($(H_i/\sigma_{xy}^{A})^{1/\gamma}$) will yield a quantity analogous to the (inverse) initial susceptibility $1/\chi_i(T) = (\partial H_i/\partial M)_{H_i=0}$. The isotherm that passing through the origin (the "critical" anomalous Hall conductivity isotherm, $\sigma_{xy}^{A}(T_C)$), enables an estimate of the ordering temperature T_C to be made (the temperature at which a spontaneous Hall conductivity $\sigma_{xy-Spon}^{A}$ first emerges). Self-consistency can then be achieved using a similar procedure to that discussed in relation to the "conventional" analysis of the magnetization. Specifically, the replacement of M by σ_{xy}^{A} in the usual scaling law equation of state equation (2-19) will lead to the following expression for

the anomalous Hall conductivity:

$$\sigma_{xy}^{A}(H_i, t_m) = |t_m|^{\beta} F_{\pm}\left(\frac{H_i}{|t_m|^{\gamma+\beta}}\right) \qquad 2\text{-}45$$

$F_{\pm}$ being an (unspecified) scaling function. Equation (2-45) then yields a set of power-law dependences for σ_{xy}^{A} on field and (reduced) temperature close to T_C, analogous to those deduced earlier for the magnetization. Here such power-laws become – for the spontaneous anomalous Hall conductivity $\sigma_{xy-Spon}^{A}(H_i = 0, t_m = |T\text{-}T_C|/T_C)$ as a function of (reduced) temperature –

$$\sigma_{xy-Spon}^{A}(0, t_m) \propto t_m^{\beta} (T < T_C) \qquad 2\text{-}46$$

Along the critical isotherm T_C ($T = T_C$, $t_m = 0$), the field dependence of the anomalous Hall conductivity reads:

$$\sigma_{xy}^{A}(H_i, T = T_C) \propto H_i^{1/\delta} \qquad 2\text{-}47$$

While for the quantity H_i / σ_{xy}^{A}, proportional/analogous to the inverse initial susceptibility, one obtains:

$$H_i / \sigma_{xy}^{A} \propto t_m^{\gamma} (T > T_C) \qquad 2\text{-}48$$

Equations (2-46) – (2-48) can then be applied to the appropriate intercept values so estimated, and the ensuing exponents values deduced from them substituted back into the "linearized" plots, and repeating this process – with *small* adjustments to T_C (< 0.1 K here) – until the (modified) Arrott plots and the ensuing power-laws yield the same exponent values. A final, comprehensive assessment of both exponent values and the T_C estimate would be provided by plotting the anomalous Hall conductivity against the argument of the scaling function in equation (2-45), i.e., $\sigma_{xy}^{A}(H_i, t_m) / |t_m|^{\beta}$ versus

$H_i / |t_m|^{\gamma+\beta}$, with the anticipation that a scaling plot analogous to Figure 2.2 (a) ensues. The detailed application of this process will be presented in Chapter 5.

In summary, this approach provides a novel pathway for establishing the universality class from the anomalous Hall conductivity, a clear reflection of the fundamental coupling between magnetic and transport properties.

Chapter 3

Experimental Apparatus and Sample Preparation

The magnetic and transport measurements on CMR manganites and magnetic semiconductors were carried out using a commercial Quantum Design Physical Property Measurement System (PPMS Model 6000) [78, 79]. Below a summary of features of this commercial product is first offered, complemented by a brief description of sample preparation.

3.1 Quantum Design Physical Property Measurement System

The PPMS (Model 6000) magnetometer/susceptometer consists principally of a dewar containing liquid helium, and a measurement probe immersed in the helium bath, a pump to control pressure, and a magnet power supply. These parts together enable the magnetic field, temperature, time dependent magnetization, ac susceptibility, resistivity, and Hall resistivity data to be acquired. These measurements can be performed in the temperature range 1.8 K – 350 K in fields from -90 kOe to +90 kOe. The discussion starts with a description of the PPMS measurement probe, Figure 3.1, followed by magnetization measurements, then ac susceptibility measurements, and finally transport

measurements.

3.1.1 PPMS Measurement Probe

The first important feature of the PPMS probe is its temperature control, which is realized by using a cooling annulus. Around the boiling point of ^{4}He at 4.2 K under 1 atmosphere pressure, two different operational modes have been adopted to produce temperatures in the range 1.8-350 K. Above 4.2 K, temperatures are controlled using the helium vapor pressure. Specifically, for cooling, helium gas is drawn into the cooling annulus through the so-called impendence tube (which plays a pivotal role in the control process) by a vacuum pump, and this cools the sample space. For warming, a block heater, set in the base of sample space, heats the sample space to the predetermined temperature. In contrast, temperatures below 4.2 K are achieved by pumping the helium in the cooling annulus, thus decreasing the pressure of the liquid helium and hence its temperature. Temperature down to 1.8 K can be achieved using this method.

The second important feature of the PPMS probe is the control of dc/ac magnetic fields. This is accomplished using a superconducting solenoid (made from NbSn) immersed in liquid helium, thus maintaining the solenoid in its superconducting state (below T_C). The solenoid is fed from a unipolar power supply, the current from which controls the strength of dc magnetic field (H) (the latter can be approximated, using Ampère's law, by $H \propto N \cdot I / z$, where I is the charging current, N is numbers of turns,

and z is the length of the solenoid [64, 80]).

Ac measurements require the application of an driving field $H_{ac}\sin(\omega t)$, generated by a second, non-superconducting coil, which is part of the ac measurement system (ACMS), Figure 3.2. The response of the sample to this ac field is picked up by the detection coil. In particular, the ACMS provides a platform to perform both dc and ac magnetic measurements without changing the hardware configuration.

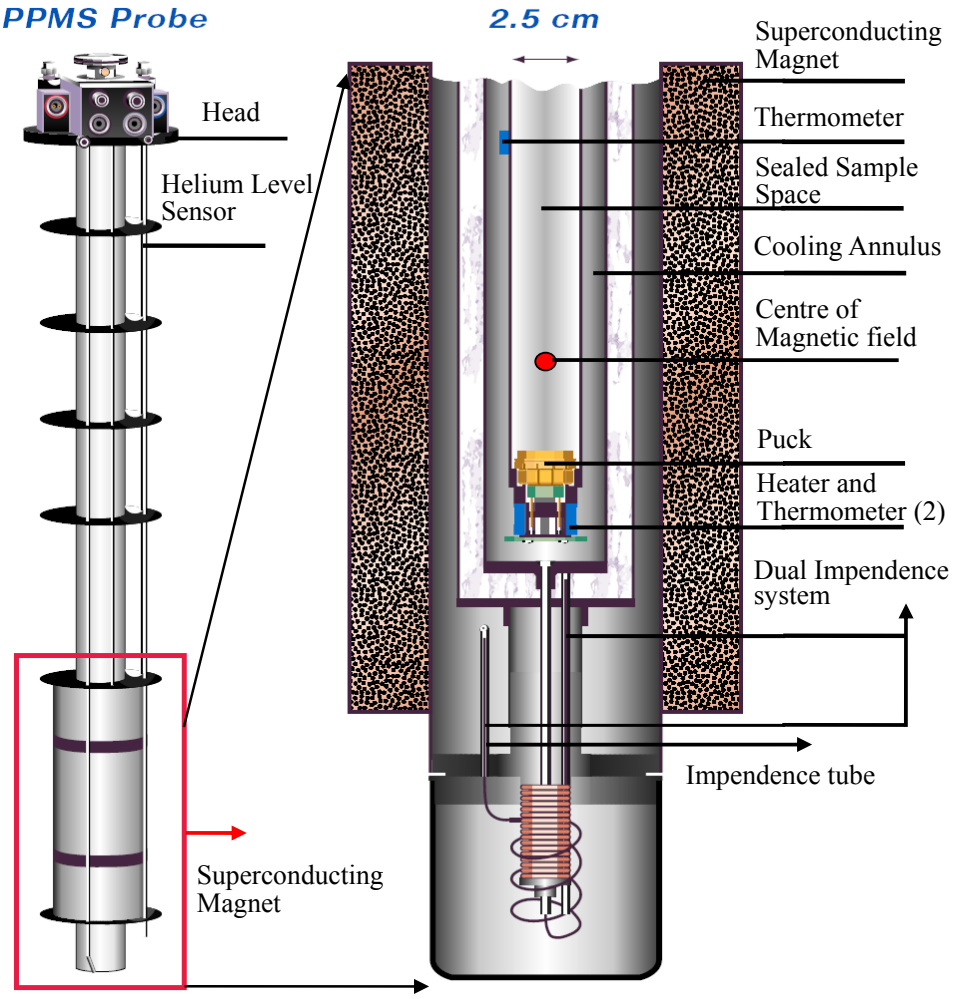

Figure 3.1 *Schematic illustrations for the PPMS probe and the enlarged cross section.*

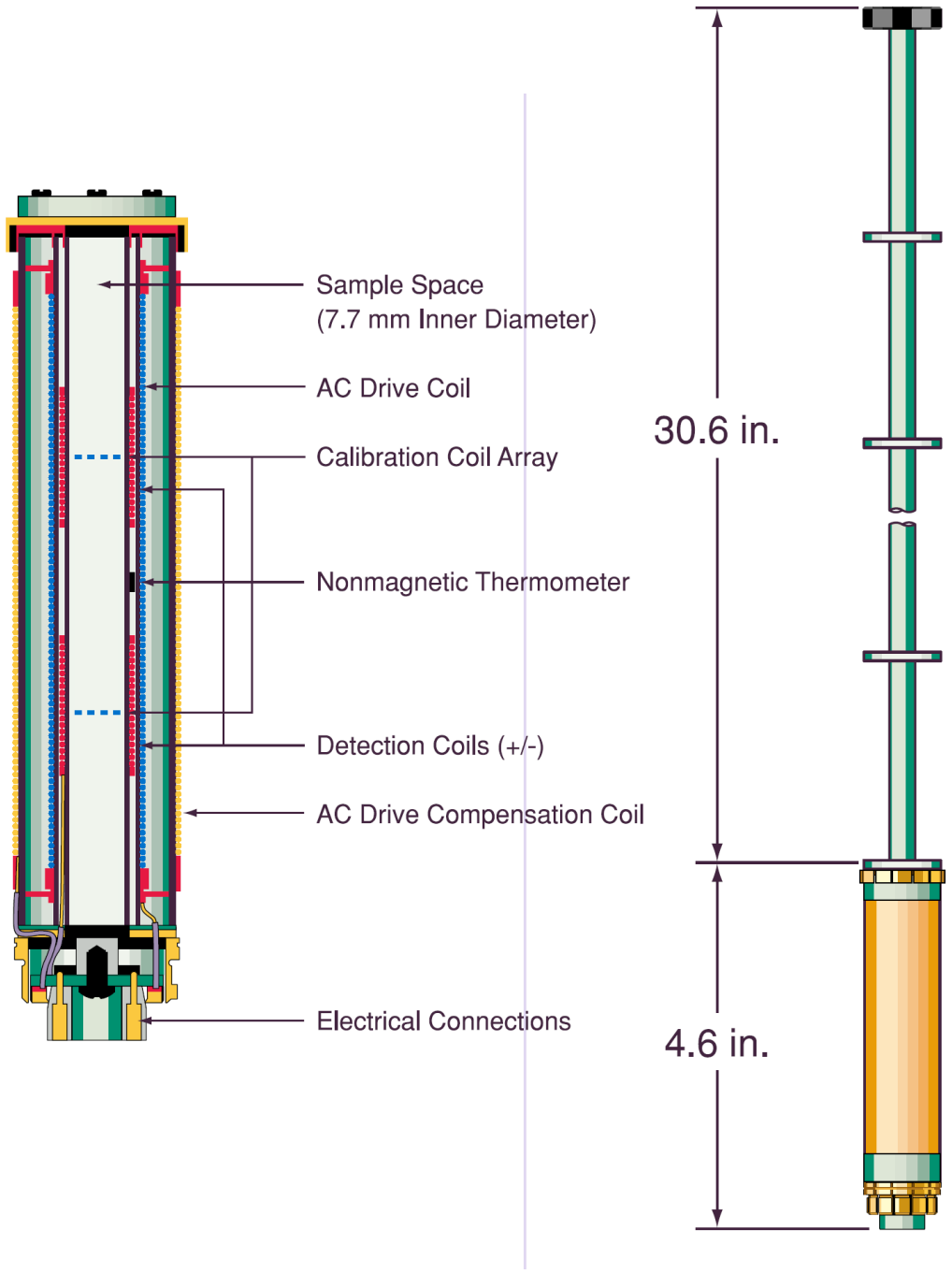

Figure 3.2 *Diagram of the ACMS inert and coil set.*

3.1.2 DC Magnetization Measurements

Numerous methods have been utilized to detect the magnetization of materials, these include extraction techniques, torque methods, superconducting quantum interference devices (SQUID), and anomalous Hall effect magnetometry. The principal approach used in the present work is the extraction method. Here, an external static magnetic field (H) magnetizes the sample, after which the induced magnetization is measured. The mechanism underlying the extraction method is simply the rapid motion (over a time interval (t_e)) of a sample between two sets of detection coils which induces a voltage ε governed by Faraday's law [64, 80], viz.,

$$\varepsilon = -\frac{\partial \Phi_B}{\partial t_e} \qquad 3\text{-}1$$

where Φ_B is the magnetic flux through the circuit. The signal in the detection system is then determined by both the extraction speed (t_e) and the total magnetic flux (which is proportional to the magnetization of sample). A dc servo motor in the PPMS provides a scanning speed of approximately 100 cm/sec. This enables many repeated scans to be made in a short period, and by averaging these scans, random measurement errors can be dramatically reduced. The sensitivity for dc magnetization measurement in the present PPMS is about 2.5×10^{-5} emu, and, typically, a 5 scan method was employed in this thesis. The PPMS thus offers a comprehensive platform for studying the dc magnetic response under conditions of varying temperature, magnetic field, and, where appropriate, time.

3.1.3 Ac Susceptibility Measurements

Ac susceptibility measurements also provide an important characterization of magnetic properties, especially magnetization "dynamics". In the present system this is accomplished by the application of a small ac driving field $H_{ac}\sin(\omega t)$, (superimposed on the static field generated by superconducting coil), which induces a frequency/time dependent magnetization $M_{ac} = (dM/dH) \cdot H_{ac} \sin(\omega t)$. At low frequencies, and in the absence of hysteresis, ac measurements are similar to their dc counterpart, viz., from the definition of susceptibility as $\chi = dM/dH$, the latter reflects the slope of the M(H) curve. At high frequencies however, ac measurements do not simply the slope of the (static) M(H) curve, significant differences occur. These are generally parameterized through the use of two components: the magnitude of the susceptibility (χ) and its phase shift angle, (Φ). Equivalently, the ac susceptibility can be expressed in terms of its real and imaginary parts, as follows:

$$\begin{cases} \chi' = \chi\cos(\Phi) \\ \chi'' = \chi\sin(\Phi) \end{cases} \Leftrightarrow \begin{cases} \chi = \sqrt{(\chi')^2 + (\chi'')^2} \\ \Phi = \tan^{-1}(\chi''/\chi') \end{cases} \qquad 3\text{-}2$$

The imaginary part, χ'', reflects dissipative processes in the system. In particular, both the real and imaginary parts are sensitive to the presence of magnetic phase transitions, as has been extensively discussed [64]. Although the PPMS enables a wide range of parameters to be recorded, including χ', χ'', Φ, temperature (T), driving field amplitude and frequency ($H_{ac}\sin(\omega t)$), as well as the superimposed magnetic field H, for

the purpose of studying magnetic phase transitions (the principal focus of the present work) the evolution of χ' as a function of superimposed dc fields H and temperatures (T) will suffice.

Since ac measurements are essentially sensitive to the slope of the M(H) curve, viz., $\chi = {dM}/{dH}$, and not the absolute value of magnetic moment, an extremely small change in magnetization can be detected even when the absolute magnetization is large. Consequently, ac magnetometry is very useful for studying magnetic phase transitions. In particular, the PPMS offers an extremely high sensitivity for the susceptibility measurements, 1×10^{-8} emu, with the facility for varying the amplitude of the ac driving field over the range 0.2 mOe $\leq H_{ac} \leq$ 10 Oe rms, at frequencies from 10 Hz to 10 kHz.

These advantages are partially offset by the fact that measurements performed in low static fields (typically, H < 20 Oe in the present PPMS) can be somewhat uncertain due to trapped flux (i.e., a residual magnetic field) in the superconducting solenoid. Some caution thus needs to be exercised in studying the magnetic response – especially the dc response – in low fields.

Demagnetization effect corrections are also important for finite magnetic systems. These originate from the establishment of "free magnetic poles" induced at either end of a sample by the application of magnetic fields. The effect of the latter can be treated as a demagnetizing field $H_d = N_D M$, where N_D is a shape-dependent demagnetization factor and M the magnetization. The resultant internal magnetic field H_i reads [64]:

$$H_i = H_a - N_D M \qquad 3\text{-}3$$

where H_a is the applied field. In principle, N_D can only be accurately calculated for the sample of ellipsoidal shape. For non-ellipsoidal samples, a theoretical approximation for the average internal field can be made [64]. Experimental estimates for the demagnetization factor N_D can be made as follows: with the real/true susceptibility defined as $\chi_t = dM/dH_i$ while the measured susceptibility is given by $\chi_m = dM/dH_a$, then equation (3-3) can be rewritten as:

$$\frac{1}{\chi_t} = \frac{1}{\chi_m} - N_D \Rightarrow \begin{cases} \chi_t = \dfrac{\chi_m}{1 - N_D \chi_m} \\ \chi_m = \dfrac{1}{N_D + 1/\chi_t} \end{cases} \qquad 3\text{-}4$$

Consequently, following the theoretical prediction of an infinite susceptibility ($1/\chi_t$ = 0) in the zero field at FM phase transition in the thermodynamic limit, then the measured susceptibility is limited to $\chi_m = 1/N_D$. Experimentally, the maximum of measured susceptibility ($T = T_C$) can thus be used to estimate the demagnetization factor N_D. In the present studies these latter estimates have been found to be consistent (within experimental uncertainty) with those found from magnetization data, viz., M(H) – H curves measured in low fields close to T_C, where the slopes of these (shearing) curves also approximate to the demagnetization factor [46-48].

3.1.4 Transport Measurements

Transport measurements, specifically longitudinal and Hall resistivities, were also carried out in the PPMS using a Model 7000 AC Transport Controller (ACT). This ACT incorporates a precision current source and voltage meter. The precision current source has a resolution 2×10^{-8} A and maximum current of 2 A. Its variable frequency (in the range 1 Hz to 1 kHz) provides a greater sensitivity resulting from the application of signal filtering techniques.

Transport measurements were made using a conventional four-probe technique to minimize the effects of contact resistance. The ACT probe was inserted into PPMS in the configuration shown in Figure 3.3 (a). The head of this probe incorporates a horizontal rotator with the angle resolution of 0.02°, which enables the out-of plane anisotropic magnetoresistance (AMR) to be measured (Figure 3.3 (b)). A homemade modification to this probe enables in-plane AMR measurements to be made in our lab (again, with the angle resolution of 0.02°), Figure 3.3 (c).

Hall measurements are well known to be very difficult perform experimentally; this arises due to unwanted contributions from the longitudinal voltage originating from a possible mismatch in the location of two Hall leads. This can cause marked difficulties when the Hall voltage is extremely small. This difficulty can be overcome by an experimental strategy based on varying the direction of the applied magnetic field. As indicated in equation (2-31), the Hall voltage can be written as $V_{Hall}(\mathbf{H}) = -\frac{\mathbf{BI}}{ned}$; thus

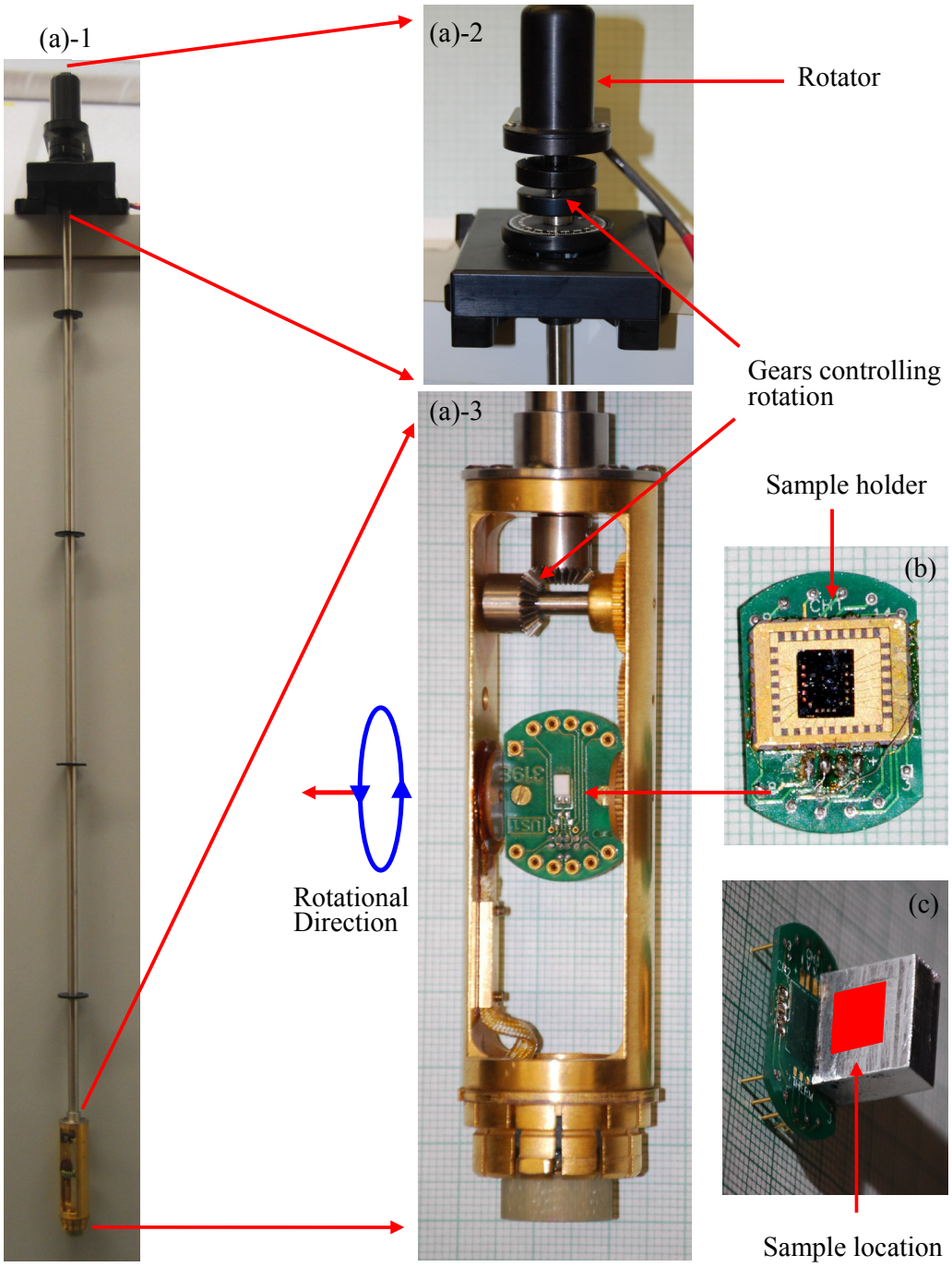

Figure 3.3 *Images of the transport measurement probe and sample holders. (a) The transport measurement probe. The sample holders for AMR measurements are given in (b) for out-of plane rotation and (c) for in-plane rotation.*

changing the direction of magnetic field leads to a change in sign for $V_{Hall}(\mathbf{H})$ as $V_{Hall}(\mathbf{H}) = -V_{Hall}(-\mathbf{H})$. However, under the same conditions the longitudinal voltage, V_{xx}, retains the same value ($V_{xx}(\mathbf{H}) = V_{xx}(-\mathbf{H})$). This latter can then be used to cancel any possible contribution from the longitudinal voltage by scanning the field from positive to negative and calculating the "real" Hall voltage, $V_{Hall\text{-}Real}(\mathbf{H})$, as:

$$V_{Hall\text{-}Real}(\mathbf{H}) = \frac{1}{2}\left[V_{Hall}(\mathbf{H}) - V_{Hall}(-\mathbf{H})\right] \qquad 3\text{-}5$$

This technique was used to estimate the real Hall voltage throughout this thesis.

3.2 Sample Preparation

Single crystals for three series of manganites, $La_{1-x}Ca_xMnO_3$ ($0.18 \leq x \leq 0.27$), $La_{1-x}Ba_xMnO_3$ ($x \leq 0.33$), $Pr_{1-x}Ca_xMnO_3$ ($x = 0.27, 0.29$), were supplied by Dr. Yakov Mukovskii at the Moscow State Steel and Alloys Institute, Moscow, Russia. They were made using a floating zone technique [81], and had a typical size, before cutting, shown in Figure 3.4. Electron probe microanalysis [81] revealed a variation of some 2% in the Mn content through the middle portions of such rod-shaped specimens, while the variation *in general* of the Ca level can approach 10%. The samples used in this thesis were cut from such central regions – which were all revealed to be single phased by powder X-ray diffraction data – and displayed a significantly lower Ca variation, as discussed in relation to the data summarized in Table 4.1 below.

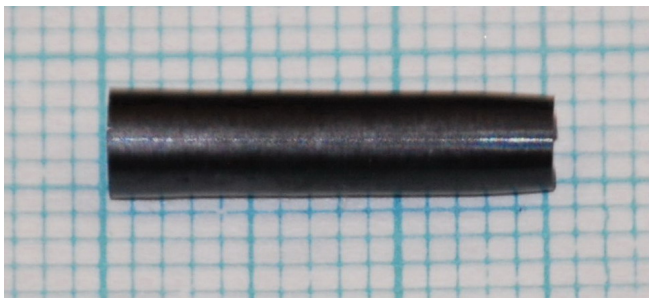

Figure 3.4 *The image of a typically sized single crystal. Here, $La_{0.75}Ca_{0.25}MnO_3$ on top of standard (1 cm) graph paper.*

Ac susceptibility and dc magnetization measurements were performed on the same piece of each sample (with typical size 4×1×1 mm^3). For transport measurements, contacts to samples of typical dimensions 5×1×1 mm^3 were made by compressing indium "pads" over current/voltage gold conducting wires embedded in grooves cut into the sample by a diamond wire saw (and contact resistance was typically less than 1 Ω).

The $(La_{1-y}Pr_y)_{0.7}Ca_{0.3}Mn^{16/18}O_3$ ($y \leq 0.85$) series were polycrystalline specimens made using standard solid state reaction techniques [82]. These samples were calcined at temperatures between 1270 – 1570 K for 120 hours from La_2O_3, Pr_6O_{11}, MnO_2 and $CaCO_3$; the oxygen exchange was made by annealing the samples in quartz tubes under an ^{18}O atmosphere at 1270 K for 40 hours. The compositions of all the samples were checked at various temperatures using a powder neutron diffraction technique [82]. A comprehensive investigation on the evolution of the magnetic properties of this system has been published by Dr. Pomjakushin and colleagues (Paul Sherrer Institute at Switzerland). We acknowledge their generosity in sending us the raw zero field ac susceptibility data of this system.

The polycrystalline magnetic semiconductor of nominal composition $Fe_{0.8}Co_{0.2}Si$ was made in our laboratory using standard argon arc melting techniques. In an attempt to improve homogeneity, it was inverted and remelted several times, followed by annealing at 1300 K for four days in an evacuated quartz tube. Powder X-ray diffraction data revealed a single phase structure. Electric contacts to this $Fe_{0.8}Co_{0.2}Si$ specimen ($3\times1\times0.15$ mm^3) were made using silver epoxy (EPO-TEK H20E, Epoxy Technology, INC.), and were done with the aid of a high resolution optical microscope to minimize possible Hall bar mismatch effects: the current and voltage leads were made from 35 μm gold (bonding) wire.

A $Ga_{0.98}Mn_{0.02}As$ layer (50 nm in thickness) was grown on a semiconducting GaAs substrate using a molecular beam epitaxy (MBE) technique, by Dr. Werner Wegscheider's group at the University of Regensburg, Germany. A 10 nm GaAs layer was grown on top of the $Ga_{0.98}Mn_{0.02}As$ to avoid oxidization. The sample was subsequently etched into a microstructural form approximately 240 μm wide and 2 mm long, using the standard optical lithography by Dr. Can-Ming Hu's group at the University of Manitoba. Electrical contacts were made using a commercial electrical wire bonder in the Electrical and Computer Engineering Department at the University of Manitoba.

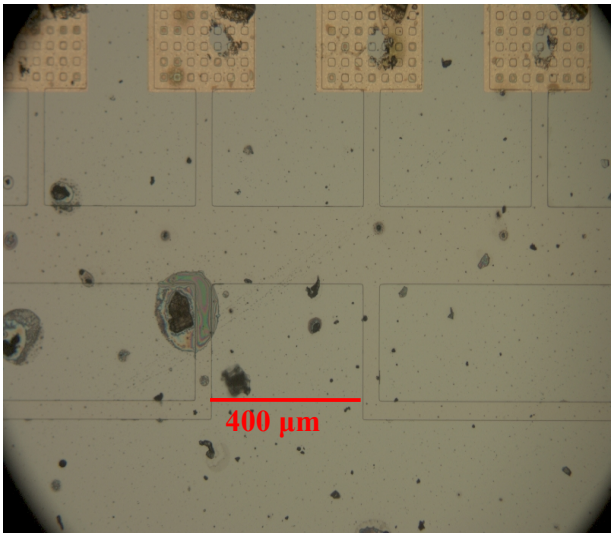

Figure 3.5 *The optical image of the lithographically-made* $Ga_{0.98}Mn_{0.02}A$ *sample. This structure includes 2 sets of Hall bars used to make transport measurements.*

Chapter 4

Magnetic and Transport Properties of Colossal Magnetoresistance Manganites

Transition metal oxides exhibit fascinating properties; these include multiferroicity, superconductivity, and CMR [2-4]. Many of these appear to be critically sensitive to differing types/levels of ion substitutions; for example, varying the Sr substitution level in the $La_{1-x}Sr_xCuO_4$ cuprate system can induce a superconducting, AFM or a non-Fermi liquid state [3]. Other striking examples occur in CMR perovskites manganites [2-4], where the earliest studies were initiated more than half a century ago [83]

4.1 Manganites Physics

An appropriate discussion of CMR Mn perovskites begins with the undoped parent compound, $LaMnO_3$. The latter exhibits a nearly cubic structure [2-4, 83], with the following valence states for the constituent ions, $La^{3+}Mn^{3+}(O^{2-})_3$; the latter are consistent with charge neutrality and result in a magnetic moment on the Mn^{3+} ($3d^4$) site alone, La^{3+} and O^{2-} containing no unpaired electrons. This configuration is illustrated in Figure 4.1, and consists of a larger La ion situated in the centre of the essentially cubic structure, surrounded by Mn and O ions. At each cubic corner, there is an oxygen octahedron with a Mn ion at its center, which gives rise to a cubic crystal field potential at the central Mn site.

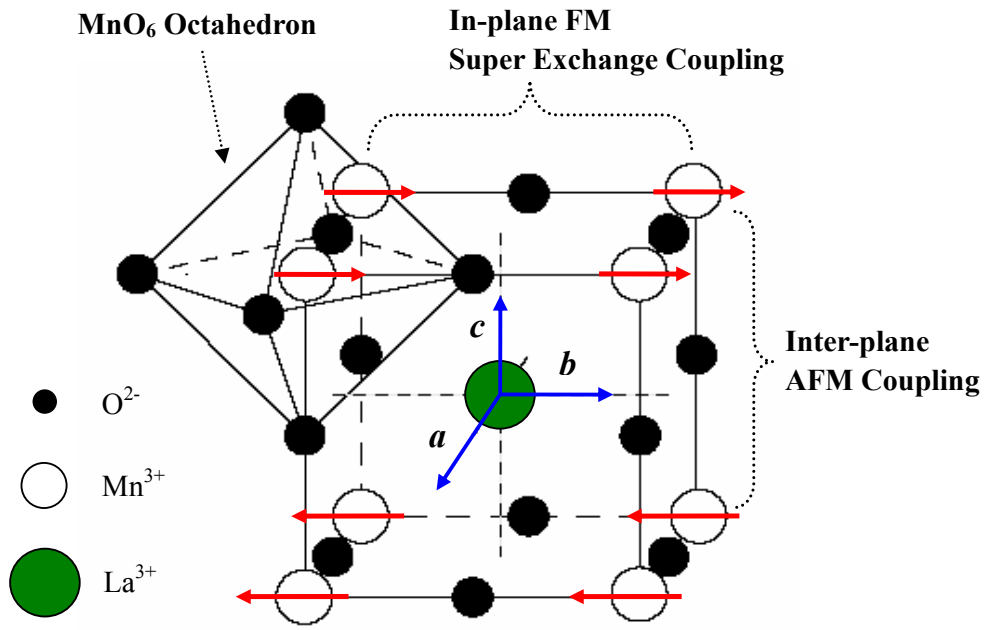

Figure 4.1 *Sketch of the structure of the undoped parent $LaMnO_3$ [4]. The FM in-plane coupling and the inter-plane AFM coupling result from a slight departure from cubic symmetry: the lattice constants are: a = 5.747 Å, b = 5.537 Å and c = 7.693 Å.*

The $3d^4$ electronic state on the Mn^{3+} ions displays 5-fold orbital degenerate ($2l + 1 = 5$) in free space, a degeneracy that is lifted by the crystal field, Figure 4.2 (a). The resulting splitting, which depends on the Coulomb repulsion with neighboring oxygen 2p orbitals, produces a higher energy orbital doublet e_g state described by so-called $d_{x^2-y^2}$ and $d_{3z^2-r^2}$ wave functions, the lobes of which are directed towards the six oxygen ions located at the corners of octahedron, and a lower lying, and hence localized, orbital triplet t_{2g} state. This latter state is characterized by d_{xy}, d_{yz}, and d_{zx} – like wave functions, which point between the oxygen ions, Figure 4.2 (b). The energy splitting between these states approaches 1 eV [3, 4]. A strong Hund's exchange coupling ($J_H \approx$ 3eV), ensures the expected FM coupling between these four Mn 3d electrons – the "spin-down" states being much higher in energy – leading to a "core spin" of $S = \frac{3}{2}$ being associated with the lower lying t_{2g} triplet, to which the single e_g electron aligns parallel, leading to a total spin $S = \frac{1}{2} \times 4 = 2$ (resulting in a corresponding moment of 2 μ_B), Figure 4.2 (a).

A further complication arises due to a Jahn-Teller (JT) splitting of the upper e_g doublet – a splitting resulting from a distortion in the oxygen octahedron surrounding each Mn ion – of some $E_{JT} \approx 0.25$ eV, Figure 4.2 (a). With thermal energies at room temperature amounting to some $k_BT \approx 0.026$ eV $<< E_{JT}$, these e_g electrons remains immobile due to the Pauli Exclusion Principle. Undoped $LaMnO_3$ is thus a "Mott" insulator. In addition, such a JT distortion is co-operative, leading to the presence of orbital ordering, viz., orbitals that are aligned along specific directions, Figure 4.2 (c).

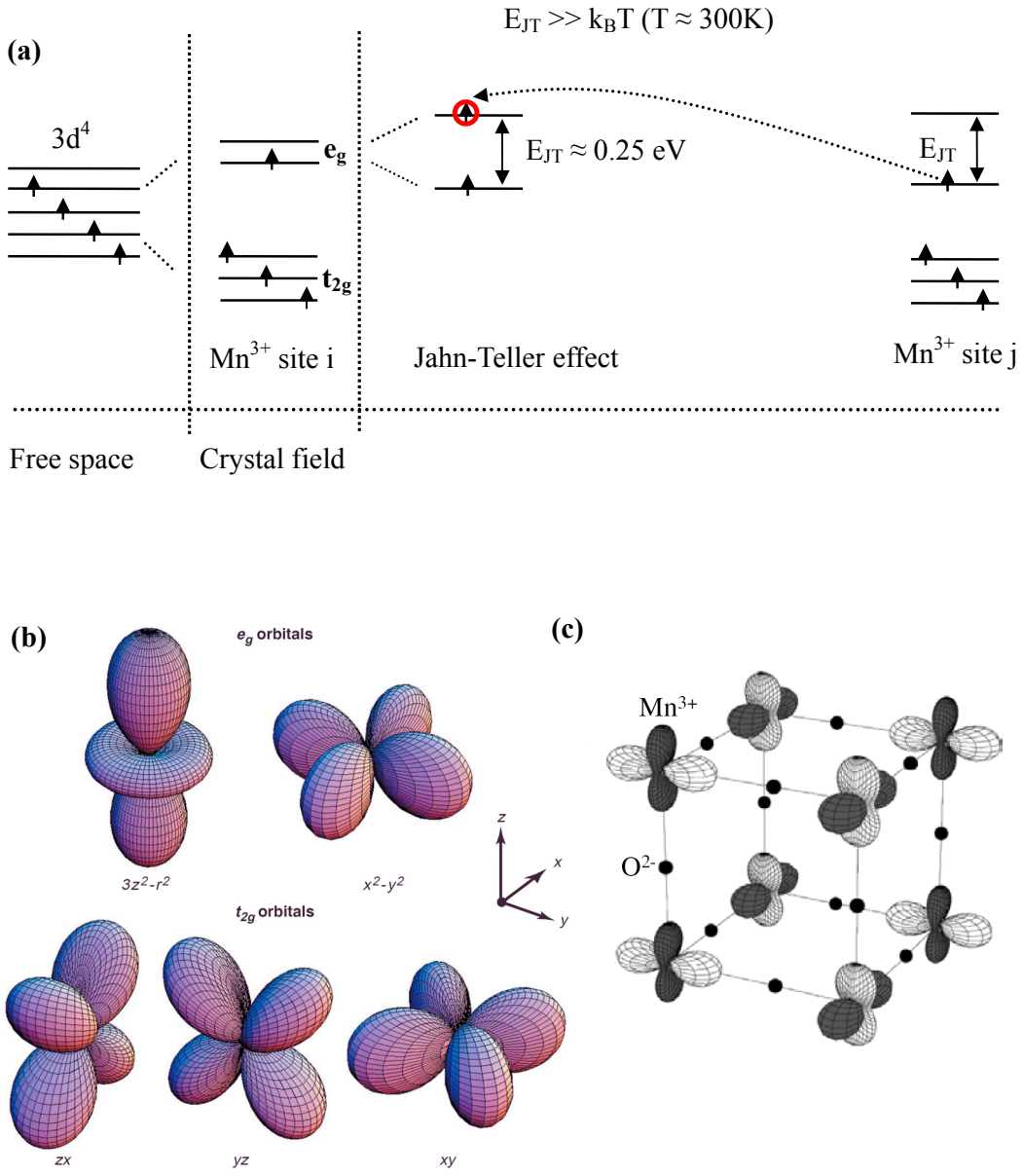

Figure 4.2 *Splitting of Mn 3d-states under a cubic crystal field [4]. (a) The 5-fold orbitally degenerate Mn d-states are split into an e_g doublet and a lower lying t_{2g} triplet under this field. The subsequent Jahn-Teller effect splits the e_g resulting in an energy gap $E_{JT} \approx 0.25$ eV. (b) The e_g and t_{2g} orbital distributions. (c) The three dimensional network of orbital ordering in $LaMnO_3$.*

As can also be seen from the structural diagram, Figure 4.1, moment bearing Mn ions are too well separated to interact via Direct Exchange – direct overlap of the Mn 3d wave functions – but couple via intermediate O ions via the so-called Super Exchange (SE) interaction [84]. An understanding of the latter is not as well established as for Direct Exchange, with the magnitude and sign of such SE interactions being determined by the semi-empirical Kanamori-Goodenough-Anderson (KGA) rules [84]. The rules indicate that the sign of this coupling (i.e., FM or AFM) is determined by the Mn-O-Mn bond length and bond angle. In the specific case illustrated in Figure 4.2 (c), the SE between an empty and a half-occupied orbital gives rise to a FM nearest-neighbor interaction within the ab-plane, whereas the corresponding interaction between two half-filled orbitals along the c-direction is AFM [85]. The undoped parent compound is thus an AFM insulator.

In the present context, doping of the parent $LaMnO_3$ compound is usually represented by $(A^{3+})_{1-x}(B^{2+})_x(Mn^{4+})_x(Mn^{3+})_{1-x}(O^{2-})_3$. Here A is a trivalent rare-earth ion (i.e., La, Pr…) and B a divalent alkaline earth cation (i.e., Ba, Ca…) which substitutes randomly at the trivalent rare-earth ion "A" sites. To ensure charge neutrality under the above form of substitution requires a corresponding (x) fraction of Mn ions be converted from a 3+ to a 4+ valence state. Such doping produces a range of fascinating phenomena, including CMR, an MIT, AFM and FM insulating states, charge ordering (CO), amongst others [3, 4]. Typical examples are given in Figure 4.3 – (a) resistivity for $La_{1-x}Sr_xMnO_3$ [86] and (b) phase diagram for $La_{1-x}Ca_xMnO_3$ [16].

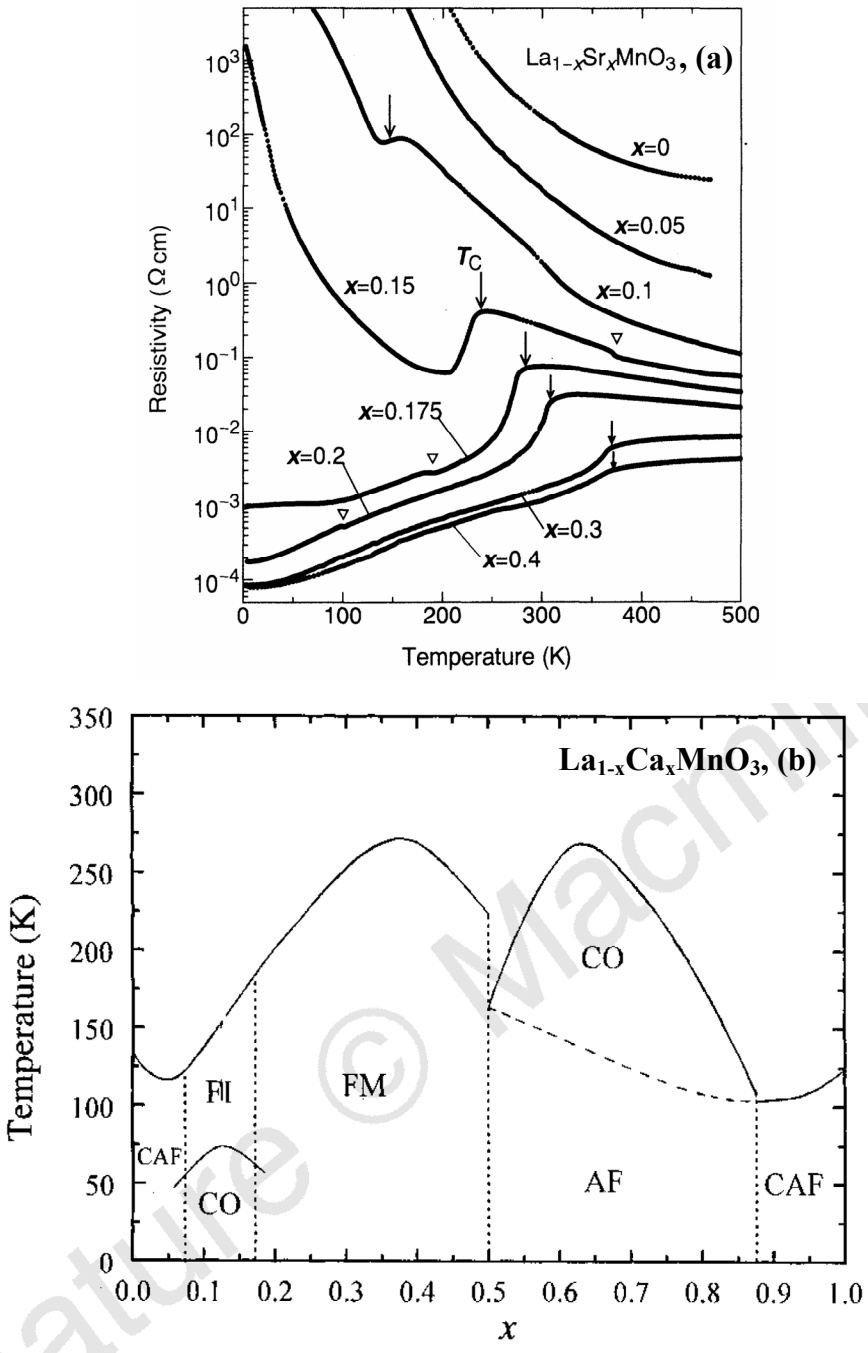

Figure 4.3 *Temperature dependent resistivity for $La_{1-x}Sr_xMnO_3$ and the phase diagram for $La_{1-x}Ca_xMnO_3$. (a) Resistivity as a function of temperature in the $La_{1-x}Sr_xMnO_3$ system [86]. Arrow indicates T_C and ∇ indicates the structural phase transition temperatures. (b) Phase diagram of $La_{1-x}Ca_xMnO_3$ showing magnetic and structural phase boundaries [16]. The horizontal axis represents the doping level x. Phases include CO, AF, canted AFM, FM metal and FM insulator. The unlabelled region of the phase diagram has neither magnetic nor charge ordering.*

A simple picture for spin-dependent DE was given earlier in the introduction [3, 4, 12], here a more detailed discussion is provided. The underlying mechanism, as depicted in Figure 1.3, is based on the result that e_g electrons are no longer prevented by the Pauli Exchange Principle from hopping from a Mn^{3+} ion to neighboring Mn^{4+} ion, since this latter state is now unoccupied. Nevertheless due to the Mn ions' separation mentioned above, this hopping must still proceed via an intervening O^{2-} ion. This process is thus envisioned as the jump of an e_g electron from a Mn^{3+} site into an O^{2-} 2p state, accompanied simultaneously by a second 2p electron hopping into an empty e_g electronic state on the adjacent Mn^{4+} ion: hence the term DE.

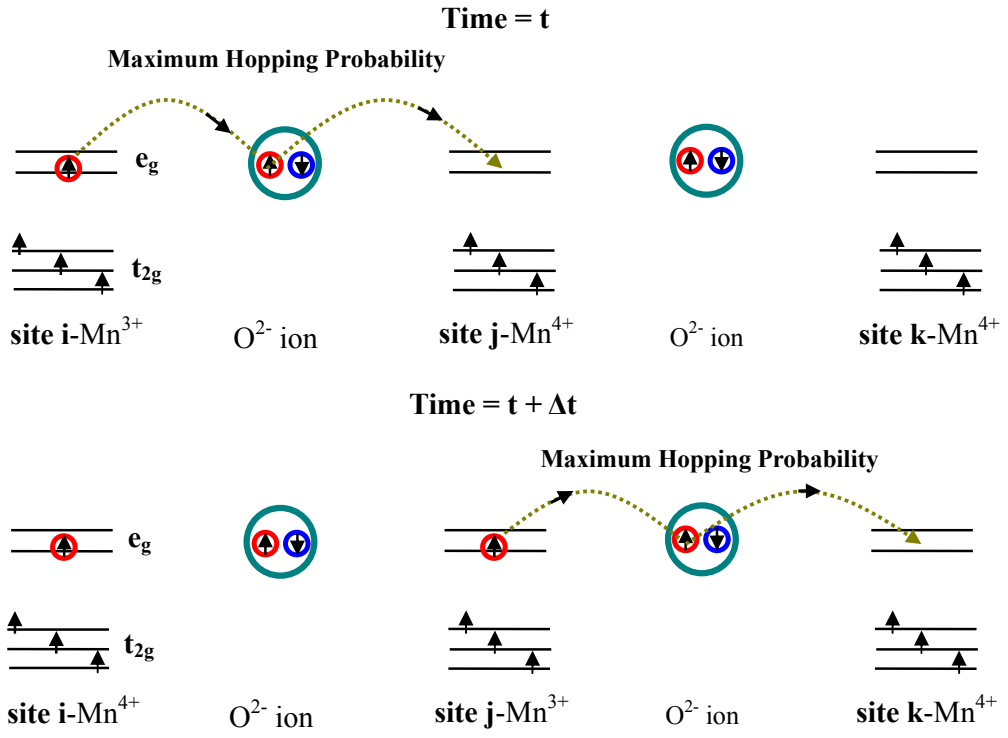

Figure 4.4 *Detailed illustration of spin-dependent Double Exchange. The time/location variation of e_g electrons in Mn^{3+}-O^{2-}-Mn^{4+} chains, leading to a alternating Mn^{3+}/Mn^{4+} distribution in real space.*

There is, however, no mechanism through which the participating electronic spin(s) can change orientation. Thus, given the strong Hund's rule coupling discussed above, this hopping channel is only fully open when the corresponding Mn spins are parallel. The transfer of non-aligned spins is a much higher energy process. Consequently, the establishment of ferromagnetism (parallel alignment of Mn spins) occurs coincidentally with metallicity (high hopping probability/conductivity). Thus if the spins of neighboring Mn^{3+} and Mn^{4+} ions are not aligned, namely, in the spin disordered, high temperature PM state, e_g electron hopping between them will be blocked, leading to an insulating/semiconducting state. Correspondingly, the hopping probability between such sites (i and j) can be described by hopping or transfer integrals of the form [3, 4, 12, 13]:

$$t_{ij} = t_0 \cos\left(\frac{\theta_{ij}}{2}\right) \qquad 4\text{-}1$$

where $0 < \theta_{ij} < 180^\circ$ is the angle between adjacent core (t_{2g}) spins at sites i and j. Thus as $\theta_{ij} \to 0$, the relevant core spins are parallel, resulting in a maximum hopping probability $t_{ij} = t_0$; by contrast, when $\theta_{ij} \to 180^\circ$, the core spin are anti-parallel and hopping is blocked, $t_{ij} = 0$; the latter provides an explanation of the onset of metallicity with FM ordering, as depicted in Figure 4.4. Furthermore, the application of magnetic field *close* to the FM ordering temperature, aligns the Mn spins and enhances the conductivity considerably, hence the occurrence of CMR.

While DE thus provides a qualitative explanation of CMR, more recent experiments indicate that this model fails: (**a**) to reproduce the large resistivity/low conductivity of disordered PM phase [14]. This latter result, coupled with evidence of

strong electron-phonon coupling revealed through experiments such as a giant oxygen isotope effect [24], has led to the specific concept of polaron mediated transport (discussed in more detail below) and the general idea that CMR systems exhibit coupling not only between charge and spin, but also orbital and vibronic degrees of freedom. (**b**) The occurrence of a FM insulating state conflicts with such a DE picture with coincidental ferromagnetism and *metallicity* [15]. Ferromagnetism in insulating manganites requires some other mechanism – such as SE – to be dominant, a point returned in detail below. These latter two features illustrate the considerable complexity exhibited by these manganites, aspects which are the focus of the present study.

The substitution/doping level (x) has an important influence on the magnetic, transport, and structural properties of these systems. First, as mentioned earlier, it modulates the Mn ion valence state to ensure charge neutrality; the ratio of Mn^{3+}/Mn^{4+} is proportional to x/(1-x), and such a coexistence of Mn^{3+} and Mn^{4+} gives rise to the term mixed-valence manganite. Doping also changes the total magnetic moment, leading to a saturation magnetization M_{SAT}:

$$M_{SAT} \propto 4 \cdot x + 3 \cdot (1 - x) = 4 - x \qquad 4\text{-}2$$

Second, doping produces vacancies in the e_g electron states at a rate of x per Mn site, often referred to as hole-doping, with a filling factor n_{hole} of the e_g electron conduction band given as: $n_{hole} = 1 - x$ [3, 4]. Third, the accompanying mismatch in the size of ions occupying the "A" site leads to a distortion in the crystal structure, frequently characterized by the average "A"-site radius, $\langle r_A \rangle$. The various ionic radii relevant for

the ions utilized in the present work are: Mn^{3+} = 0.70 Å; Mn^{4+} = 0.53 Å; O^{2-} = 1.32 Å; La^{3+} =1.22 Å; Pr^{3+} = 1.18 Å; Ca^{2+} = 1.18 Å; Ba^{2+} = 1.47 Å; Sr^{2+} = 1.31 Å [87]. The corresponding variance, φ, in the A-site radii is;

$$\varphi^2 = (< r_A^2 > - < r_A >^2) \qquad 4\text{-}3$$

and the "tolerance factor":

$$t_f = \frac{< r_A > + < r_O >}{\sqrt{2}(< r_{Mn} > + < r_O >)} \qquad 4\text{-}4$$

Here $<r_{Mn}>$ and r_O are the average radii of the Mn and O sites, respectively [3, 4]. Different doping levels change the Mn^{3+}/Mn^{4+} ratio, and with the varying ionic radii accompanying substitution, distortions occur, with the crystal structure transforming from being initially nearly cubic perovskite ($t_f \approx 1$), through rhombohedral ($0.96 < t_f < 1$), to an orthorhombic ($t_f < 0.96$) structure [3, 4]. This is accompanied by reductions in the Mn-O-Mn bond angle below the "ideal" value of 180º, thus changing the hopping probability of conduction electron, a process that can lead to charge-localization, and hence an insulating state [88]. Thus, while doping creates a wide variety of physical features in manganites, here only a brief description of two such features – charge and orbital ordering – will be given. Other relevant characteristics such as a MIT, a Griffiths-like phase, and FM insulating behavior, will be discussed in sections 4.2 – 4.5.

In analogy with magnetite (Fe_3O_4), the concept of CO was initially applied to the mixed valence manganite $La_{0.5}Ca_{0.5}MnO_3$ by Goodenough [89]; here the periodic arrangement of Mn^{4+} and Mn^{3+} ions – for which strong Coulomb repulsion reduces the hopping probability – is shown Figure 4.5. $La_{0.5}Ca_{0.5}MnO_3$ actually undergoes two

transitions, to a FM conducting state at T_C = 220 K, and subsequently to an AFM insulating state at T_N = 150 K (AFM insulating) [90]. Between these two transitions the magnetization and resistivity exhibit hysteresis. Such effects are not prevalent in the samples studied here, as they are far removed from this half-doping regime.

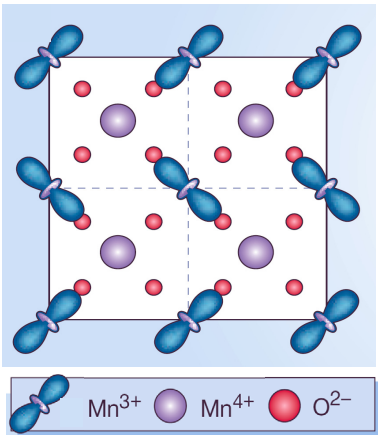

Figure 4.5 *Illustration for the simultaneous charge/orbital ordering in* $La_{0.5}Ca_{0.5}MnO_3$. *This is reproduced from [91].*

In this thesis four different systems have been studied; $La_{1-x}Ca_xMnO_3$ ($0.18 \leq x \leq 0.27$), $La_{1-x}Ba_xMnO_3$ ($x \leq 0.33$), $(La_{1-y}Pr_y)_{0.7}Ca_{0.3}Mn^{16/18}O_3$ ($y \leq 0.85$), $Pr_{1-x}Ca_xMnO_3$ ($x = 0.27, 0.29$).

4.2 Phase Diagram for $La_{1-x}Ca_xMnO_3$ ($0.18 \leq x \leq 0.27$)

Regarded as a prototypical CMR system, $La_{1-x}Ca_xMnO_3$ exhibits a complex phase diagram as a function of temperature and chemical substitution levels (x) [3, 4, 16, 92]. Below x = 0.125, it displays a canted-AFM insulating ground state, which evolves into a FM insulating state as the doping level is increased to $0.125 \leq x \leq 0.18$. Increasing the doping levels to $0.22 \leq x \leq 0.50$ result in the emergence of a FM metallic state accompanied by CMR. For $0.50 \leq x \leq 0.85$, the so-called hole-doped regime, CO, AFM insulating states predominates, terminating in a canted-AFM insulating ground state in the doping range $0.85 \leq x \leq 1$. The present study focuses on the doping range where both ferromagnetism and metallicity first emerge, viz., $0.18 \leq x \leq 0.27$, although these detailed measurements confirm they do not emerge coincidentally.

4.2.1 Evolution of Metal - Insulator Transition and Griffiths-like Phase

Estimates for the saturation magnetization M_{SAT} were obtained from extrapolations of M versus H^{-1} plots from magnetic isotherm measured at 2 K; these estimates are consistent (within experimental uncertainty of ~ 1–4%, considerably smaller than the *general* composition variation throughout an entire typical boule, referred to earlier) with the theoretical, spin-only values and the nominal compositions (Table 4.1). Thus, no evidence supporting appreciable spin canting was found.

Composition	x=0.18	x=0.19	x=0.20	x=0.21	x=0.23	x=0.25	x=0.27	x=0.30
Structural Properties								
$\langle r_A \rangle$ (Å)	1.2096	1.2092	1.2088	1.2084	1.2078	1.2072	1.2063	1.2051
Tolerance Factor (t_f)	0.9361	0.9297	0.9234	0.9174	0.9172	0.9169	0.9167	0.9163
φ (Å)	0.0138	0.0141	0.0144	0.0147	0.0151	0.0156	0.0159	0.0165
Transport Properties								
ρ (T = 2K) (Ω cm)	120	4	1.72×10^{-4}	1.85×10^{-4}	1.79×10^{-4}	1.77×10^{-4}	1.82×10^{-4}	1.6×10^{-4}
E_a (mev)	161.2	160.8	135.8	135.3	132.7	126.9	119.2	--
ρ_0 (10^{-8} Ω cm $T^{-3/2}$)	20.5	13.7	8.3	6.8	5.6	4.2	3.1	--
Magnetic Properties								
β	0.37	0.38	0.37	0.10	0.41	0.51	0.12	0.12
γ	1.38	1.34	1.38	1.65	1.35	1.15	1.63	1.63
δ	4.8	4.8	4.8	20	5.2	18	~28	28
E (emu/g Oe)	5.4 ± 0.1	5.3 ± 0.1	5.2 ± 0.1					
T_C (K)	171	173	179	182	185	189	232	212
T_G (K)	No	256	No	252	232	224	275	232
GP	No	Yes	No	Yes	Yes	Yes	Yes	Yes
$M_S(0)$ (emu/g)	94.45	90.92	91.87	90.71	91.24	92.75	89.05	--
$M_{SAT}(0)$ (emu/g)	95.23	91.44	91.93	91.25	91.73	92.93	89.62	--
H_C (Oe)	35	36	12	10	9	7	6	--
D (meV $Å^2$)	65	62	65	120	118	123	126	160

Table 4.1 *Parameters characterize $La_{1-x}Ca_xMnO_3$ ($0.18 \leq x \leq 0.30$) single crystals. Data of x = 0.30 are taken from [18], "--" stands for no data available.*

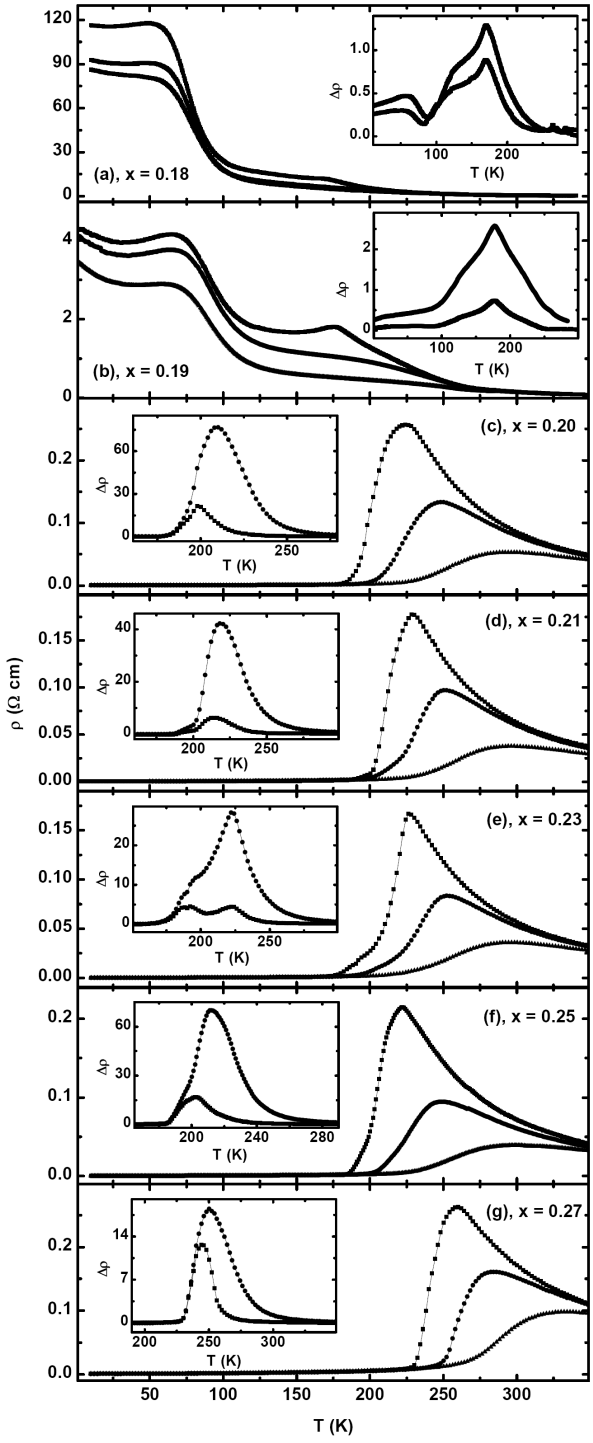

Figure 4.6 *Temperature dependent (magneto)resistivities for $La_{1-x}Ca_xMnO_3$ ($0.18 \leq x \leq 0.27$). Main body, ρ(T,H), measured on warming following zero field cooling (ZFC), in static magnetic fields of 0 (top), 30 k Oe, and 90 k Oe (bottom). The insets show the magnetoresistivities, $\Delta\rho = [\rho(0) - \rho(H)]/\rho(H)$. Figures (a) – (g) correspond to x = 0. 18, x = 0.19, x = 0.20, x = 0.21, x = 0.23, x = 0.25 and x = 0.27, respectively.*

The temperature dependent resistivities ρ(T,H) measured in static magnetic fields of 0, 30 kOe, and 90 kOe are reproduced in Figure 4.6; the insets display the accompanying magnetoresistance ($\Delta\rho = [\rho(0) - \rho(H)]/\rho(H)$). The narrow composition steps intentionally chosen in the present study suggest that with but a 1% change in the Ca substitution/doping level, in particular, from x = 0.19 to x = 0.20, the ground state resistivities exhibit a dramatic decrease exceeding 10^4 [93]. As a consequence of this suppression, at x = 0.20 and above, this system displays a temperature dependent MIT, the temperature of which increases with increasing Ca substitution, with an attendant reduction in the associated peak resistivity and the accompanying magnetoresistance/CMR, Δρ. Over the composition range studied here, the ratio of ρ(10 K,0) between metallic and insulating ground state approaches 10^{-6}, consistent with a range of previous reported results [93]. As discussed in more detail later, the nature of this insulating ground state remains controversial.

Before discussing the implications of the magnetization/susceptibility data, a detailed examination of the (temperature dependent) transport properties is appropriate. This is performed via a quantitative fits to these data of various model predictions. In particular, the temperature dependence of the resistivity in the high temperature/PM insulating phase (empirically characterized by $d\rho/dT < 0$) above T_C in many doped Mn perovskites has been fit to a modified Arrhenius law of the form [94, 95]:

$$\rho(T) = \rho_0 T^z \exp(E_a / k_B T) \qquad 4\text{-}5$$

Here E_a is related to the polaron formation energy, while the exponent z can assume

values of 0, 1, or 3/2 depending on the physical model invoked - 0 for simple thermally activated hopping, 1 for adiabatic and 3/2 for non-adiabatic small polaron hopping. The prefactor ρ_0 contains a carrier density factor characterized by $4x(1–x)/V$, where the term x(1-x) accounts for site occupation effects, with V being the double-cell volume. For the present single crystals, the non-adiabatic small polaron hopping model (z = 3/2) provides the most convincing fit to available data in the high temperature regime (as judged by the associated standard deviation). Such fits to zero-field data are shown in Figure 4.7 using the linearized form of equation (4-5), namely, $\ln(\rho(T)/T^{3/2})$ versus T^{-1}, simultaneously yield estimates for E_a and ρ_0. These E_a estimates (listed in Table 4.1) fall within the general range reported for a variety of manganites [95]. Figure 4.7 (h) reproduce these E_a and ρ_0 estimates as a function of doping level x. Here a sharp decrease in the activation energy, E_a, is clearly evident on crossing the compositionally modulated MIT boundary, a precursor effect appearing in the PM regime prior to the establishment of insulating ground state properties below x = 0.20. This observation appears to be consistent with the results of small angle neutron scattering [96], and recent high temperature inverse ac susceptibility/transport data [20]. While the prefactor ρ_0 also decreases with increasing doping level, it does so less abruptly, providing a weaker indication from the PM regime regarding the disappearance of metallicity.

Note that in the x = 0.18 single crystal, apart from the principal maximum in MR near T_C ($\Delta\rho = [\rho(0) – \rho(H)]/\rho(H)$), two additional transitions are evident via secondary peaks in MR, shown in the inset in Figure 4.6 (a). Such peaks corresponds to a low

temperature, structurally driven transition near $T_B \approx 70$ K accompanying a decrease in orthorhombicity, and a higher temperature Jahn-Teller transition around $T_{JT} \approx 270$ K (a pseudo-cubic to orthorhombic structural change [97]); the latter is also evident in the inverse ac susceptibility. Such additional features are not evident at higher doping levels, $0.19 \leq x \leq 0.27$, where the magnetoresistance/CMR, $\Delta\rho$, displays no systematic trend as a function of doping level (x).

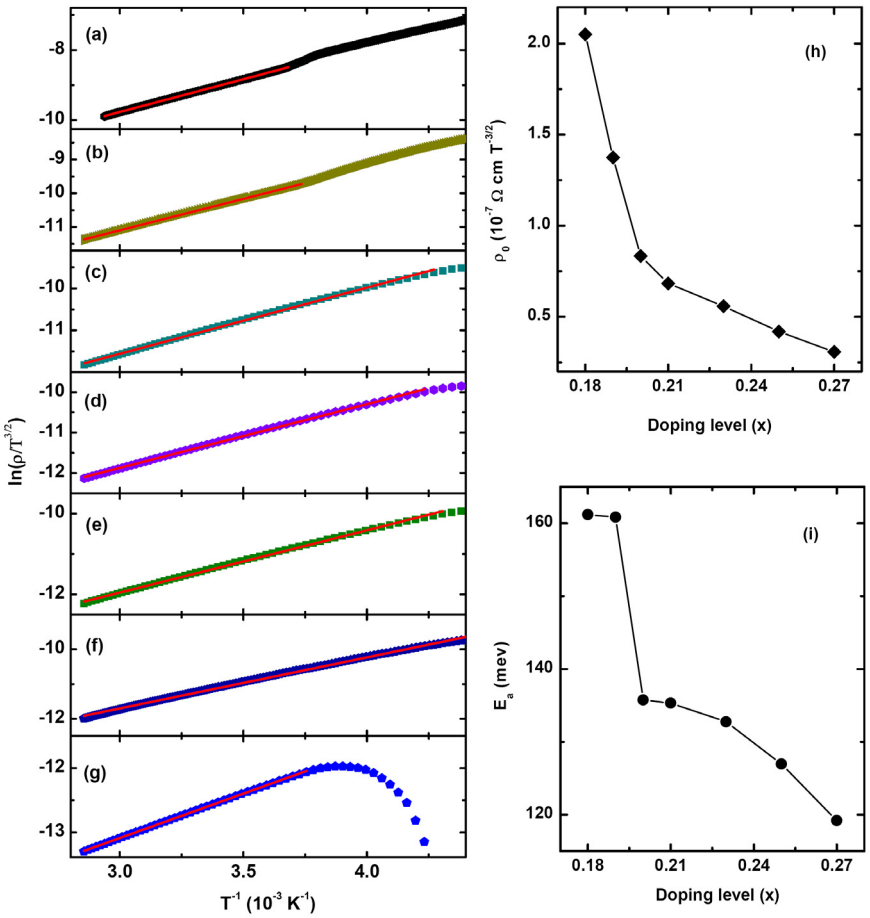

Figure 4.7 *Estimates of the excitation energy using small polaron hopping model. Zero field resistivity reproduced in the linearized form of equation (4-5), namely $\ln(\rho/T^{3/2})$ vs. T^{-1}, Figures (a) – (g) correspond to x = 0. 18; x = 0.19; x = 0.20; x = 0.21; x = 0.23; x = 0.25 and x = 0.27, respectively. The linear fits yield the corresponding excitation energy E_a and also the prefactor ρ_0, both of which are plotted as a function of doping level x in (h) and (i).*

Subsequently, the correlation of the general transport behavior with the magnetic response (in particular, magnetization and ac susceptibility) is investigated. The results of zero-field ac susceptibility measurements are summarized in Figure 4.8 – the real part (χ) in Figures 4.8 (a)-1 to (g)-1, and the imaginary component ($\chi^{"}$) in Figures 4.8 (a)-2 to (g)-2. These data, from all samples, enable two initial estimates to be made. First, the maximum susceptibility, often referred as the Hopkinson/principal maximum [46-48], provides an experimental estimate for the demagnetization factor, $N_{D,}$ (values unexpectedly close to theoretical estimates given the non-ellipsoidal sample shape) and used subsequently to make demagnetization corrections. Second, the inflection point in ac susceptibilities (first derivative, $d\chi/dT$, is a minimum) yields a preliminary estimates for ordering temperatures (T_C). The imaginary component peaks close to T_C and the Hopkinson/principal maximum, confirming the onset of irreversible magnetization processes in the ordered phase.

Despite the closeness in composition of these samples, the ac susceptibilities exhibit marked differences, the most relevant of which – in terms of current study – can be seen in Figure 4.9, in which the inverse ac susceptibilities ($1/\chi$) (measured in both zero-field and in various static biasing fields up to 1 kOe) are plotted as a function of temperature. The characteristic depression evident for some of these data below the higher temperature CW line is symptomatic of a so-called Griffiths-like phase, as mentioned in the second Chapter [57-60], namely, an inverse susceptibility of the form $\chi^{-1} \propto (T - T_C^{Rand})^{1-\lambda}$.

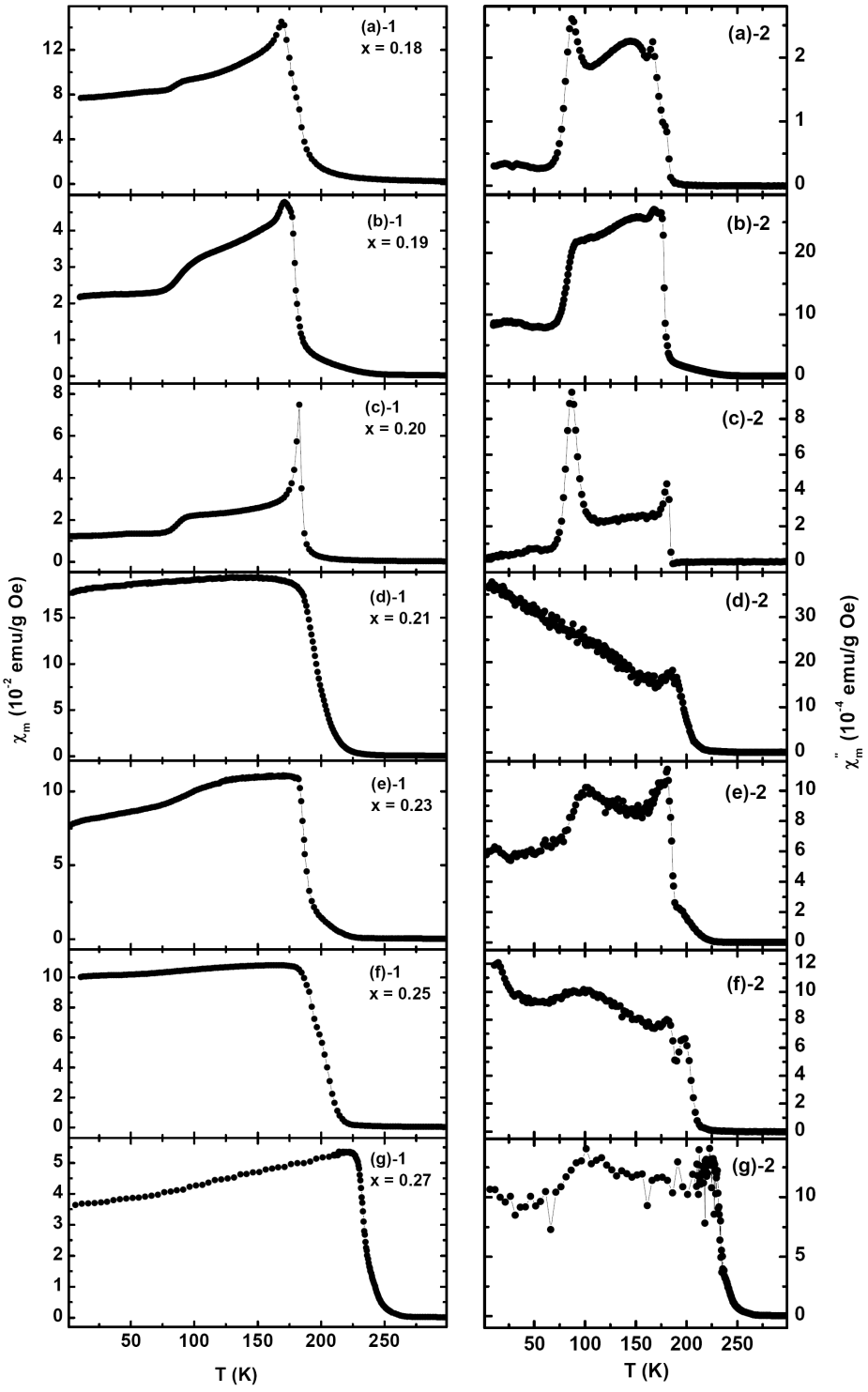

Figure 4.8 *Zero field ac susceptibilities of $La_{1-x}Ca_xMnO_3$ ($0.18 \leq x \leq 0.27$). Figures (a)-1 to (g)-1 are in-phase components to x = 0. 18, x = 0.19, x = 0.20, x = 0.21, x = 0.23, x = 0.25 and x = 0.27 respectively, measured on warming following ZFC. Figures (a)-2 to (g)-2 are the corresponding imaginary components of the ac susceptibility.*

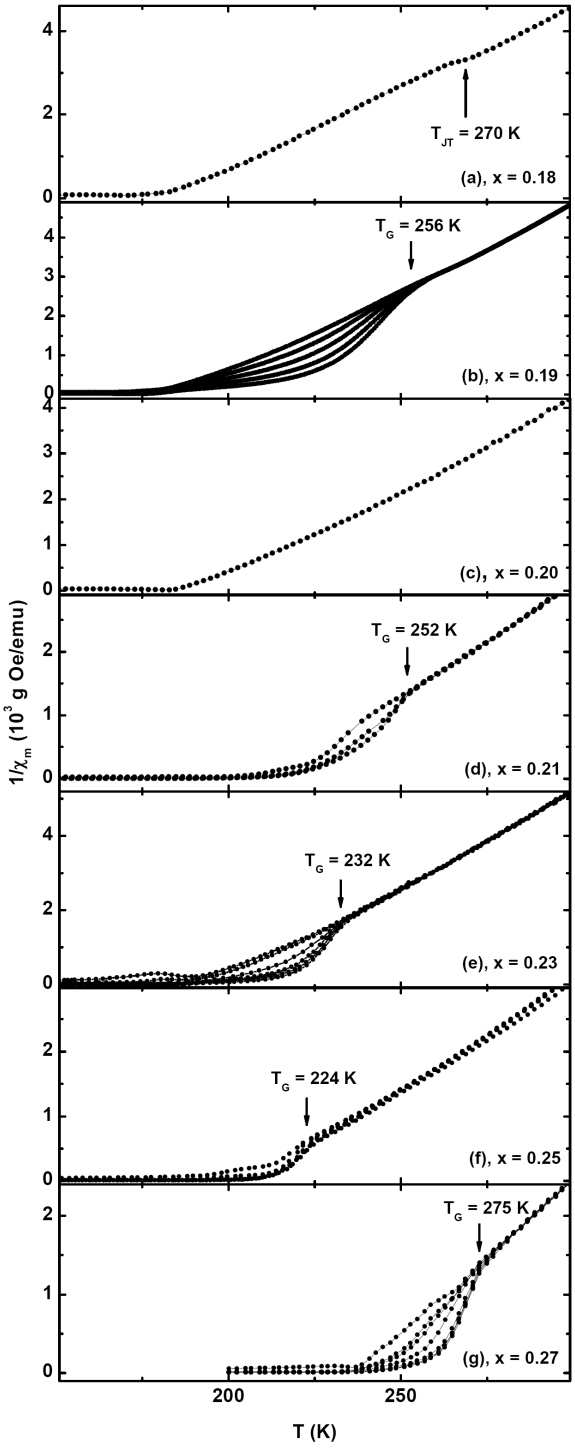

Figure 4.9 *Occurrence of Griffiths-like phases in $La_{1-x}Ca_xMnO_3$ ($0.18 \leq x \leq 0.27$). The inverse ac susceptibilities measured under various static fields, with zero always at the bottom, figures (a) – (g) correspond to x = 0.18 (0), x = 0.19 (0, 50, 100, 200, 500 Oe), x = 0.20 (0), x = 0.21 (0, 100, 200, 500 Oe), x = 0.23 (0, 30, 70, 200, 500, 1000 Oe), x = 0.25 (0, 50, 100, 500, 1000 Oe), x = 0.27 (0, 20, 50, 100, 200, 350, 500, 1000 Oe).*

Again, here T_C^{Rand} is the random transition temperature and λ is the exponent quantifying the Griffiths-like phase. Currently, a precise definition for T_C^{Rand} has not been provided. Rather it remains a parameter to be obtained from fitting, using the constraint that in the higher temperature regime above T_G, the "exponent" $\lambda \sim 0$, an anticipated result as the Griffiths-like phase evolves into a conventionally disordered PM state. Following Magen et.al., [58], a working definition for T_G has been taken as the temperature of the onset of a depression below high-temperature CW behavior. These T_G estimates are marked by vertical arrows in Figure 4.9. Further, the rapid suppression of the Griffiths-like phase with field evident in Figure 4.9 is also expected, as the applied field is the conjugate field for uniform ferromagnetism rather than its disordered Griffiths counterpart. While the fitting approach outlined above is physically reasonable, it does result in a degree of uncertainty in T_C^{Rand} and hence λ, and will be returned to in discussions of the $(La_{1-y}Pr_y)_{0.7}Ca_{0.3}Mn^{16/18}O_3$ ($y \leq 0.85$) [60] system later in this chapter.

The occurrences of a Griffiths-like phase have been reported in range of doped perovskites based on a various physical measurements [18-20, 54, 55, 59-61, 98-100], their presence has been attributed to the influence of disorder on the phase complexity in the manganites and related systems, such as magnetocaloric compound [58, 101]. Whereas Griffiths-like phase have been shown to correlate closely with CMR in $La_{1-x}Ca_xMnO_3$ near optimal doping ($x \approx 0.33$) [18, 20], a comparison of the data in Figures 4.6 and 4.9 enable the following conclusions to be drawn (**i**) that a Griffiths-like

phase is clearly *not* a prerequisite for CMR – the x = 0.20 and 0.21 samples both exhibit CMR, whereas only the latter displays a Griffiths-like phase [19], and (**ii**) allows the further important new caveat that indeed the appearance of a Griffiths-like phase does not *guarantee* the emergence of CMR – the x = 0.19 specimen exhibits a Griffiths-like phase but has an insulating ground state and hence no appreciable MR [55]. These conclusions raise ongoing questions regarding our current understanding of the fundamental mechanism(s) underlying CMR [3, 4, 18-20].

While the current data allow these two specific conclusions to be drawn, they also raise further questions about the "disorder" [98, 100] relevant for establishing Griffiths-like phase characteristics in $La_{1-x}Ca_xMnO_3$. Unlike the linking of such characteristics with phase competition discussed later in this chapter for optimally doped $(La_{1-y}Pr_y)_{0.7}Ca_{0.3}Mn^{16/18}O_3$ ($y \leq 0.85$) [60], no such definitive results exist currently for $La_{1-x}Ca_xMnO_3$. In particular, Rodriguez-Martinez and Attfield [102] have proposed a semiquantitative model which provides a considerable degree of unification in discussing the behavior of doped Mn perovskites (with a more recent extension covering cuprate superconductors [103]) in the form of a comprehensive $T_C(<r_A>,0)$ versus $<r_A>$ phase diagram. This encompasses the use of a disorder-corrected ordering temperature $T_C(<r_A>,0)$ estimates using:

$$T_C(< r_A >, 0) = T_C(r_A°, 0) - \varpi(r_A° - < r_A >)^2 \qquad 4\text{-}6$$

In this expression, $r_A°$ represents the ideal radius of the undistorted cubic perovskite structure (taken as 1.30 Å near optimal doping), so that the last term in equation (4-6)

measures the departure of the actual structure from "ideal", i.e., a measure of the strain field. $T_C(r_A°, 0)$ and ϖ were proposed as universal constants for these optimally doped perovskites, assuming values of 530 K and 29×10^3 KÅ^{-2} respectively from fitting available data. As can be seen from Table 4.1, there is no clear correlation between the occurrence of Griffiths-like phase behavior and the tabulated *structural* parameters (or indeed the combinations such as $<r_A>/\varphi)$), viz., the parameters that are central to the Rodriguez-Martinez and Attfield approach. This lack of correlation indicates that the disorder underlying the tendency to nucleate a Griffiths-like phase is *not* simply structural in origin, and hence needs further study. Such data emphasize the continued subtleties displayed by CMR manganites.

It should be conceded here, however, that it does not seem unlikely that oxygen stoichiometry may play some role in this issue through changes necessary to maintain charge neutrality, as summarized by [104, 105]:

$$La^{3+}_{1-x}Ca^{2+}_{x}Mn^{3+}_{1-x+2\Delta}Mn^{4+}_{x-2\Delta}O^{2-}_{3-\Delta} \qquad 4\text{-}7$$

One consequence of oxygen deficiency (represented by Δ) would be changes in the ratio of DE linked Mn^{3+}-Mn^{4+} sites and the numbers of Mn^{3+}-Mn^{3+} and Mn^{4+}-Mn^{4+} SE interactions [105], influencing principally the distribution/disorder of exchange couplings. Unfortunately, no means of measuring the oxygen stoichiometry with sufficient precision to comment with the necessary degree of certainty on this issue in the present series of samples is currently available to us.

4.2.2 Evolution of Magnetic Critical Behavior

4.2.2 (A) x = 0.18 and 0.20

Magnetization. As these two single crystals display no Griffiths-like phase features, their behavior is the simplest to analyze. Arrott plots ($M^2 \sim H_i/M$) for the corresponding data display a positive slope (i.e., no term of the form $- a(T)M^4$ in the free energy [35, 37, 38]) throughout the transition region, confirming the continuous/second-order nature of the FM-PM transition.

Based on the modified Arrott-Noakes equation of state [43], these data were subsequently plotted using a range of model exponents, which iterate towards values consistent with Heisenberg model predictions [51] ($\gamma = 1.387$, $\beta = 0.365$, and $\delta = 4.783$), namely, $(H_i/M)^{1/1.387}$ versus $M^{1/0.365}$, as shown in Figures 4.10 (a) for x =0.18 and 4.10 (b) for x = 0.20. Self-consistency is ensured by taking the intercepts from these latter two figures (that on the vertical axis giving the spontaneous magnetization, M_S and horizontal axis, the inverse initial susceptibility, $1/\chi_i$) and testing them against the corresponding power-law predictions, equations (2-20) and (2-22), as shown in Figures 4.10 (c) and (d), and Figures 4.10 (e) and (f), the slopes of the inserts in these figures yield the marginally refined exponent estimates. This process is then iterated until minimal changes in exponent values result [46, 47, 106]. The critical isotherms yield values for T_C, with the associated magnetizations (Figures 4.10 (g) and (h)) being tested

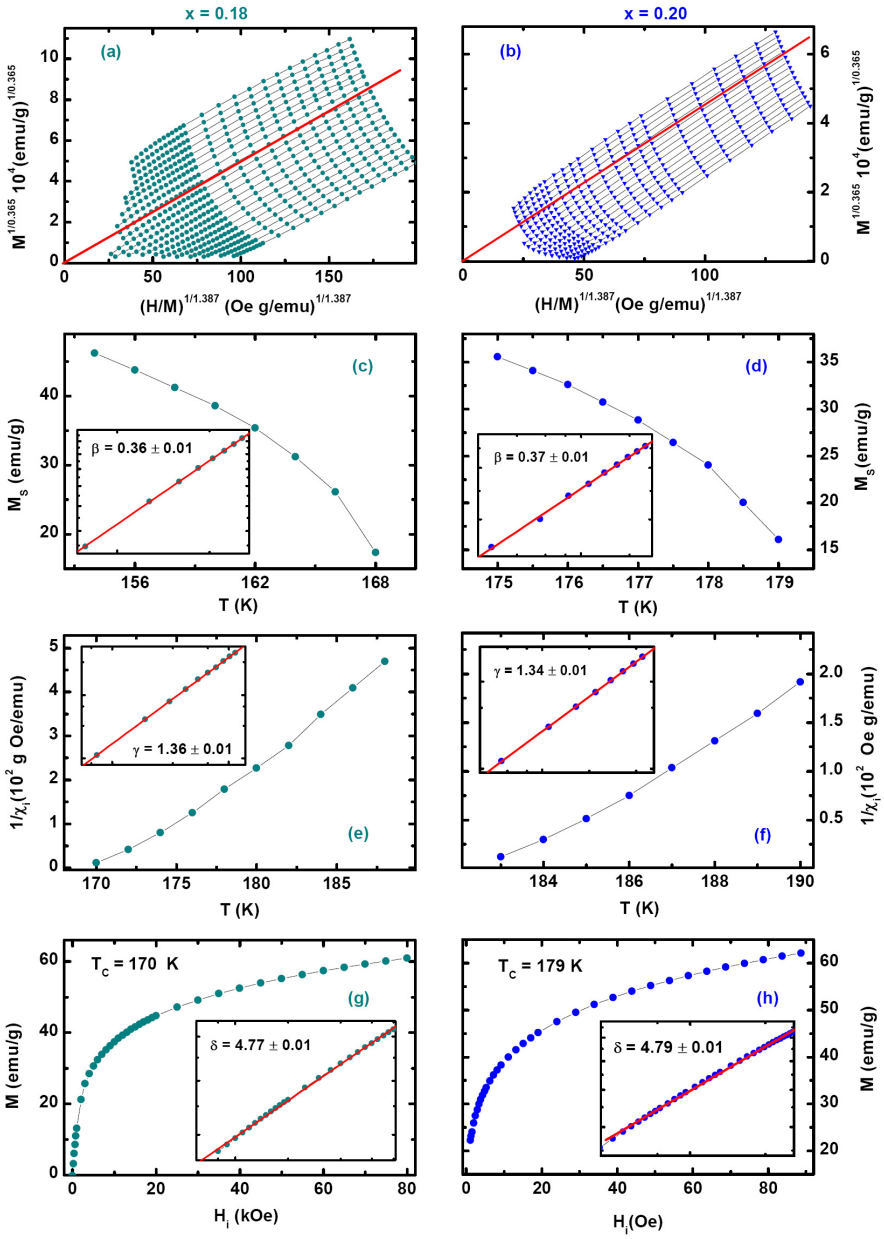

Figure 4.10 *Magnetic critical analysis for x = 0.18 and x = 0.20. Figures (a) and (b) reproduce selected magnetic isotherms (from 150 K to 190 K in 2 K steps for x = 0.18, from 175 K to 190 K in 1 K steps for x = 0.20) in the form* $(H_i/M)^{1/1.387}$ *vs.* $M^{1/0.365}$*. (c) and (d)* $M_S(T)$ *plotted against T: inset;* M_S *vs.* t_m *on a log-log scale, yielding* $\beta = 0.36 \pm 0.01$ *in x = 0.18, and* $\beta = 0.37 \pm 0.01$ *in x = 0.20. (e) and (f) The inverse initial susceptibility,* $1/\chi_i$*, plotted against T: inset;* $1/\chi_i$ *vs.* t_m *on a log-log scale, yielding* $\gamma = 1.36 \pm 0.01$ *in x =0.18, and* $\gamma = 1.34 \pm 0.01$ *in x =0.20. The critical isotherms passing through the origins yield* T_C*. (g) and (h) Plots of M vs.* H_i *at* T_C*, the insets are the corresponding double-logarithmic plots, the slopes of the straight lines drawn yielding* $\delta = 4.77 \pm 0.01$ *for 4 kOe < H < 90 kOe in x = 0.18, and* $\delta = 4.79 \pm 0.01$ *for 4 kOe < H < 90 kOe in x = 0.20.*

against the prediction of equation (2-21), as shown in the inserts in these latter figures.

This procedure yields values of $T_C = 170 \pm 1$ K, $\gamma = 1.36 \pm 0.01$, $\beta = 0.36 \pm 0.01$ and $\delta = 4.77 \pm 0.01$ (3 kOe < H < 90 kOe) for x = 0.18, with $T_C = 179 \pm 1$ K, $\gamma = 1.34 \pm 0.01$, $\beta = 0.37 \pm 0.01$ and $\delta = 4.79 \pm 0.01$ (4 kOe < H < 90 kOe) for x = 0.20. Both sets of estimates agree with Heisenberg model predictions within experimental uncertainty, and satisfy the Widom equality $\gamma = \beta(\delta-1)$ [35]). The δ estimate, incidentally, confirms – albeit directly – the absence of Griffiths-like phase behavior, as the latter is frequently characterized by large δ values [18, 19], an issue addressed in more detail below.

Ac Susceptibility. The evolution of the ac susceptibility peak structure with field and temperature, typified by the data in Figures 4.11 (a) for the x = 0.18 and (b) for the x = 0.20 single crystals, provides confirmatory evidence of the continuous nature of the accompanying phase transition, and provides independent estimates of both the critical exponents and ordering temperatures. Figures 4.11 (c) – 4.11 (i) summarize the analysis of such ac susceptibility peak data for both x = 0.18 and 0.20, in terms of power-law predictions, equations (2-25) – (2-27). Figures 4.11 (b) and (c) reproduce plots of the critical peak amplitudes χ_m (corrected for background and demagnetizing effects) – taken from Figure 4.11 (a) for x = 0.18 (and its equivalent for x = 0.20) – against the internal field H_i on a double-logarithmic scale; these not only confirming the power law dependence of equation (2-25), but their slopes also yield estimates of $\delta = 4.78 \pm 0.01$ (x = 0.18) and 4.78 ± 0.01 (x = 0.20). These estimates are clearly independent of any choice for T_C, indicating that ac susceptibility measurements provide a distinct

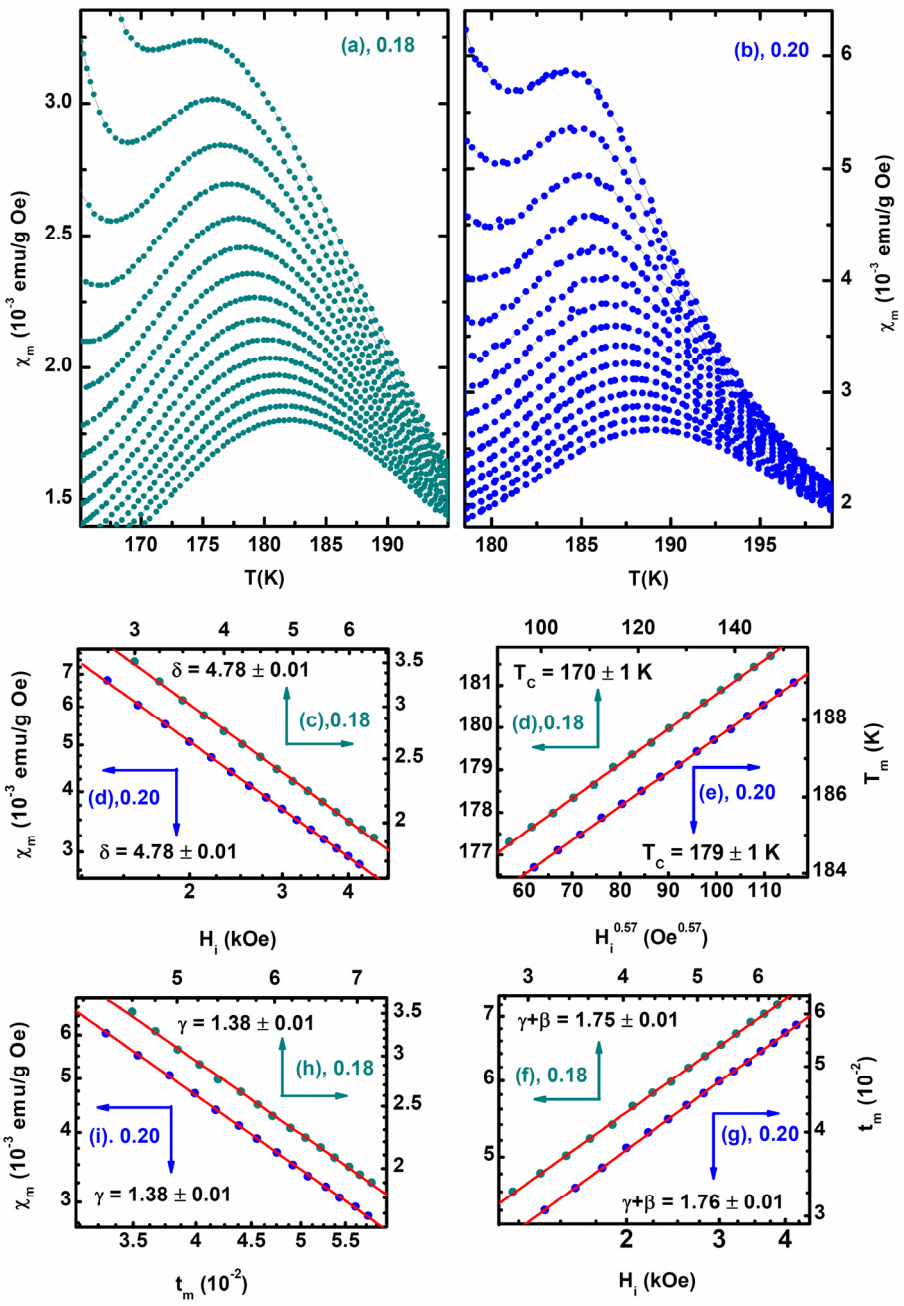

Figure 4.11 *Susceptibility critical analysis for x = 0.18 and x = 0.20. χ(H, T) (corrected for background and demagnetization effects) measured on warming following ZFC in various static fields, (a) x = 0.18 from 3 kOe (top) to 6.5 kOe (bottom) in 250 Oe steps, (b) x = 0.20 from 1.4 kOe (top) to 4.2 kOe (bottom) in 200 Oe steps. (c) Plot of log (χ_m) vs. log (H_i), yielding the exponent δ. (d) Plot of T_m against $H_i^{0.57}$ yielding an estimate for T_C. (e) Plot of log (χ_m) vs. log (t_m), yielding the exponent γ. (f) Plot of log (t_m) vs. log (H_i), yielding the exponent sum γ + β, and hence β. Susceptibility scaling plots for (g) x = 0.18 and (f) x = 0.20 using the data in (a) and (b).*

advantage over conventional magnetization-based approaches, for which the determination of the ordering temperature (T_C) is a prerequisite prior to extracting estimates for δ from data taken by attempting to stabilize along the critical isotherm.

The remaining exponent values, however, require a choice for T_C to be made; this is done – based on equation (2-26) – by plotting the measured peak temperatures, T_m, against the internal field $H_i^{0.57}$ (i.e., assuming the applicability of Heisenberg model exponents, namely, $(\gamma+\beta)^{-1} = 0.57$ [35, 46-48], as suggested by the δ estimate, above), and extrapolating to $H_i = 0$, as shown in Figures 4.11 (d) and (e). This yields $T_C = 170 \pm 1$ K for $x = 0.18$ and $T_C = 179 \pm 1$ K for $x = 0.20$ respectively. These initial T_C estimates are then used to construct the double-logarithmic plots of the reduced temperatures t_m against the internal fields H_i (equation (2-26)) shown in Figures 4.11 (f) and 4.11 (g), and of the peak amplitude χ_m against the reduced temperature, t_m (equation (2-27)), Figures 4.11 (h) and 5 (i). The slopes of such plots yield initial estimates for $(\gamma+\beta)^{-1}$ and γ^{-1}, respectively. Subsequently, this process is iterated, accompanied by s*mall* adjustments in T_C, until self-consistency is achieved. Thus values of $\beta = 0.37 \pm 0.03$, $\gamma = 1.38 \pm 0.01$, and $T_C = 170 \pm 1$ K ($x = 0.18$) and $\beta = 0.37 \pm 0.03$, $\gamma = 1.38 \pm 0.01$, and $T_C = 179 \pm 1$ K ($x = 0.20$) were obtained, both parameter estimates being in excellent agreement with the analysis of the magnetization data.

A final test of ordering temperatures (T_C) and these exponent value estimates for – and hence the applicability of 3-D Heisenberg model exponents – to these samples is provided in Figure 4.12, using the magnetic isotherms reproduced in Figures 4.10 (a)

and (b), and ac susceptibility data shown in Figures 11 (a) and (b), for x = 0.18 and x = 0.20, respectively. The magnetization scaling using the above listed T_C's and exponent estimates, based on equation (2-19) [35, 43, 107], is carried out in Figure 4.12 (a); both demonstrates good data collapse. Susceptibility scaling is based on equation (2-28); specifically, such data, when normalized to its peak value ($\chi(h,T_m)$), should collapse onto a universal curve when plotted against the argument ($h/t_m^{(\gamma+\beta)}$) of the scaling function (actually, its inverse, $t_m/h^{1/(\gamma+\beta)}$, to preserve the peak structure [46, 47]), as confirmed in Figures 4.11 (a) and (b). In summary, the above analysis provides consistent estimates for the ordering temperatures T_C, and demonstrates convincingly that the exponent estimate agree, within experimental uncertainty, with those of the 3-D Heisenberg model and thus satisfying the Widom equality.

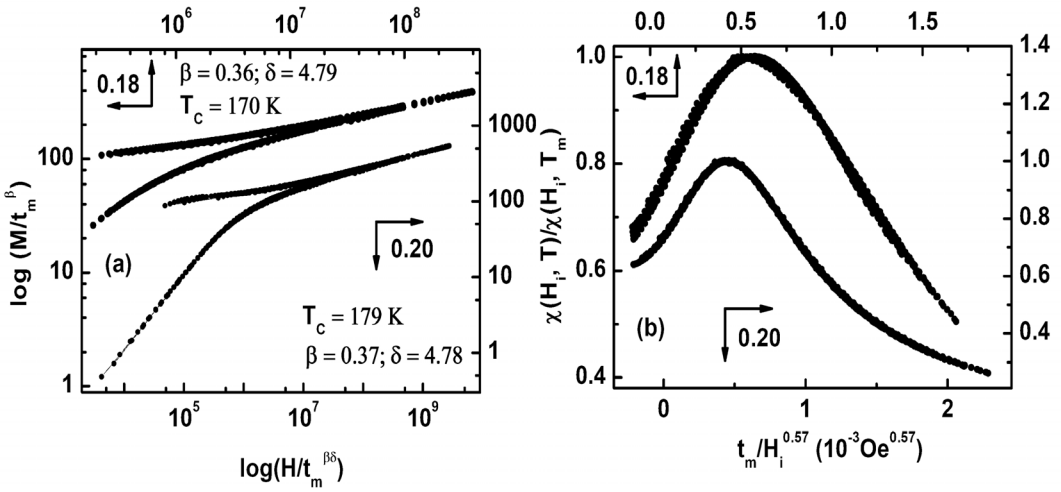

Figure 4.12 *Conventional magnetization and susceptibility scaling analyses. (a) Double logarithmic magnetization scaling plots of data from Figure 4.10 (a) and (b) using the critical exponents and T_C listed above. The upper branch corresponds to data below T_C and the lower branch to data above T_C. (b) Susceptibility scaling plots for the data in Figure 4.11 (a) and (b).*

4.2.2 (B) x = 0.19

As can be seen from Figure 4.9 (b), this single crystal displays features characteristic of Griffiths-like phase, what is also evident from this figure is that such features are rapidly suppressed by an applied field. Such a result is expected since a uniform applied field is the conjugate field for collinear ferromagnetism, enhancing the latter at the expense of its non-uniform Griffiths counterpart [59]; what is not understood at present are the parameters that determine the *rate* at which such a suppression occurs with applied field [59]. At x = 0.19 this suppression is rapid, as the following demonstrates.

Arrott plots again confirm the continuous nature of the PM-FM transition. Following the procedure outlined earlier, these data could be linearized initially using the same exponent values as those deduced above, namely, $(H_i/M)^{1/1.387}$ versus $M^{1/0.365}$, Figure 4.13 (a). Subsequent analysis, summarized in Figure 4.13 (b) – (d), yields T_C = 173 ± 1 K, $\delta = 4.78 \pm 0.01$ (3 kOe < H < 90 kOe), $\gamma = 1.36 \pm 0.01$, and $\beta = 0.37 \pm 0.01$. As mentioned earlier, Griffiths-like phase features are often accompanied by large δ values [18, 19]; such behavior is not, however, observed in x = 0.19 sample, first because the Griffiths-like phase features are rapidly suppressed by field and second, because *low*-field data (those typically below 0.5 – 1 kOe, where such features *are* present) are seldom included in scaling analysis to avoid both technical contribution and the relatively large uncertainties associated with demagnetization corrections prevalent

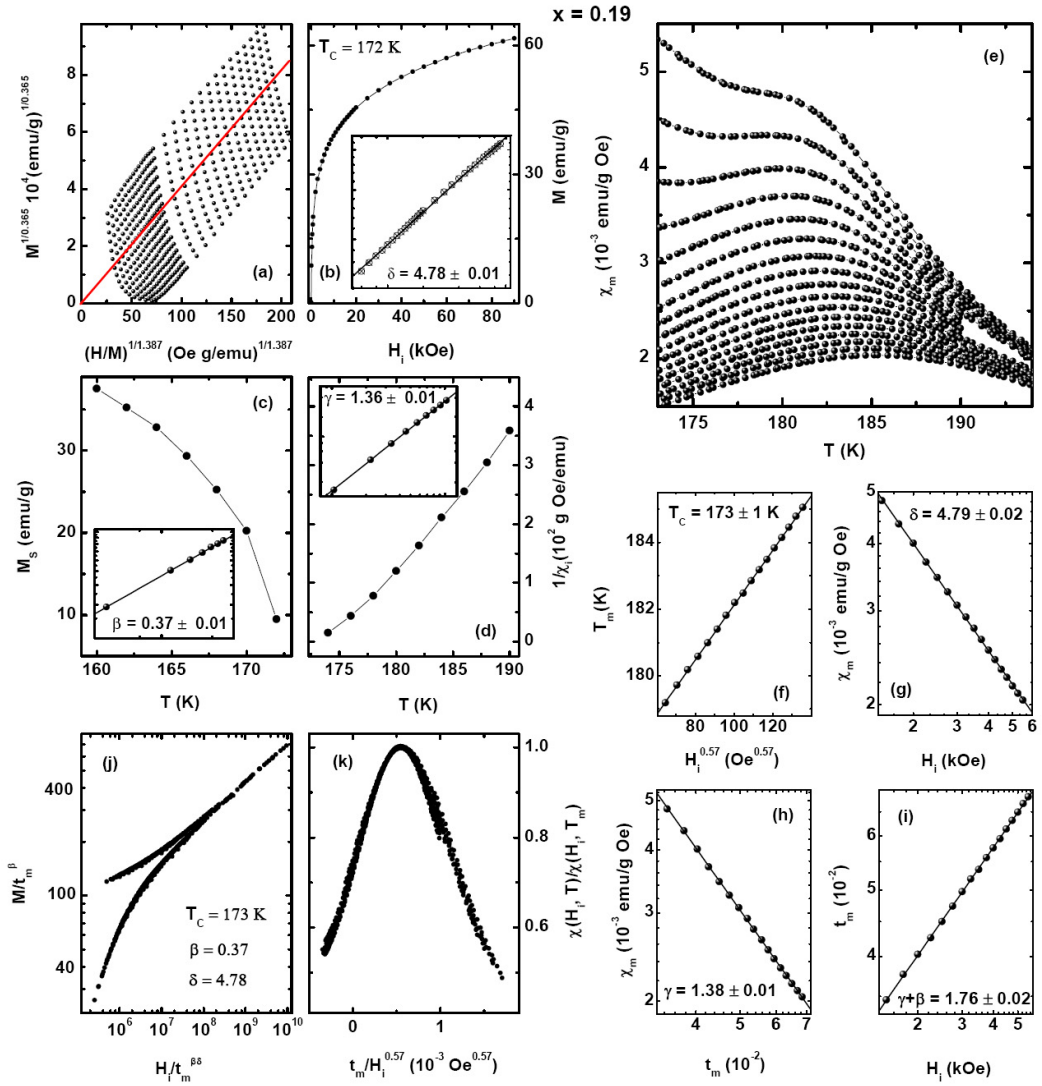

Figure 4.13 *Magnetic critical analysis for x = 0.19. Figure (a) reproduces selected magnetic isotherms (from 160 K to 190 K in 2 K steps), in the form* $(H_i/M)^{1/1.387}$ *vs.* $M^{1/0.365}$*. The isotherm passing through the origin yields* T_C*. (b) Plot of M vs.* H_i *along critical isotherm* T_C *= 172 K, the log (M) vs. log (*H_i*) plot in the inset yields* $\delta = 4.78 \pm 0.01$ *for 4 kOe < H < 90 kOe. (c)* $1/\chi_i$*, plotted against T: the log (*$1/\chi_i$*) vs. log (t) plot in the inset yields* $\gamma = 1.36 \pm 0.01$*. (d)* $M_S(T)$ *plotted against T: the log (*M_S*) vs. log (t) plot in the inset yields* $\beta = 0.37 \pm 0.01$*. (e)* $\chi(H,T)$ *(corrected for background and demagnetizing effects) measured on warming following ZFC in fixed static fields of 1.5 kOe (top) to 5.5 kOe (bottom) in 250 Oe steps. (f) Estimate of critical temperature,* T_C *= 172 ± 1 K, from extrapolation of* T_m *against* $(H_i^{0.57})$*. (g) The slope of log (*χ_m*) vs. log (*H_i*) plot yields* $\delta = 4.79 \pm 0.02$*. (h) The slope of log (*t_m*) vs. log (*H_i*) plot yields* $\gamma + \beta = 1.76 \pm 0.02$*; (i) the slope of log (*χ_m*) vs. log (*t_m*) plot yields* $\gamma = 1.38 \pm 0.01$*, and hence* $\beta = 0.37 \pm 0.02$*. (j) Conventional magnetic scaling plot of data in (a). (k) Susceptibility scaling plot for the isokaps in (e).*

in that field range. A similar situation occurs in the analysis of ac susceptibility data on this single crystal, summarized in Figures 4.13 (e) to (i). Here a critical peak structure similar to that shown in Figure 4.13 (e) emerges, but as fields in excess of 1.5 kOe have to be applied to first resolve this structure, such fields completely suppress Griffiths-like phase characteristics in *this* sample. The analysis of these ac susceptibility data in manner outlined earlier yields $\delta = 4.79 \pm 0.01$, $\beta = 0.37 \pm 0.01$, and $\gamma = 1.38 \pm 0.01$, with $T_C = 172 \pm 1$ K, in close agreement with the analysis of magnetization data and, again, with model predictions for the 3-D Heisenberg model. The magnetization and ac susceptibility data collapses can be seen to be accompanied using with the parameters listed above in Figures 4.13 (j) and (k).

This x = 0.19 Ca substituted single crystal thus displays properties very similar to single crystal $La_{0.73}Ba_{0.27}MnO_3$ [59]; both show signatures of Griffiths-like phase behavior but with an *insulating* ground state, and δ values close to those of the Heisenberg model due to the rapid field-induced suppression of Griffiths-like phase features. This point is discussed in more detail below. Given the near Heisenberg model behavior of the three single crystals with x = 0.18, 0.19 and 0.20, their critical amplitudes, E in equation (2-16), were estimated from power-law plots, and listed in Table 4.1. Since this table contains a comprehensive survey of parameters obtained by fitting magnetization, susceptibility and transport data, further discussion of its content is deferred at this point.

4.2.2 (C) x = 0.21, 0.23 and 0.25

As might be anticipated, the presence of Griffiths-like phase characteristics complicates the analysis of the magnetic critical behavior in these three single crystals in varying degrees, for example, Figure 4.14 for x = 0.21. While Arrott plots (Figure 4-14 (a)) exhibit positive slopes throughout the transition region, confirming the occurrence of a continuous PM-FM transition, modified Arrott-Noakes plots using a range of model parameters fail to linearize the magnetization-field data at these compositions. Figure 4.14 (b) illustrates this point for the x = 0.21 single crystal using Heisenberg exponent values. Such a result is often linked with the presence of Griffiths-like phase behavior [19]. As a consequence critical analysis, based on the temperature/field dependent magnetization of the type performed above for $0.18 \leq x \leq 0.20$, is precluded at these higher substitution levels.

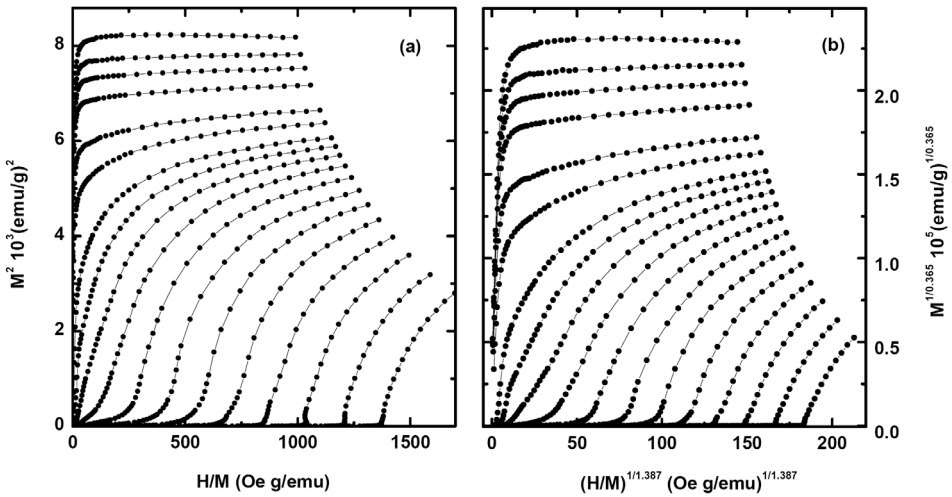

Figure 4.14 *Arrott and Modified Arrott plots for x = 0.21. (a) H_i/M vs. M^2 for selected magnetic isotherms measured at 2 K, from 100 K to 175 K in 25 K steps, at 185 K, and form 195 K to 250 K in 5 K steps. (b) Plot of $(H_i/M)^{1/1.387}$ vs. $M^{1/0.365}$ for data in (a).*

The field-dependent ac susceptibility, in contrast, does not suffer from this limitation; in all three of these samples a peak structure similar to that shown in Figure 4.11 (a) for x = 0.18 and (b) for x = 0.20, emerges and can be analyzed in the manner described above. The emergence of this peak structure, incidentally, supports the conclusion that the magnetic transition is second order/continuous. Figure 4.15 provide estimates for exponents δ directly, prior to the identification of T_C, as described above, these estimates are: $\delta = 19 \pm 1$ (x = 0.21), $\delta = 5 \pm 0.3$ (x = 0.23), and $\delta = 15 \pm 1$ (x = 0.25). Such estimates far exceed that for the 3-D Heisenberg model, at least for x = 0.21 and x = 0.25, a result typically accompanying Griffiths-like phase characteristics in some doped CMR perovskites [18, 19, 54, 55], at x = 0.23 the δ estimates marginally exceed the model values – as in $La_{0.7}Ba_{0.3}MnO_3$ [54] which also exhibits a Griffiths-like phase – an issue addressed in more detail later in this chapter.

Furthermore, since estimates for the critical amplitude E (equation (2-21)) depend crucially on the value for δ [15, 106], no such estimates are listed for these three single crystals. To extract other exponent estimates, a value for T_C must be established *quantitatively*. Despite the non-standard values for δ, plots of T_m against the internal field $H_i^{1/(\gamma+\beta)}$ using Heisenberg model exponents provides an excellent representation of the data between x = 0.21 and x = 0.25 [54]. This is a fortuitous result, but one enabling a quantitative estimate for T_C to be made, as confirmed in Figures 4.15 (a)-2, (b)-2 and (c)-2. Nevertheless, while the *sum* of these two exponents combine to the Heisenberg model value, the remaining two scaling plots – Figures 4.15 (a)-3/(a)-4, (b)-3/(b)-4, and

(c)-3/(c)-4 indicate that *individual* exponent values differ from model predictions. The results emerging from these latter two sets of figures yield: $\delta = 19 \pm 1$, $\beta = 0.09 \pm 0.02$, $\gamma = 1.65 \pm 0.01$, with $T_C = 182 \pm 1$ K for $x = 0.21$ (in excellent agreement with the initial report [19]), $\delta = 5.0 \pm 0.3$, $\beta = 0.43 \pm 0.02$, $\gamma = 1.35 \pm 0.01$, with $T_C = 185 \pm 1$ K for $x = 0.23$, and $\delta = 15 \pm 1$, $\beta = 0.51 \pm 0.02$, $\gamma = 1.15 \pm 0.04$, with $T_C = 188 \pm 1$ K for $x = 0.25$. The field ranges covered in, for example, the various δ plots are determined by the field range over which the critical peak structure is well resolved. This, in turn, is controlled by the ease, or difficulty, with which the regular/technical contributions to the measured response are suppressed. In dilute alloy systems such as **Pd**Mn and **Pd**Fe this is controlled by the coercive field, H_C, which in the latter enable critical peak structure – and hence critical analysis – to be carried out in fields as low as 4 and 0.1 gauss respectively (such measurements are truly asymptotic in nature). In the first alloy system mentioned, the Mn ion is in an S-state, whereas in contrast, Mn^{3+} ions in the systems studied here are not – they are Jahn-Teller ions subject therefore to spin-orbit coupling and these systems are thus technically harder. While this observation provides a qualitative explanation of the higher fields needed to first resolve critical peak structure in these doped perovskites, quantitative differences between the two types of systems being discussed exist. Specifically the coercive fields measured in these manganites, typically 5 – 50 Oe [46], do not provide an appropriate measure of the technical hardness in the context of the present discussion; fields far in excess of H_C need to be applied before well resolved susceptibility peaks emerge. This difference is

the subject of ongoing investigation; it exhibits a distinct variation with sample doping level, and thus underlies the differing field ranges over which critical behaviour can be assessed, as in the figure below.

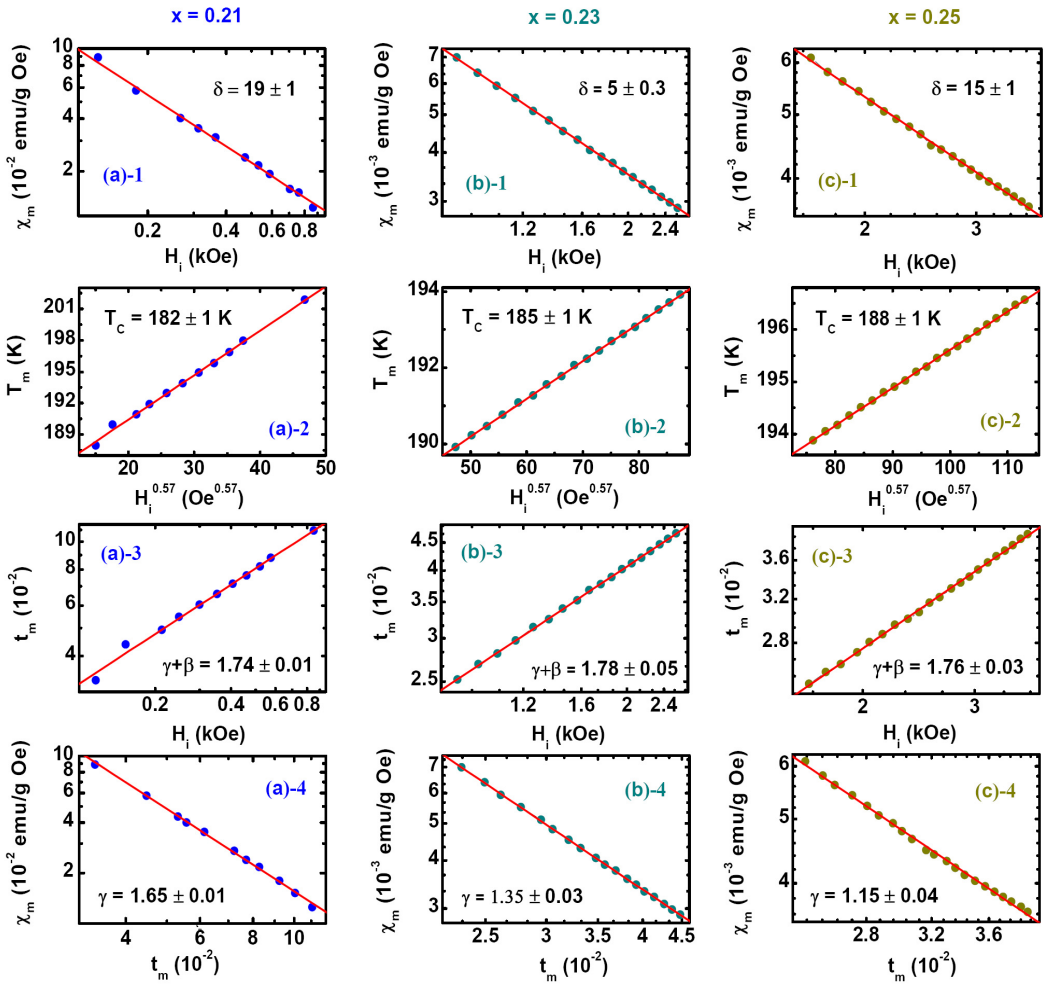

Figure 4.15 *Susceptibility critical analyses for x = 0.21, x = 0.23, and x = 0.25. (a) The slope of log (χ_m) vs. log (H_i) plot yields δ. (b) Estimate of critical temperatures, from extrapolation of T_m against ($H_i^{0.57}$). (c) The slope of log (t_m) vs. log (H_i) plot yields $\gamma + \beta$. (i) The slope of log (χ_m) vs. log (t_m) plot yields γ, and hence β. These estimates are $\delta = 19 \pm 1$, $\beta = 0.09 \pm 0.02$, $\gamma = 1.65 \pm 0.01$, with $T_C = 182 \pm 1$ K for x = 0.2; $\delta = 5.0 \pm 0.3$, $\beta = 0.43 \pm 0.02$, $\gamma = 1.35 \pm 0.01$, with $T_C = 185 \pm 1$ K for x = 0.23, and $\delta = 15 \pm 1$, $\beta = 0.51 \pm 0.02$, $\gamma = 1.15 \pm 0.04$, with $T_C = 188 \pm 1$ K for x = 0.25.*

These non-standard estimates satisfy the Widom equality, within experimental uncertainty, for the x = 0.21 single crystal, but not its x = 0.23 and 0.25 counterparts; nevertheless, they also provide good data collapse for both the ac susceptibility *and* magnetization data for all of these samples, as Figure 4.16 confirms.

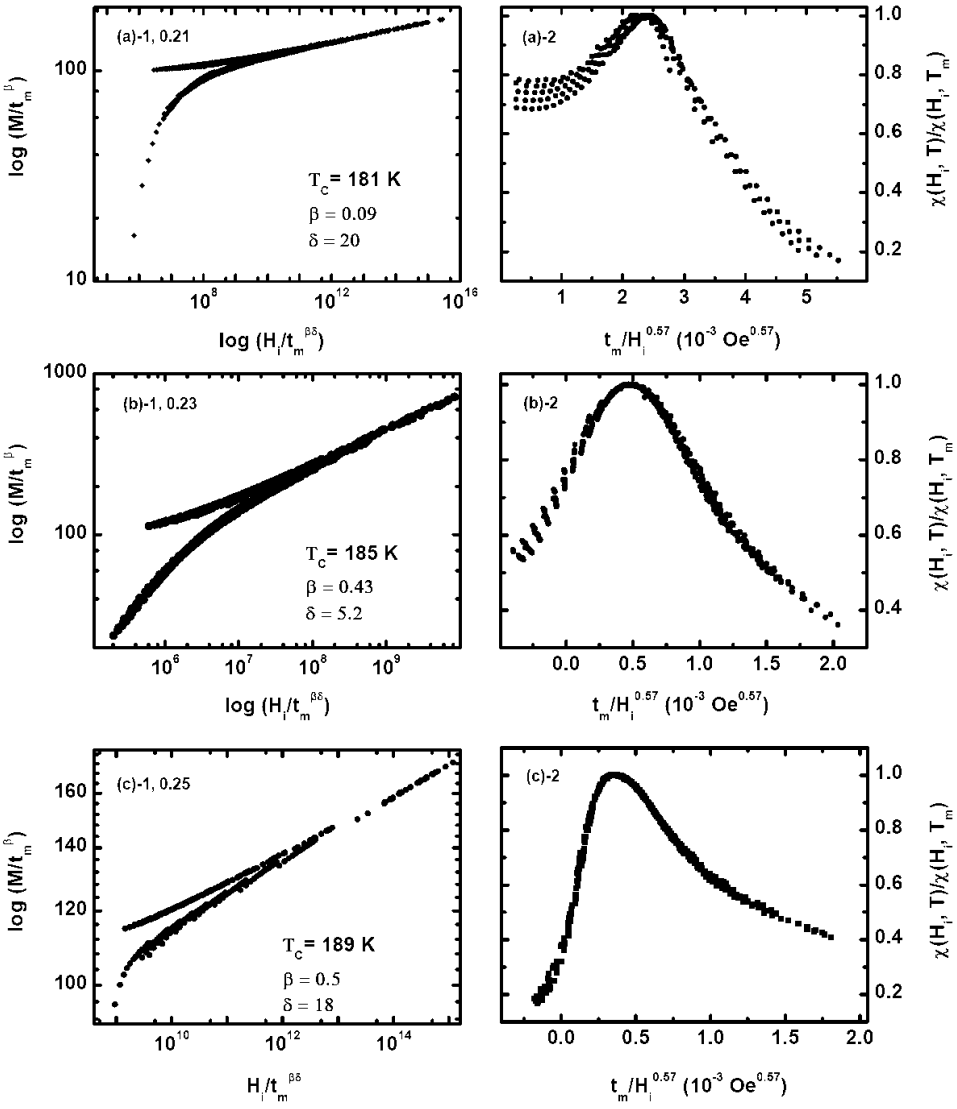

Figure 4.16 *Conventional magnetization and susceptibility scaling analyses. Figures (a)-1, (b)-1, and (c)-1 are magnetization scaling plots for x = 0.21, x= 0.23, and x = 0.25 on a double-logarithmic scale using the critical exponents and T_C listed above. The upper branch corresponds to data below T_C and the lower branch to data above T_C. Figures (a)-2, (b)-2, and (c)-2 the corresponding ac susceptibilities.*

4.2.2 (D) x = 0.27

As aspects of the unusual magnetic response at this composition have been reported previously [108], here we focus on issues related to the continued presence of Griffiths-like phase features at this composition. Briefly, therefore, Figure 4.17(a) summarizes magnetization data in fields up to 15 kOe in the vicinity of 240 K, which confirms both the metamagnetic/"S"-like character of the response near this temperature and the occurrence of weak hysteresis. Both features are consistent with the presence of a discontinuous/first-order PM-FM transition [38, 109], a conclusion is supported by Arrott plots for the corresponding data, Figure 4.17 (b), which can be seen to exhibit negative slopes over part of the (H-T) plane encompassing these data.

Nevertheless, field-dependent ac susceptibilities display a peak structure reminiscent of Figures 4.11(a) and (b), features normally associated with continuous/second-order transitions. As reported earlier [108], the usual tests of the evolution of these "pseudo-critical" peaks with field and temperature fail to confirm power-law behavior, they display continuous curvature, precluding estimates for critical exponents. Specifically, the Heisenberg model exponents do not describe these data is confirmed by the corresponding modified Arrott-Noakes plots, Figure 4.17(c).

It is important to (i) reiterate that the response summarized above is fundamentally different from cross-over effects accompanying a sequential second order to first order transition as the temperature is lowered towards T_C. In such a situation the

first order transition line would lie *below* that for the continuous transition, here it does not. A plot of the peak temperatures in the ac susceptibility against field combined with those for the metamagnetic field [38, 109] (the inflection points in Figure 4.17 (b) – a signature of the first-order transition line [38, 108, 109]) against temperature are

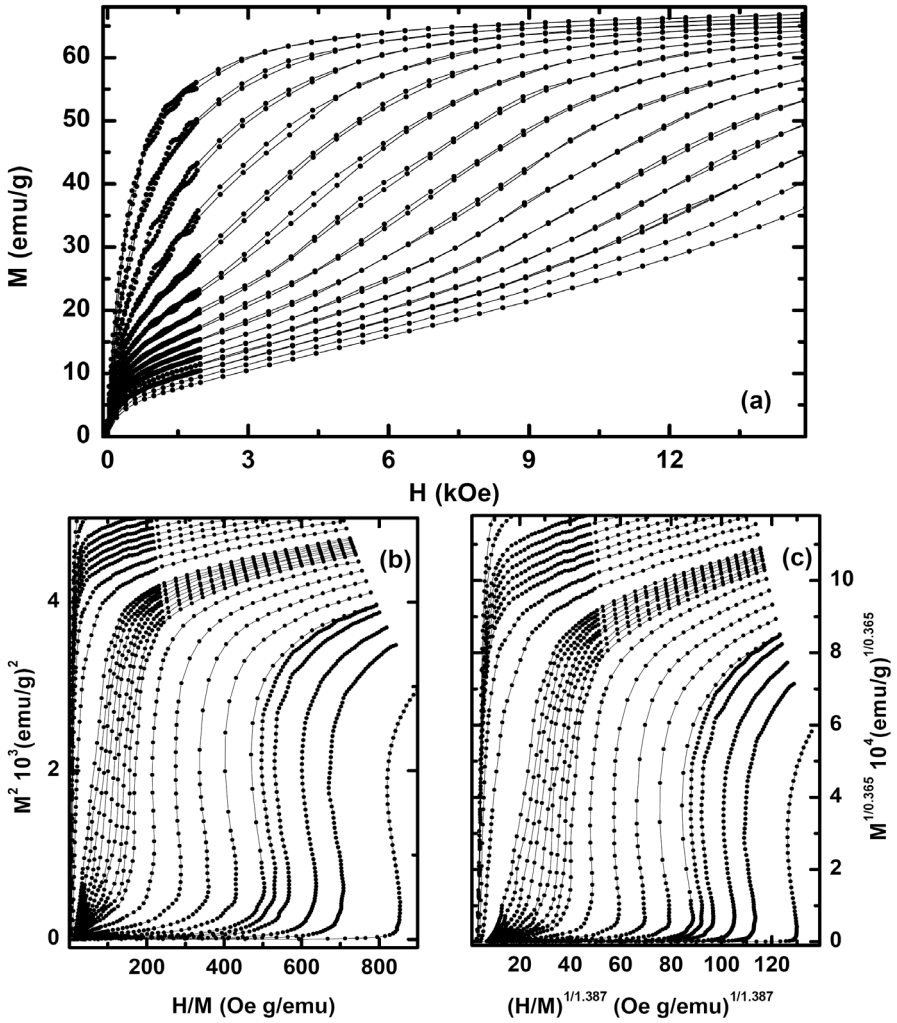

Figure 4.17 *Coexistence of first/second order phase transitions in x = 0.27. (a) Selected magnetic isotherms measured on increasing temperature from 234 K to 238 K in 1 K steps for fields up to 15 kOe. The existence of hysteresis demonstrates that the transition is first order. (b) Arrott plots – H_i/M vs. M^2 – for magnetic isotherms from 210 K to 220 K in 5 K steps, and from 222 K to 260 K in 2 K steps. (c) Plot of $(H_i/M)^{1/1.387}$ vs. $M^{1/0.365}$ as data in (b).*

contiguous. This plot exhibits curvature at low field [108], but nevertheless admits a reasonable extrapolation yielding T_C = 228 ± 3 K (close to the inflection point in the zero-field ac susceptibility, Figure 4.8 (g)). This behavior supports the assertion that in this x = 0.27 single crystal, the characteristics of both first-order and second-order transitions are essentially *coincident*.

And (ii) to note that above this transition line the present data demonstrate the continuing presence of Griffiths-like phase behavior, although measurements at still higher Ca substitution (approaching optimal doping, x = 0.33) indicate the termination of such behavior with the existence of a first-order transition alone [18, 20].

4.2.3 Evolution of Ferromagnetism

The present investigations provide a careful delineation of the compositionally driven MIT boundary as lying between 19 and 20% Ca substitution in this series of single crystals, thereby supplying incontrovertible evidence that the emergence of metallicity and ferromagnetism is *not* coincidental in $La_{1-x}Ca_xMnO_3$. The latter emerges prior to the former, prompting the question of what are the principal mechanisms underlying ferromagnetism in this composition range? As suggested recently [18,110], whereas FM-DE, stabilized by hole delocalization, dominates in the metallic regime immediately above the compositionally controlled MIT boundary [111], the relevant interaction below this boundary is *ferromagnetic* SE [112].

This proposal [18] is based on the evolution of SE with composition (x) in $La_{1-x}Ca_xMnO_3$. The SE-dominated, undoped parent $LaMnO_3$, exhibits in-plane FM interactions (the corresponding exchange coupling $J_{ab} > 0$), whereas intra/out-of-plane interactions are AFM (($J_c < 0$), leading to a quite different magnetic ground state from that prevalent at x = 0.18 and beyond. In the undoped parent the magnetic structure is induced/stabilized by the orbital ordering [85] (viewed alternatively, it is a consequence of the semi-empirical KGA rules in which the sign of SE coupling is modulated by the Mn-O-Mn bond angles and bond lengths [84]). Neutron scattering measurements [111] has provided evidence at the microscopic level regarding the evolution of SE coupling with doping level in this system, showing that while the magnitude of FM-SE in-plane coupling, $J_{ab}(x)$, increase monotonically with increasing doping level in the region of interest here, the evolution of $J_c(x)$, the c-axis coupling is more complex [111], Figure 4.16. Specifically, $J_c(x < 0.125) < 0$ (as in the undoped parent), $J_c(x = 0.125) = 0$, while $J_c(0.125 < x < 0.22) > 0$, increasing roughly linearly with doping for $x > 0.125$. Thus *both* in-plane $J_{ab}(x)$ and intra-plane $J_c(x)$ couplings are positive/FM across the compositionally modulated MIT boundary and this is where ferromagnetism first emerges in $La_{1-x}Ca_xMnO_3$.

Two issues emerge immediately: the first concerns the universality class for the PM-FM transition between x = 0.18 and x = 0.20, which the above analysis demonstrates conclusively is that of the nearest neighbor 3-D Heisenberg model: the second relates to the critical amplitude, E of equation (2-21). The latter shows little

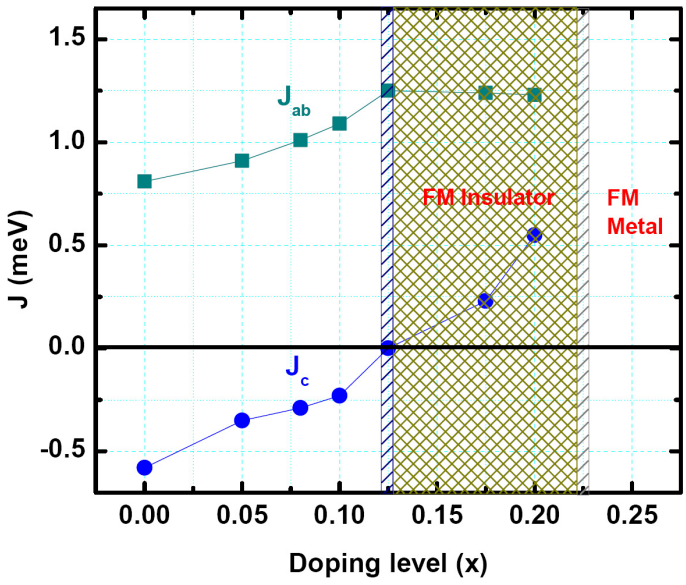

Figure 4.18 *Variation of magnetic coupling constants J, as a function of doping level (x). Data are reproduced from [111].*

across the compositionally modulated MIT between x = 0.18 and 0.20 (Table 4.1). To address the second question first, since this critical amplitude is a direct measure of the *number* of spins involved in the transition [113], then once the ferromagnetism is established (more appropriately in the present context, an infinite/percolating FM "backbones"), minor increases in the number of spins coupled to this backbone accompany further, additional increases in hole doping in this regime. Thus E should exhibit little variation with x across the MIT boundary, as observed. It is the dominant *mechanism* that changes from insulating to metallic phase. To estimate a critical amplitude such as E, the scaling behavior of the transition in question must fall into a specific universality class (i.e., exhibit a specific power-law dependence) – here that of

the isotropic 3-D Heisenberg model. Comparisons with samples exhibiting Griffiths-like phase characteristics, for the power-law along the critical isotherm is radically different, are thus inappropriate. For the universality class, Monte Carlo simulations for the DE model [114] *without* anisotropy do indeed predict that it should fall into 3-D Heisenberg system, as the analysis of the above data confirm.

However, DE coupling in systems with a *non-cubic* structure should acquire some anisotropy/directional dependence. That this is not observed in the current experiments likely reflects the scale of such anisotropy compared with thermal energies, k_BT_C, in the vicinity of the ordering temperature T_C. Similar comments apply in insulating samples where FM-SE is the principal interaction mechanism; here neutron data indicate that $J_{ab}(x)$ and $J_c(x)$ differ by only some 0.5 meV near $x = 0.19$ [111].

The current data indicate that exponent values characterizing this latter interaction also lie in the universality class of the 3-D Heisenberg model. While we are not aware of any theoretical prediction that confirms this result, data on the CMR pyrochlore $Tl_2Mn_2O_7$ in which FM-SE dominates, confirms such an assignment [47], as does the data on $Pr_{1-x}Ca_xMnO_3$ presented later. Indirect evidence supporting the above assertion is also provided by the use of the same model exponents in reproducing the dispersion relation for magnetic excitations measured at $x < x_c$ [111].

Such similarities notwithstanding, the data presented above indicate that the percolation threshold for these two interaction mechanisms are unequivocally different in $La_{1-x}Ca_xMnO_3$, despite the near-neighbor interaction range frequently assumed to

characterize them. The relative coupling *strengths* must, however, be comparable. The present data - acquired from samples with closely spaced compositions – indicate that dT_C/dx is unchanged (within experimental uncertainty) for compositions spanning the MIT boundary ($dT_C/dx = 3 \pm 1.4$ K for both the two insulating and the two metallic samples immediately adjacent to this boundary, with the actual "best fit" T_Cs yielding identical values for this slope across the boundary in question).

Support for the comparability of these two interaction strengths is also provided by estimates of the acoustic spin-wave stiffness, D [93], and the coercive field, H_C, respectively. To investigate the spin-wave stiffness in the present samples, measurements of the magnetization were carried out starting from 2 K in 2 – 5 K steps up to approximately half the ordering temperature ($T_C/2$), and estimates made of the spontaneous magnetization ($M_S(T)$) using extrapolations based on a modified Arrott-Noakes equation of state [43]. These estimates are reproduced in Figure 4.19 and have been fit to the well-known Bloch $T^{3/2}$ law [40], a temperature dependence originating from the assumption of gapless acoustic spin-wave excitations described in the usual notation by the dispersion relation $\hbar\omega_{ac} = Dq^2$, leading to the following expression for the temperature dependent spontaneous magnetization, $M_S(T)$, [40, 115]:

$$\frac{M_s(T)}{M_S(0)} = 1 - \frac{1}{NS}\left(\frac{k_B T}{4\pi D(T)}\right)^{3/2} \cdot \zeta\left(\frac{3}{2}\right) \qquad 4\text{-}8$$

$\zeta(3/2) = 2.612$ being the Riemann zeta function. A least square fit of these data to equation (4-8) yields the spin-wave stiffness, D and the zero temperature spontaneous magnetizations, $M_S(0)$ (Table 4.1). The former are plotted a function of doping level (x)

in Figure 4.19, from which it can be seen that D varies *smoothly* across the compositional MIT boundary [116]. This behavior of D thus correlates with the critical behavior, with lower D values (~ 65 meV A^2) appearing in both insulating and metallic samples exhibiting Heisenberg model exponent values. Quantitatively, $D = 2JSa^2$ [115, 117] for interacting near-neighbor spins (S) with separation a (at least, in cubic symmetry), J being the associated SE or DE interaction strength. Comparable values for D on either side of the MIT boundary thus imply comparable magnitudes for the prevailing dominant interactions. Figure 4.19 also shows that D increases sharply deeper into the metallic phase, but only at compositions at which a Griffiths-like phase occurs [19].

This result supports the initial suggestion, based on a study at x = 0.20 and 0.21 alone [19], that differences in behavior accompanying the latter in metallic samples are not simply manifested in a modified critical response appearing in the vicinity of T_C, but extend throughout the magnetically ordered regime. Furthermore, these values for D estimated for the insulating regime of $La_{1-x}Ca_xMnO_3$ agree with those in *ferromagnetic* $Pr_{1-x}Ca_xMnO_3$ (x = 0.27, 0.29) [118], discussed subsequently, where the ground state is not only insulating, but the critical exponents also fall into the universality class of the 3-D Heisenberg model, a point returned below. It is clear that the insulating character of this latter system precludes DE as a dominant coupling mechanism [15, 119], supporting the assertion made above regarding the universality class appropriate for $La_{1-x}Ca_xMnO_3$ in its the insulating regime.

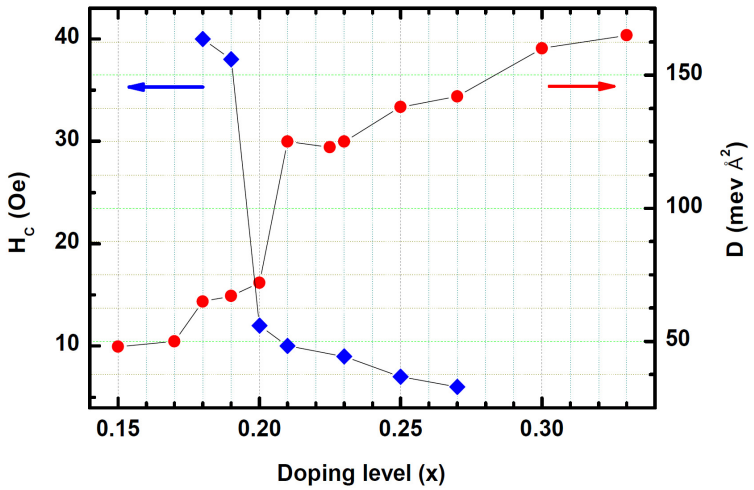

Figure 4.19 *Coercivity and Spin-wave stiffness as a function of doping level (x). Coercivity H_C at 10 K (left scale) acquired from both the magnetization hysteresis and susceptibility butterfly loops. Spin wave stiffness constant D (right scale) found from the low temperature spontaneous magnetization M_S. Data for x = 0.15, 0.225 and 0.33 are taken from [116].*

Finally, the coercivity, H_C, estimated from both magnetization isotherms and susceptibility butterfly loops at 10 K, increases sharply in those single crystals with an *insulating* ground state. As discussed previously, FM-SE emerges just below the (insulating) orbital ordering (OO) to (metallic) orbital disordering (OO*) boundary, thus ferromagnetism in this region is stabilized by orbital ordering [112]. As the coercivity is determined from the response of the magnetization/spin to applied fields, then the onset of orbital order would be expected to lead an increase in H_C. The presence of spin-orbit coupling combined with the specific orientational structure reflecting orbital ordering characteristics is equivalent to anisotropy, thus impeding any magnetization/spin rotation, leading to increased coercivity, as indeed is observed (Figure 4.19) (domain wall effects notwithstanding).

Furthermore, temperature dependent (magneto)transport measurements demonstrate that the compositionally modulated MIT lies between $0.19 \leq x_c \leq 0.20$ for $La_{1-x}Ca_xMnO_3$ [120]. A number of previous reports have been interpreted that an insulating ground state in this system can be linked to local structural changes – which control carrier (e_g electron) (de)localization [16, 110] – changes characterized quantitatively by the absence/presence of the so-called Jahn-Teller (JT) long-bond accompanying an OO insulating to OO^* metallic transition [16, 110, 112].

Summarizing the results on the $La_{1-x}Ca_xMnO_3$ system, the evolution of this system from the OO toward the OO* metallic state accompanying increasing levels of Ca substitution underlies the emergence of FM-SE (as seen in neutron scattering data [110, 111]). This latter interaction, it is argued, dominates the magnetic ordering process in the insulating phase immediately adjacent to the compositionally modulated MIT; on crossing the latter, DE becomes the dominant interaction as metallicity emerges. The compositional variations of both the acoustic spin-wave stiffness (D) and the coercive field (H_C) support this assertion.

The universality class of the transition accompanying both FM-SE and DE dominated ordering is shown to be that of the isotropic, near-neighbor 3D Heisenberg model; nevertheless, the percolation thresholds for these two interactions are manifestly different. Evidence of Griffiths-like phase appears in the low-field ac susceptibility for samples exhibiting both the insulating and metallic ground states, although such features are rapidly suppressed by small applied fields (the fields conjugate to *uniform*

ferromagnetism) for $x < 0.21$, leading to a Heisenberg model-like critical response. Combined with the magneto-transport measurements, the latter not only confirms that Griffiths-like phase features are *not* a prerequisite for CMR [19], but also impose the important caveat that Griffiths-like phase features do not *guarantee* the appearance of CMR.

With the adoption of a working definition of the Griffiths temperature, T_G, given earlier, viz., as the temperature marking the onset of a depression in the inverse zero-field ac susceptibility below its high-temperature CW form first [58] (marked by vertical arrows in Figure 4.9), a phase diagram for $La_{1-x}Ca_xMnO_3$ ($x < 0.33$) can be constructed, Figure 4.20. This affords comparisons with that reported previously for $La_{1-x}Sr_xMnO_3$ ($0.075 \leq x \leq 0.175$) [98] and later in this chapter for $La_{1-x}Ba_xMnO_3$ ($0.10 \leq x \leq 0.33$) [54, 99].

In $La_{1-x}Ca_xMnO_3$, the Griffiths-like phase regime terminates in close proximity to the MIT boundary, but, as mentioned above, the emergence of such features near this boundary may be particularly sensitive to various aspects of the underlying "disorder", possibly including the oxygen stoichiometry [104, 105] (the latter, mentioned earlier, may also play a role in the variation evident in T_C and T_G estimates in this Ca doped system, Figure 4.20, rather than differences between nominal and actual Ca substitution levels, as the discussion of Table 4.1 suggests). The termination of this region is consequently marked as hatched, the latter also delineating – likely non-coincidentally – the MIT boundary at $0.19 \leq x_c \leq 0.20$ in the series studied.

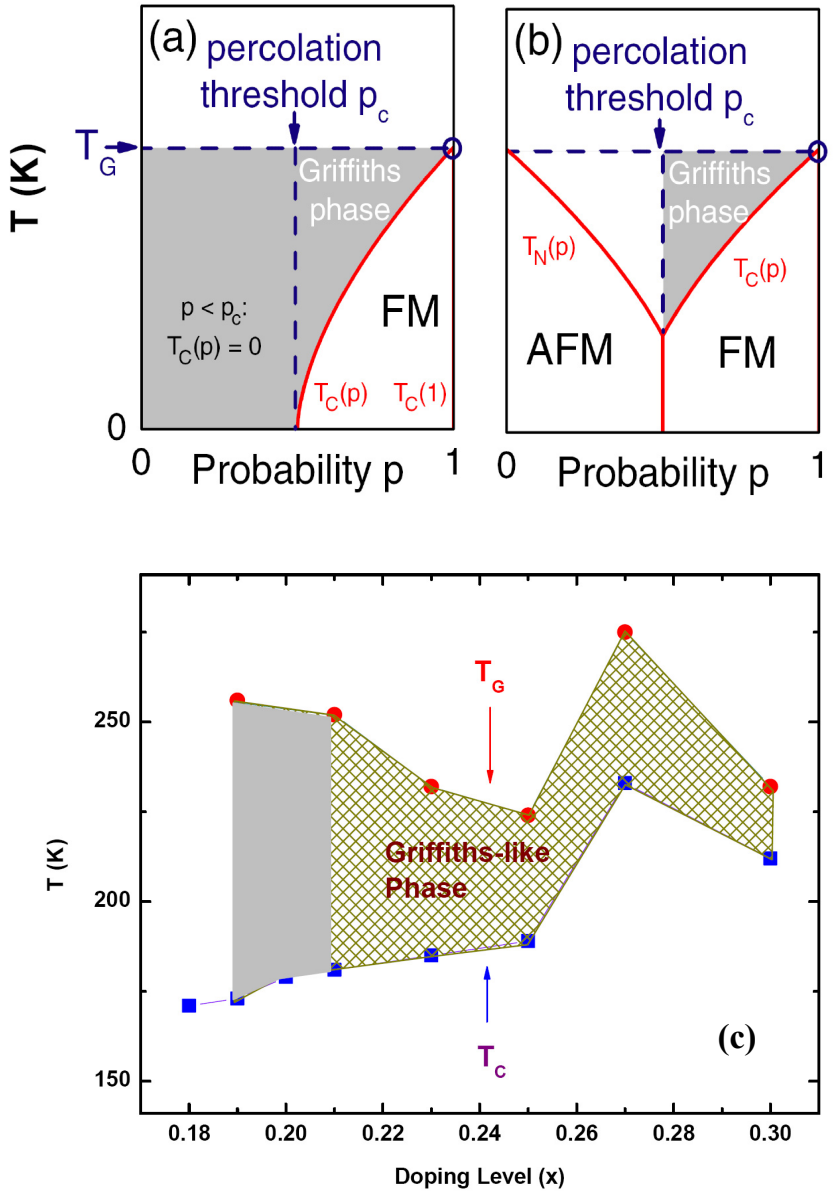

Figure 4.20 *The bond-diluted FM Ising model and phase diagram for $La_{1-x}Ca_xMnO_3$ ($0.18 \leq x \leq 0.33$). (a) The $T_G - T_C - p$ diagram for the bond-diluted FM Ising model [98], and (b) its conjectured $\pm J$ random bond Ising model counterpart. (c) Phase diagram for $La_{1-x}Ca_xMnO_3$ ($0.18 \leq x \leq 0.33$).*

The remaining lines – drawn as guides for the eye – join the T_G (upper) and T_C (lower) estimates, and initially appear somewhat different from the essentially triangular structure predicted by both Griffiths' original diluted FM Ising model and the ±J random bond approach, unlike the behavior for $La_{1-x}Ba_xMnO_3$ discussed later. While these data exhibit scatter around these model predicted boundaries, what is consistent with such predictions is the narrowing gap *between* T_C and T_G as the Ca doping is increased toward "optimal" levels, x = 0.33. Evidence supporting the narrowing gap between T_C and T_G around x = 0.25 can be seen in data reported in [121].

Elements of such scattering will also evident in $La_{1-x}Ba_xMnO_3$ near x = 0.27 [54, 99], while in $Sm_{1-x}Ca_xMnO_3$ [122] the reported T_G values are neither constant – they decline by some 6% between x = 0.85 and 0.92 – nor is the corresponding phase diagram reminiscent of the model-predicted forms mentioned above. All of the latter attest to the yet unresolved subtleties displayed by Griffiths-like phases in the manganites.

At compositions above the compositionally modulated MIT boundary, the emergence of metallicity is accompanied by CMR which, in model descriptions invoking phase separation, is based on the presence of FM conducting regions embedded in an *AFM insulating* background [3-4, 17, 21-23, 123]. It should be noted that the presence of a *FM insulating* phase at compositions below the MIT boundary is not in conflict with such a phase separation scenario. Ferromagnetism in insulating samples immediately below the MIT boundary results from FM-SE, stabilized by OO.

The emergence of metallicity is essentially coincident with a transition to an OO* state in which such FM-SE becomes destabilized, being replaced by AFM-SE characteristic of the parent compound, $LaMnO_3$.

4.3 Phase Diagram for $La_{1-x}Ba_xMnO_3$

Following the discussion on the $La_{1-x}Ca_xMnO_3$ system, a summary of magnetic and transport data an optimal doped $La_{0.7}Ba_{0.3}MnO_3$ single crystal is presented, with particular emphasis on the influence of disorder which nucleates a Griffiths-like phase in this and other $La_{1-x}Ba_xMnO_3$ single crystals [54].

Field and temperature dependent ac susceptibility measurements provide a powerful technique for investigating continuous magnetic phase transitions, as detailed previously, complementing conventional techniques. The corresponding data on the present single crystal are reproduced in Figure 4.21. The insert in Figure 4.21 (a) shows the zero field ac susceptibility, $\chi(0, T)$, measured on warming and cooling. While there is no measurable thermal hysteresis (on a scale of typically 0.5 K) associated with the magnetic transition near 310 K, hysteresis is evident in the temperature region 157 K < T < 187 K surrounding the rhomboheral $R\bar{3}c$ to orthorhombic Pbmn structural phase transition [124] (not the focus of the present study).

The maximum susceptibility value – evident in this insert – yields an estimate for the demagnetization factor $N_D = 1/\chi_{max} = 1/0.2119 = 4.72$ g Oe/emu. The main body of Figure 4.21 (a) summarizes the field-dependence of the ac susceptibility, which displays a series of peaks which decrease in amplitude ($\chi(H, t_m)$, and increase in temperature (T_m) as the applied field increases. Standard critical theory, presented earlier, indicates that the locus in temperature, t_m, and amplitude of these peaks are

governed by the power laws contained in equations (2-25) – (2-27).

Given the success of the Heisenberg model [51] in describing the critical behavior in many manganites [15, 48, 106, 107], an attempt was made to find a quantitative estimate for T_C using the above data in conjunction with equation (2-26), i.e., by plotting the measured peak temperatures, T_m, against the internal field, $H_i^{0.57}$, using the Heisenberg model prediction of $(\gamma+\beta)^{-1} = 0.57$ [13]. The data are well represented by this form, and an extrapolation to $H_i = 0$ yields an initial estimate for T_C. Typically this estimate is then used to construct double logarithmic plots of the reduced temperature

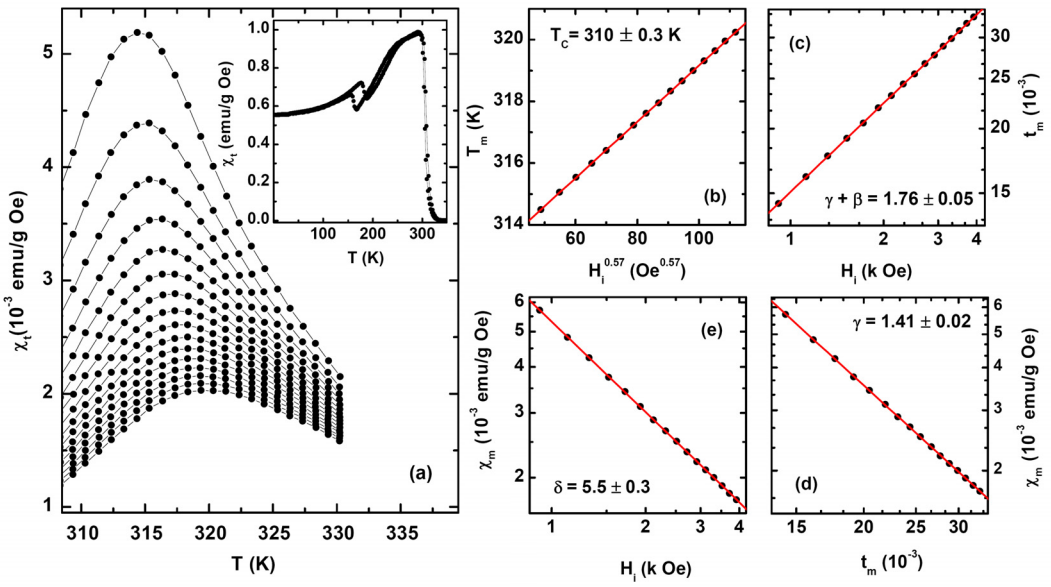

Figure 4.21 *Susceptibility analyses for $La_{0.7}Ba_{0.3}MnO_3$. Insert: zero field ac susceptibility, measured on warming and cooling. (a) The main body reproduces the variation of the critical maxima with increasing static fields from 1 kOe (top) to 4 kOe (bottom) in 0.2 kOe steps. (b), (c), (d), (e) are tests of the associated power-law predictions on log-log scales, corrected for background and demagnetization effects. (b) Estimate of critical temperature T_C, using susceptibility peak temperatures (T_m) against ($H_i^{0.57}$). (c) The reduced temperature (t_m), against the internal field (H_i). (d) The peak susceptibility (χ_m) against reduced temperature (t_m). (e) The peak susceptibility (χ_m) against internal field (H_i).*

t_m, against internal field (retesting equation (2-26)) and of the peak amplitude against t_m (equation (2-27)), with small adjustments to T_C until a consistent set of plots are obtained. In Figure 4.21 (e) the peak amplitudes from Figure 4.21 (a) (corrected for background and demagnetizing effects) are plotted against the internal field on a double logarithmic scale; this figure tests the remaining power law prediction, equation (2-25), and yields $\delta = 5.5 \pm 0.3$ (an estimate which does not depend on choice for T_C). Such an approach confirms the corresponding power predictions and in the present sample yields $\gamma = 1.41 \pm 0.02$, $\beta = 0.35 \pm 0.04$, with $T_C = 310 \pm 0.5$ K (i.e., here the initial T_C is essentially unchanged). Notice that while the individual exponent values differ from Heisenberg model predictions, their sum (coincidentally) does not, thus validating the approach used to construct Figure 4.21 (c). These estimates for γ, and δ particularly, are slightly higher than Heisenberg model values ($\gamma = 1.387$, $\beta = 0.365$, $\delta = 4.783$) [51], however, the exponent values quoted obey the Widom relation $\gamma = \beta(\delta - 1)$ [35] within experimental uncertainty.

Confirmation of these exponent estimates is provided by the magnetization data. Figure 4.22 (a) shows such data collected along the critical isotherm ($T_C = 310$ K), with the insert in this figure evaluating δ independently using equation (2-21), viz., $M(H, T = T_C) = M_0 H^{1/\delta}$. A double logarithmic plot will then yields the exponent δ. For fields comparable to those used in Figure 4.21 (b), this double logarithmic plot yields $\delta = 5.5 \pm 0.3$. Figure 4.22 (b), demonstrates good collapse of magnetic isotherms near $T_C = 310$ K based on the usual scaling representation, equation (2-19), incorporating the

above exponent estimates; the latter demonstrates the convincing consistency with the ac susceptibility data.

Values of the exponent δ far in excess of the Heisenberg value have been linked with the onset of a Griffiths-like phase [18-20]. The characteristics of such a phase have been used successfully to reproduce CMR behavior in the $La_{1-x}Ca_xMnO_3$ system near optimal doping [18], as well as its variation with dopant species. Despite the result that the δ value in the present Ba-doped single crystal exceeds the model predicted value to a far lesser extent than values reported in its Ca-doped counterparts [18-20, 55], Figures 4.23 (a) and (b), which reproduce the low field dc and ac susceptibilities immediately above T_C, demonstrate clearly the depression of the inverse initial susceptibility in this temperature regime below its CW value, a result consistent with the formation of large

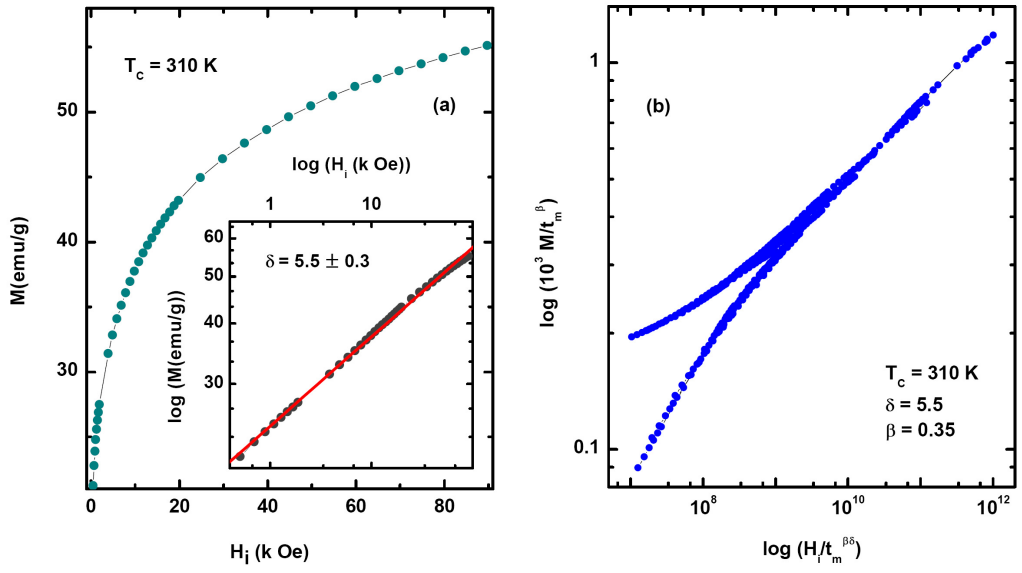

Figure 4.22 *Magnetization scaling analysis for $La_{0.7}Ba_{0.3}MnO_3$. (a) Magnetic data measured along the critical isotherm (T_C = 310 K), the insert estimates δ by repotting these data on a double logarithmic scale. (b) Conventional magnetization scaling plot using the critical exponents and T_C listed above.*

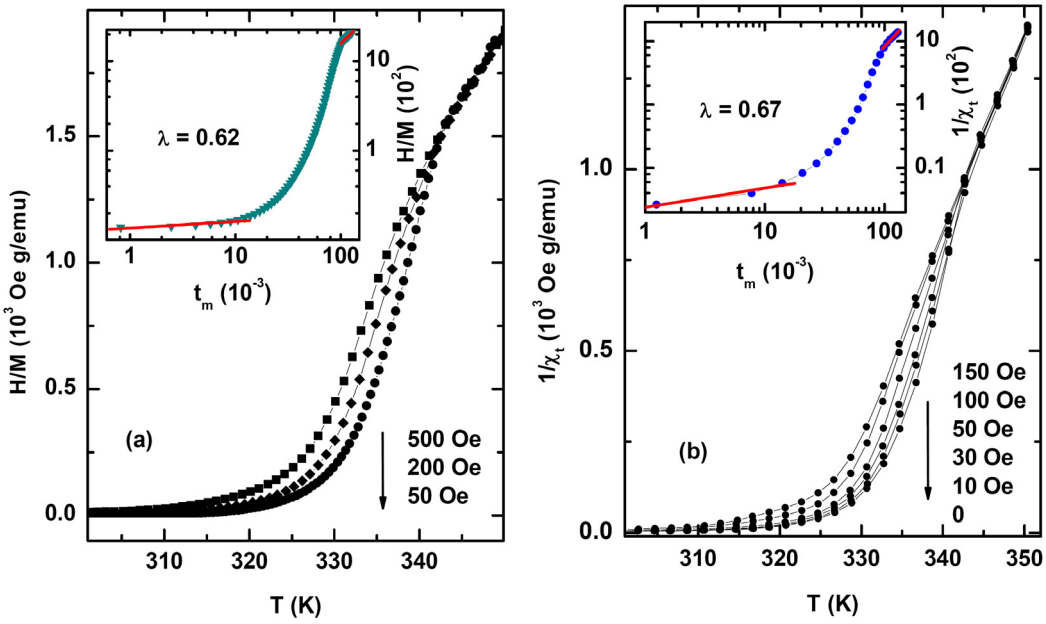

Figure 4.23 *Occurrence of a Griffiths-like phase in $La_{0.7}Ba_{0.3}MnO_3$. (a) The inverse dc susceptibilities plotted against temperature immediately above T_C in various static fields shown; the insert, a double logarithmic plot testing equation (2-31), yields a value of $\lambda = 0.62$ ($H = 20$ Oe) with $T_C^{Rand} = 310$ K. (b) The corresponding inverse ac susceptibility measured in various static fields, the insert yields $\lambda = 0.67$. All data were collected on warming following zero field cooling.*

correlated regions/clusters. The insert in these figures verify the power-law prediction of equation (2-31); specifically Figures 4.23 (a) utilizes a T_C^{Rand} of 310 K (a value which is consistent in *this* system with the Curie temperature T_C deduced from scaling analysis) with the associated fit to the 20 Oe dc data yielding $\lambda = 0.62 \pm 0.05$ ($310\text{ K} < T < 318$ K). The insert in Figures 4.23 (b) yields a consistent result, with $\lambda = 0.67 \pm 0.05$ from the zero-field ac data over the same temperature range. In the PM region ($T > T_G = 342$ K, with T_G chosen using the same criterion as Magen et.al., [58], viz., the onset of the departure of the inverse susceptibility from a CW dependence (as higher temperature

measurements – and fits to them – are not possible in our present magnetometer)), the corresponding exponent λ is close to zero (0.011), an anticipated result mentioned earlier, as the Griffiths-like phase evolves into a conventionally disordered PM state. The rapid suppression of the Griffiths-like phase with field evident in Figure 4.23 (the applied field being the conjugate field for uniform ferromagnetism rather than its disordered Griffiths counterpart, also mentioned above) is consistent with that reported earlier for an x = 0.27 Ba single crystal [59]; however, the λ value deduced here, being comparable to that found in a variety of doped manganites and other systems [18-20, 58, 60], is larger than that found at the lower composition. The latter likely reflects the result that at x = 0.27 the exponent values are considerably closer to Heisenberg model values. This point is returned to below.

Despite the differences in exponent values with the "regular" Griffiths-like phase systems [59], transport measurements on the present system reveal it displays standard CMR behavior, as Figure 4.24 demonstrates. The insert reproduces the associated magnetoresistance, $[\rho(0) - \rho(H)]/\rho(H)$, which, as expected, exhibits a peak near the MIT.

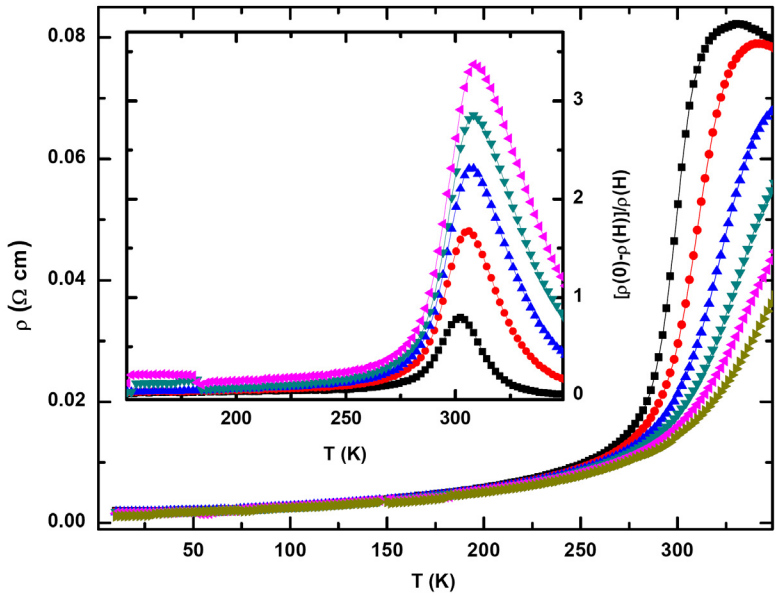

Figure 4.24 *Magneto-transport measurements on $La_{0.7}Ba_{0.3}MnO_3$. Resistivity in 0 (top), 10 kOe, 30 kOe, 50 kOe, 70 kOe, 90 kOe (bottom) measured on warming following zero field cooling; the insert shows the associated magnetoresistance.*

Combining the present data with an investigation of Griffiths-like behavior at a lower composition of x = 0.27, summarized in Figure 4.25 (the critical behavior of this single crystal was published earlier [106], and yielded exponents estimates $\gamma = 1.39$, $\beta = 0.38$, $\delta = 4.83$ with $T_C = 245$ K), with the recent interpretation of electron spin resonance measurements by Yatsky et.al., [99], and a range of previous measurements, enables a modified phase diagram for the $La_{1-x}Ba_xMnO_3$ system in the vicinity of the Griffiths regime ($x \leq 0.33$) to be constructed. In particular, the present measurements demonstrate unequivocally that the conjectured termination of the Griffiths-like phase between x = 0.2 and x = 0.3 needs to be corrected, as Figure 4.26 indicates; it extends to somewhat beyond x = 0.3, likely to optimal doping [125]. Differences in the absolute values for

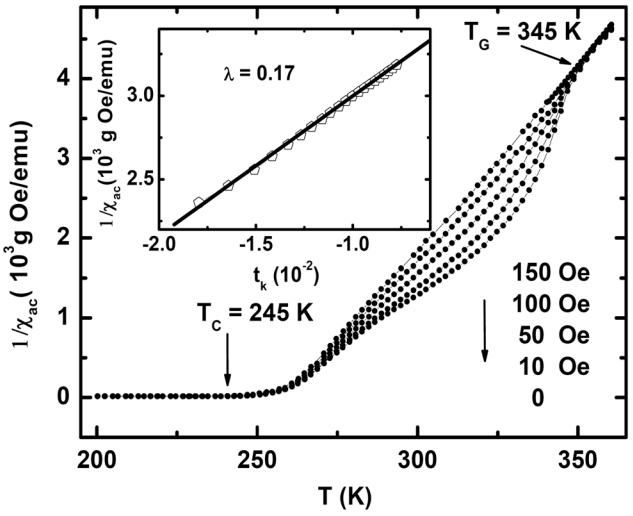

Figure 4.25 *Occurrence of a Griffiths-like Phase in $La_{0.73}Ba_{0.27}MnO_3$. The inverse ac susceptibility (1/χ) plotted against temperature immediately above T_C in various static fields shown; the insert, a double logarithmic plot testing equation (2-31) with T_C^{Rand} = 261 K) yields the "exponent" λ = 0.17. These data demonstrate the extreme sensitivity of the Griffiths-like phase in this system to field; this phase is completely suppressed by applied fields of 150 Oe.*

T_G, T_C and x notwithstanding (with the possible influence of oxygen stoichiometry, mentioned earlier), Figure 4.26 is strikingly similar to corresponding phase diagram determined for the $La_{1-x}Sr_xMnO_3$ system [98], which, in turn, was compared with the (T–p) diagrams for Griffiths' original diluted FM Ising model [56, 98] and that conjectured for its ±J random bond counterpart (Figures 4.18 (a) and (b)). Despite the overall agreement in mapping the compositional boundaries of the Griffiths-like phase in this Ba-substituted system using data from several experimental techniques, some fundamental questions remain. These include both the origin of the rapid suppression of Griffiths characteristics by field in this system and the associated variation of the exponent λ with composition. Suggestions [59, 100] that this might reflect the fact that

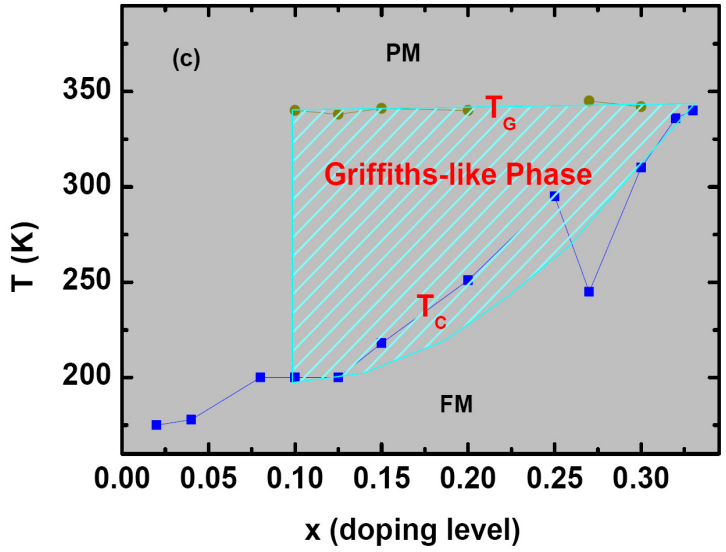

Figure 4.26 *Phase diagram for $La_{1-x}Ba_xMnO_3$. A summary of the current and prior observation of Griffiths-like phase boundaries for $La_{1-x}Ba_xMnO_3$ system ($x \leq 0.33$, see text). Data in the range of doping levels are cited from Ref [125].*

the average A-site, $\langle r_A \rangle$, in this Ba-substituted system near optimal doping is closest to that of the undistorted cubic perovskite structure (r_A^O) [100], appears to reproduce general trends at this doping level. Specifically that the disorder-corrected T_C – and by inference, T_G – is highest for optimally doped Ba compared to its Ca or Sr doped counterparts. However the broader assertion that $r_A^O - \langle r_A \rangle$ provides the appropriate criterion for measuring the "disorder" that underlies the tendency to nucleate a Griffiths-like phase, and the parameters that characterize it, is ruled out by detailed comparisons of the present data with that at x = 0.27 Ba doping [59], with the data on the Ca-doped system near the FM-metal to FM-insulator boundary discussed earlier in this chapter (and in [55]), and with the $La_{1-x}Sr_xMnO_3$ system [98]. Indeed, an inspection of the various structurally based parameters for these systems reproduced in Table 4.2

re-emphasizes the previous conclusion that not a single such parameter reflects the detailed variations in these temperatures, the exponent λ and the accompanying field dependence of Griffiths-like phase behavior, outlined above, away from optimal doping.

	x	$<r_A>$ (Å)	Tolerance Factor (t_f)	φ (Å)	T_C (K)	GP
Ba (T_G≈340K)	0.1	1.241	0.9290	0.0762	200	Yes
	0.12	1.247	0.9308	0.0825	200	Yes
	0.15	1.254	0.9335	0.0907	215	Yes
	0.2	1.267	0.9379	0.1016	251	Yes
	0.27	1.285	0.9442	0.1128	245	Yes
	0.3	1.292	0.9469	0.2997	310	Yes
Sr (T_G≈270K)	0.05	1.221	0.9217	0.0205	120	No
	0.08	1.224	0.9227	0.0255	140	Yes
	0.1	1.225	0.9234	0.0282	160	Yes
	0.12	1.227	0.9240	0.0306	180	Yes
	0.15	1.230	0.9250	0.0336	210	Yes
	0.2	1.235	0.9267	0.0376	310	No
	0.3	1.244	0.9299	0.0485	351	No

Table 4.2 *Parameters characterize some Mn perovskites, $La_{1-x}B_xMnO_3$.*

The earlier discussion of Ca-doped single crystals also revealed an anomalous behavior of the acoustic spin-wave stiffness, D, one that might be a precursor signal for the onset of a Griffiths-like phase, at least near the FM metal-FM insulator boundary at x = 0.19 in that system. The corresponding results for Ba-doped samples provide an interesting comparison. Using the well-known Bloch $T^{3/2}$ expression for the temperature dependence of the spontaneous magnetization below 80 K in the x = 0.3 single crystal (the spontaneous magnetization $M_S(T)$ being estimated from extrapolation of both Arrott-Noakes and conventional Arrott plots, either being equally applicable well away from the critical region) yields a value of the acoustic spin-wave stiffness D(0) = 147 ± 2 meV $Å^2$. This value is in excellent agreement with that reported for a Ba doped x = 0.3 polycrystalline sample (D(0) = 152 ± 3 meV $Å^2$) [126]. More importantly this value for D is well above that reported at x = 0.27 (D(0) = 66 ± 3 meV $Å^2$ [115] (the unusual behavior of the gap parameter at that composition notwithstanding). A rapid decline in the value of D in the Ca-based system coincided with the termination of Griffiths-like phase characteristics and the occurrence of critical behavior described by Heisenberg model exponents [59, 106, 115]. The parallels with Ba-doping are striking; as D declines sharply as x is reduced from 0.3 to 0.27, so do the critical exponents approach very closely to Heisenberg model values.

Nevertheless, vestiges of Griffiths-like phase behavior persist, although they display an extreme sensitivity to field and a much reduced value of the exponent λ = 0.17, correspondingly, the phase regime immediately above T_C at x = 0.27 exhibits but

minor departures from PM CW behavior. However, whereas in the Ca-doped system T_C and T_G converge as x is lowered to 0.2, immediately prior to the onset of the FM-insulator (with antiferromagnetism being established at still lower x values), in this Ba-doped system, Griffiths-like phase characteristics do not terminate when the composition x = 0.27 is approached from either above or below, but can be seen to persist well below x = 0.2 and likely up to optimal doping, x = 0.33, exhibiting ($T_G - T_C - x$) boundaries generally similar to $La_{1-x}Sr_xMnO_3$ [98].

In summary, analysis of magnetic data on single crystal $La_{0.7}Ba_{0.3}MnO_3$ yield values for the critical exponents $\delta = 5.5 \pm 0.3$, $\gamma = 1.41 \pm 0.02$ and $\beta = 0.35 \pm 0.04$ slightly larger than those of the three dimensional Heisenberg model. Subsequent measurements of the low field dc and ac susceptibilities reveal features consistent with the presence of a Griffiths-like phase. These data, combined with previous results, enable a phase diagram of the Griffiths regime for the $La_{1-x}Ba_xMnO_3$ system in the temperature-composition plane to be constructed, and in connection with the latter, the possible importance of the variation of the acoustic spin-wave stiffness with composition is outlined. Nevertheless, the evolution of Griffiths-like phase behavior accompanying compositional doping with any specific alkaline-earth cation, as well as the differences displayed using different dopant species, still present considerable challenges to our current understanding of these strongly correlated systems.

4.4 Phase Competition in $(La_{1-y}Pr_y)_{0.7}Ca_{0.3}Mn^{16/18}O_3$

The occurrence of a Griffiths-like phase in number of $La_{1-x}Ba_xMnO_3$ and $La_{1-x}Ca_xMnO_3$ single crystals has been discussed earlier in this chapter. While the relationship between the presence of this and related phases and the onset of CMR is the subject of ongoing discussion [18-20], the nucleation of this phase is linked unequivocally to the presence of disorder [56, 57]. In the context of the manganites, one pivotal question outstanding is whether there is one particular "measure" of disorder (magnetic disorder or structural disorder) which characterizes the appearance of a Griffiths-like phase [54, 59, 100]. While much previous effort, both present and by other authors, has focused on this issue in the $La_{1-x}Ba_xMnO_3$ and $La_{1-x}Ca_xMnO_3$ systems, amongst others, no definitive conclusion has been reached. In an attempt to address this issue, an analysis of systematic measurements of zero-field ac susceptibility on a series of fixed, "optimally" hole doped $(La_{1-y}Pr_y)_{0.7}Ca_{0.3}Mn^{16/18}O_3$ ($0 \leq y \leq 1$) polycrystalline compounds is presented. These, and the neutron data referred to below [82], were kindly provided by Dr. V. Pomjakushin and colleagues at the Paul Scherrer Institute.

The use of these specific samples importantly maintains not only a fixed number of DE linked Mn^{3+}-Mn^{4+} sites, but also a fixed number of Mn^{3+}-Mn^{3+} and Mn^{4+}-Mn^{4+} SE interactions (the possible influence of substitution on the magnitude and sign of these interactions notwithstanding), and in this sense the disorder is categorized as quenched disorder. Such an analysis, used in conjunction with previous neutron powder

diffraction data [82], indicates first that there is a close correlation between phase competition as measured by the relative volume fractions of the phase separated AFM and FM components, and the nucleation of a Griffiths-like phase, and second, the Griffiths-like phase in this system resembles that conjectured for the ±J random bond Ising model [56], in that it is confined to a restricted regime of the temperature (T)-probability (p) plane [98], p here being related to the relative FM/AFM volume ratio.

This analysis is based - following the Griffiths original idea of a diluted FM Ising ferromagnets [56] – on the characteristic temperature dependence for the susceptibility (χ), mentioned earlier in equation (2-31), viz., $\chi^{-1} \propto (T - T_C^{Rand})^{1-\lambda}$, with $1 < \lambda < 0$. This power law has been shown to reproduce the low field ac and dc susceptibilities immediately above T_C in the systems discussed earlier in this chapter and in a variety of other candidate Griffiths-like phase systems [18, 58, 101], its form demonstrating clearly the depression of χ^{-1} in this temperature regime below its CW value, as a result of the formation of large correlated regions/clusters [58]. Here T_C^{Rand}, and the transition or Griffiths temperature, T_G, of the undiluted system are determined from such data, as outlined below.

The main body of Figures 4.27 (a)-(e) present a selection of inverse zero field ac susceptibility data, which clearly monitors the nucleation and evolution of a Griffiths-like phase with composition in this optimally doped system. Data from ^{16}O doped samples are presented on the left and for ^{18}O doping on the right.

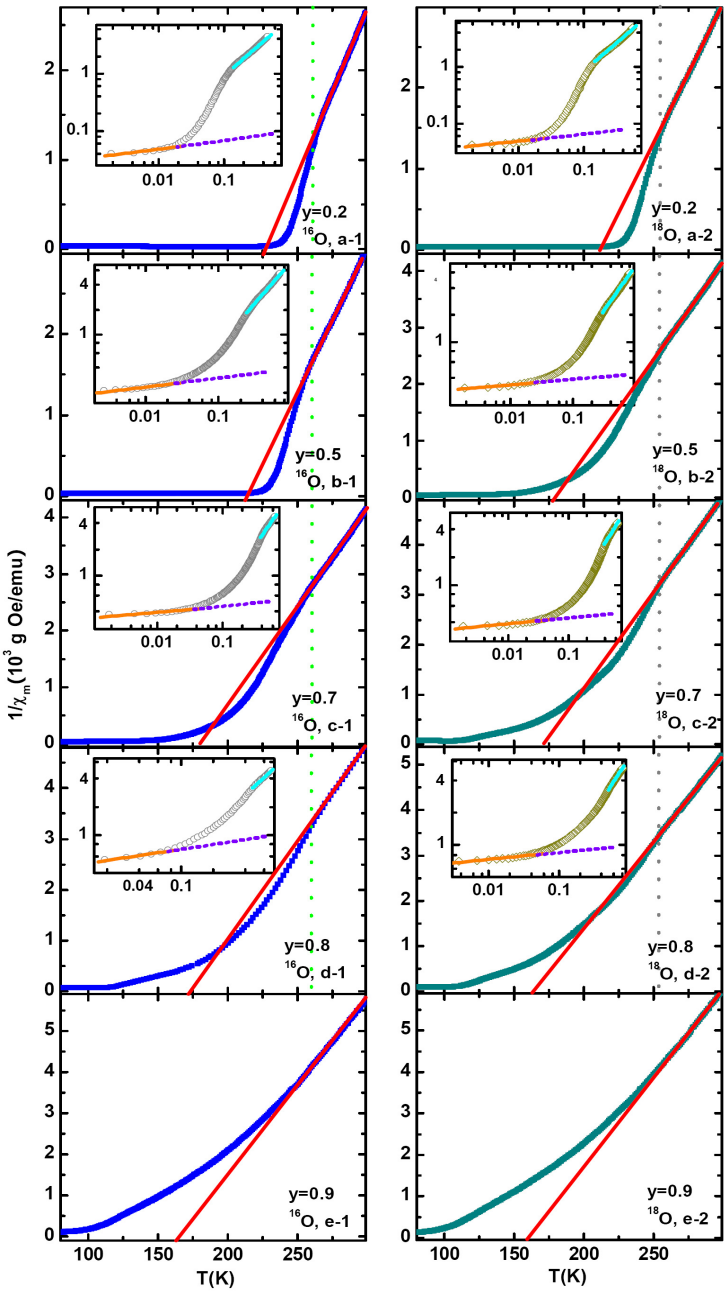

Figure 4.27 *Analysis of Griffiths-like phase in* $(La_{1-y}Pr_y)_{0.7}Ca_{0.3}Mn^{16/18}O_3$. *Main body: the inverse zero-field ac susceptibility against T, measured on warming;* ^{16}O *and* ^{18}O *data are shown on the left and right, respectively. The Pr substitution levels, y, are marked. The (red) straight lines (drawn immediately above* T_G*) represent a CW law. The vertical dash lines drawn through figures a1 – d1 (green) and a2 – d2 (gray) represent the corresponding estimates for* T_G. *The inserts replot these data on a double-logarithmic scale, testing the power-law equation (2-31) with* t_m, *the (orange) slope at low* t_m *yields the exponent* λ *quoted. The requirement that* $\lambda = 0$ *in the CW regime provides the estimate for* T_C^{Rand} *(the (cyan) line at higher* t_m *in the insert).*

Double-logarithmic plots of χ^{-1} against reduced temperature, $t_k = (T - T_C^{Rand})/T_C^{Rand}$, reproduced in the inserts in these figures, confirm the power-law prediction of equation (2-31) and yield estimates for the exponent λ (notwithstanding both the difficulties surrounding such estimates at small λ values and a precise theoretical interpretation for T_C^{Rand} currently. Viz., it lies above the actual ordering temperature (T_C) of the system, but below the highest ordering temperature admitted by the exchange bond distribution (T_G) [57, 58]). In addition, while estimates for λ at small values of t_m have proved difficult to obtain in some cases, the trend evident in Figures 4.27 (a) – (e) is unequivocal, a point returned to below. Further, while specific criteria exist for determining the PM to FM ordering temperature, T_C, and the Griffiths temperature, T_G, experimentally, viz., the inflection point in the zero-field ac susceptibility and the onset of marked departures from CW behavior [58-61], respectively, the choice of T_C^{Rand} has been less precise [58, 59]. Here a specific criterion is reiterated, one based on several previous reports [18, 19, 58] that fitting data in the PM regime above T_G to equation (2-31) yields a value for λ of zero when T_C^{Rand} is correctly identified. Such a criterion is based on the physically reasonable expectation that the Griffiths-like phase evolves into a conventionally disordered PM phase at high temperature.

This criterion translates into essentially estimating the CW temperature, θ, as done recently for the $La_{1-x}Ca_xMnO_3$ system [19], applied here to data immediately above T_G; its accuracy is correspondingly comparable (Table 4.3), as are the results reported for the isotope induced shifts in T_C [24]. The use of this criterion not only enables

experimental estimates for T_C^{Rand} to be acquired consistently, but it also avoids the unacceptable occurrence of both negative values for λ when choices of T_C^{Rand} below its correct value are adopted, and increasingly positive estimates for λ which emerge when too high a T_C^{Rand} is used in equation (2-31) (trends that are exacerbated in self-consistent approaches). Table 4.3 also lists the corresponding values for T_G ($T_G \approx$ 265 K for ^{16}O, and ≈ 260 K for ^{18}O, essentially constant for all samples exhibiting a Griffiths-like phase, except close to the critical composition, $y_c = 0.85$ in ^{16}O; this shift in T_G is somewhat smaller than the isotope induced shift in T_C), λ and T_C, parameters used subsequently to construct Figures 4.29 (c), and (d).

Irrespective of any detailed analysis based on equation (2-31), the clear observation of a depression of $1/\chi$ below its projected high-temperature CW form in Figures 4.27 (a1) – (d1) provides unequivocal evidence for the formation of large clusters/correlated regions [58-61], consistent with the formation of a Griffiths-like phase. Also clearly evident from Figure 4.27 (1e) is that higher levels of Pr substitution (y = 0.9) suppresses the nucleation of such clusters, and correspondingly, the Griffiths-like phase. The immediate implication is that $y_c = 0.85$ represents the compositional critical point below which a Griffiths-like phase is nucleated in this system (comparable results occur with ^{18}O substitution, Figures 4.27 (a2) – (e2), a point returned to below).

y	**0**	**0.2**	**0.5**	**0.7**	**0.75**	**0.8**	**0.85**	**0.9**	**1**
$<r_A>$ (Å)	1.205	1.200	1.192	1.187	1.186	1.185	1.183	1.182	1.179
φ (10^{-4} Å)	180	178	174	149	135	127	118	94	4.6
t_f (tolerance factor)	0.916	0.915	0.912	0.910	0.909	0.908	0.907	0.906	0.905
T_C (K) - ^{16}O	212	232	180	138	122	120	116	99	120
T_C (K) - ^{18}O	--	219	155	122	116	107	--	94	115
T_C^{Rand} (K) - ^{16}O	216	232	200	182	178	175	178	0	0
T_C^{Rand} (K) - ^{18}O	--	219	188	171	167	166	--	0	0
T_G (K) ^{16}O	245	265	264	265	265	267	228	0	0
T_G(K) ^{18}O	--	260	258	259	256	255	--	0	0
λ-^{16}O	0.33	0.15	0.13	0.09	0.08	0.07	0.05	0	0
λ-^{18}O	--	0.12	0.09	0.08	0.07	0.05	--	0	0

Table 4.3 *Static structural parameters characterizing $(La_{1-y}Pr_y)_{0.7}Ca_{0.3}Mn^{16/18}O_3$ ($0 \leq y \leq 1$). The ionic radii are from [87], the y = 0 data cited from [18]. "--" indicates no data available at that composition.*

The idea of a critical ratio in a phase-separated view of the manganites has been discussed recently [123], focusing principally on the thermal, not compositional, variation of this ratio. By contrast, and of immediate relevance to the present conclusion, is that analysis of previous neutron diffraction experiments [82], Figure 4.28 concluded that at this same composition the role of quenched disorder was pivotal in establishing a long-ranged phase separated state. The significance of this correlation is emphasized by an inspection of Figures 4.29 (c) – (f). The first of these reproduce the three characteristic temperatures T_C, T_C^{Rand} and T_G as a function of La replacement by Pr (y) (while maintaining optimal doping) in both ^{16}O (Figure 4.29 (c)) and ^{18}O systems (Figure 4.29 (d)); these phase diagrams exhibit a trapezoidal shape, similar to that first reported in $La_{1-x}Sr_xMnO_3$ [98], (and also $La_{1-x}Ba_xMnO_3$ discussed above and in [54]), which replicates aspects of the conjectured phase diagram for the FM regime of the ±J random bond Ising model.

These figures also emphasize the precipitous drop in T_G beyond $y_c = 0.85$ where a Griffiths-like phase fails to nucleate, again inviting comparison with the AFM region of the ±J random bond Ising model. Before proceeding to the evolution of FM/AFM volume fraction, it is necessary to point out the main result from powder neutron diffraction in the present system, as outlined below. The effective FM moment (a) and AFM moment (b) is the product of the real moment and square root of the volume occupied by the corresponding ordered phase, and is obtained from data measured at temperature T = 15 K, Figure 4.28, see [82] for measurement and other details.

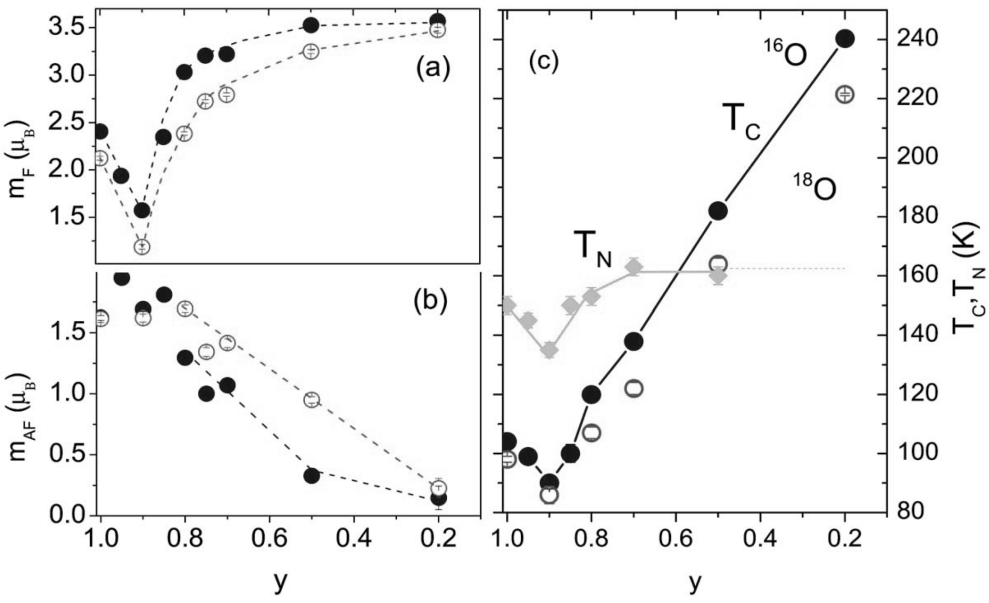

Figure 4.28 *Estimates of the effective FM/AFM moments. FM moment m_F (a) and AFM moment m_{AF} (b) at T =15 K, (c) Néel (T_N) and Curie (T_C) temperatures determined from the Neutron Diffraction data as a function of y in $(La_{1-y}Pr_y)_{0.7}Ca_{0.3}Mn^{16/18}O_3$. The lines are guides for the eyes. ^{16}O and ^{18}O samples are shown by closed and open symbols, respectively. T_N for the samples with different oxygen isotopes are the same.*

The current analysis utilizes the above neutron diffraction data [82]. These data not only demonstrate the presence of competing phases, but also confirm that an AFM component can be detected at all compositions down to y = 0.2 (at this latter composition the AFM volume fraction is, not unexpectedly, very small, viz., the effective AFM moment $m_{AFM} = 0.24\ \mu_B$ [82]). The important result demonstrated here is that as the AFM phase fraction increases with the Pr substitution level, y, so the nucleation of a Griffiths-like phase is suppressed.

Utilizing a modified protocol based on Table 4.3 and Figures 11/12 of reference [82], along with the detailed technique given in the same reference, the FM/AFM volume fractions, m_{FM}(FM) and m_{AFM}(AFM) were estimated from the measured low

temperature (15 K) moments. This approach, assuming a pure AFM state moment of M_{AFM} = 2.26 μ_B and its FM counterpart M_{FM} = 3.57 μ_B, taken to be constant for the whole Pr (y) doping range and over the relevant temperature range, used in conjunction with the relationship: $(m_{AFM}/M_{AFM})^2 = 1-(m_{FM}/M_{FM})^2$, yields the FM (AFM) volume fraction, $(m_{FM}/M_{FM})^2$ (and vice-versa). The resulting FM and AFM volume fractions are reproduced in Figures 4.29 (e) (^{16}O) and (f) (^{18}O) as a function of y, enabling direct comparisons with Figures 4.29 (c) and (d) to be made.

This comparison demonstrates a marked correlation linking directly the nucleation of a Griffiths-like phase in this system – undoubtedly reflecting the presence of quenched disorder – but disorder quantified by the relative volume fractions of the phase separated FM and AFM components. In particular, the critical Pr composition, y_c = 0.85, above which λ vanishes and below which a Griffiths-like phase first forms, coincides with the emerging dominance of the FM phase fraction. These figures also demonstrate that in the presence of competition between phase separated AFM and FM regions/clusters, the occurrence of a Griffiths-like phase is indeed confined to a restricted region of the temperature-probability (T-p) phase diagram, again showing similarities with predictions for the ±J random bond Ising model [56, 98], Figures 4.29 (a) and (b). Here however, the relevant probability (p) parameter is not simply the A-site occupation, *per se* [56, 98], but the relative AFM/FM volume fraction modulated by Pr doping, with the experimentally determined compositional threshold at y_c = 0.85 (equivalent to p_c = 0.5 in the ±J random bond Ising model [56, 98]).

The consensus of current work is that a Griffiths-like phase in the manganites originates from quenched disorder; here an attempt is made to isolate one principal characteristic of this disorder which can be linked to the nucleation of a Griffiths-like phase. The advantages accrued by using a system maintained at optimal doping have been discussed earlier; nevertheless, it should be reiterated that a consequence of changing the La-Pr ratio even at fixed (total) doping is that the Mn-O-Mn bond lengths and angles are inevitably modified [127].

The prior attempts to provide a unified description of the properties of doped-manganites [102] (and cuprates [103]), mentioned earlier, have been based on the use of predominantly *static* structural factors, specifically $\langle r_A \rangle$, and φ as discussed earlier (although changes in both the Mn-O and O-O bonds occur on passing through T_C [127]). Such discussions, however, made no quantitative predictions relevant to the present topic, viz., a comparison between the extent of structural disorder ($\langle r_A \rangle$, and φ) and the magnitude of T_G and/or T_C^{Rand} or the existence of a critical composition in this context.

The compendium of structural parameters collected in Table 4.3 simply facilitates the reiteration of the previous conclusion [54, 59, 100] that no such parameter – or indeed a combination of them-maps onto the behavior summarized in Figures 4.29 (c) – (d). In contrast, the present analysis offers a quantitative measure of phase competition and its correlation with the nucleation of a Griffiths-like phase. Specifically it demonstrates that the replacement of La by Pr (y) results in progressively decreasing

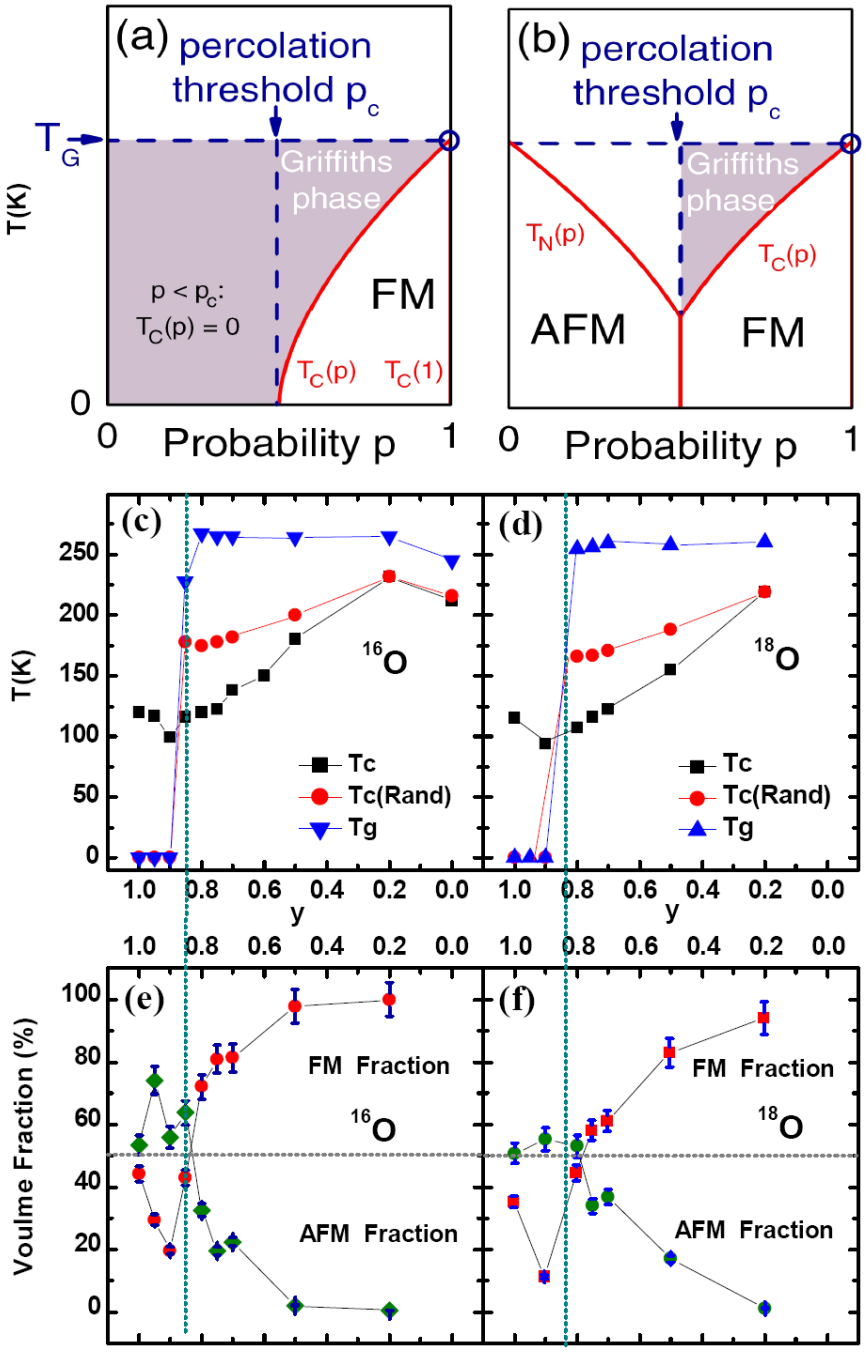

Figure 4.29 *Comparisons between the Ising model predictions and the estimated phase separated fractions. (a) The T_G –T_C – p diagram for the bond-diluted FM Ising model [98]; (b) its conjectured ±J random bond Ising model counterpart. Plots of T_G, T_C, and T_C^{Rand} vs. the Pr doping level, y, for the ^{16}O (c) and the ^{18}O substituted series (d). The associated AFM and FM volume fractions, calculated as described in the text, in the ^{16}O (e) and the ^{18}O series (f).*

values for the susceptibility "exponent" λ in the Griffiths-like phase regime, from a maximum value of $\lambda = 0.33$ at $y = 0$ to $\lambda = 0$ above the critical composition, $y_c > 0.85$.

It is particularly important to note that by maintaining optimal doping with $x = 0.3$, the lower bound of $0.04 < x_c < 0.1$ for the appearance of a Griffiths-like phase, estimated recently by Deisenhofer et.al., [98] based on the number of DE linked sites, is deliberately exceeded throughout the present system; nevertheless, a Griffiths-like phase is not ubiquitous, it nucleates only below a Pr probability compositional threshold (y_c) where the FM volume fraction dominates. The additional correlation between λ estimates in the Griffiths-like phase (once established) and the FM/AMF volume ratio adds support to this assertion, viz., these λ estimates fall monotonically as the Pr concentration approaches y_c and the dominance of the FM component diminishes.

Of course, there is a compositional upper bound beyond which a Griffiths-like phase fails to form, around $x = 0.3$ in the $La_{1-x}Ca_xMnO_3$ [18] series, as the present data confirm, but for which numerical estimates do not exist at present. The current analysis similarly shows that beyond this supposed upper bound a Griffiths-like phase can still be nucleated, with a constant number of DE linked sites, by manipulating the relative FM/AFM volume fraction.

At this point it should be recalled that phase separation underlies explanations of CMR based on models of carrier density collapse [128]. While such an approach can account for the transport behavior and various other observed properties of doped Mn perovskites and pyrochlores [128] – including marked disorder-induced effects [129] –

its predictions regarding a Griffiths-like phase in the vicinity of T_C have yet to be investigated in any detail. Indeed, in such an approach the magnetic transition is primarily first order, although, depending on the polaron density – which in turn reflects the relative magnitudes of the exchange coupling and the electron-phonon interaction – second order/continuous transitions are possible.

That a Jahn-Teller mediated electron-phonon coupling plays an important role in manganites is confirmed by isotope effects accompanying ^{18}O replacement of ^{16}O (Figures 4.27 (e1) and (e2) and Table 4.3). Such effects are, however, not dominant here; there is a small depression of some 5 K in T_G (likely due to a decrease in the Mn-O-Mn mode frequencies accompanying the oxygen mass increase [130]), and both T_C^{Rand} and λ are both slightly lower in ^{18}O doped specimens. This appears to reflect a similar reduction in the critical composition below $y_c = 0.85$, where, as with its ^{16}O counterpart, it again correlates closely with the emerging dominance of the FM phase fraction; the present data indicate that this phase competition is modulated, but certainly not suppressed, by the electron-phonon coupling, as is the accompanying establishment of a Griffiths-like phase.

In summary, systematic analysis of the ac susceptibility of a series of $(La_{1-y}Pr_y)_{0.7}Ca_{0.3}Mn^{16/18}O_3$ ($0 \leq y \leq 1$) indicates a compositional critical point $y_c = 0.85$ (^{16}O) above which a Griffiths-like phase does not nucleate and λ vanishes. Below this critical composition, the characteristic depression of the χ^{-1} below its high-temperature CW behavior, summarized by the power law $\chi^{-1} \propto (T - T_C^{Rand})^{1-\lambda}$, $0.05 \leq \lambda \leq 0.33$, is

clearly evident. The reanalysis of previous neutron diffraction data [82] demonstrates that for Pr concentrations $y_c > 0.85$, the AFM component in this phase separated manganite dominates; in contrast, the FM component is prevalent below this critical composition, and it is in this latter regime that a Griffiths-like phase first appears, despite the fact that all these optimally doped samples exceed the lower bound established for the emergence of a Griffiths-like phase in DE linked systems.

The result that the trend in the "exponent" λ also tracks this FM component suggests that the relative FM-AFM phase fraction in this phase separated system provides the appropriate measure of the disorder from which a Griffiths-like phase originates. That there is significant competition between states with differing magnetic characteristics (as opposed to disorder measured solely by structurally based parameters) is confirmed, for example, by the observation of a $T_C \geq T_N$ near $y = 0.5$; in particular, the latter demonstrate the presence of two energy scales, the existence of which underlies the appearance of CMR in several computational approaches [3-4, 17] which rely on such competition to establish intrinsically inhomogeneous ground states. In these strongly correlated systems in which charge, spin, orbital and phononic degrees of freedom are believed to play competing roles, phononic effects, while not dominant, can be seen through oxygen isotope effects.

At present, detailed measurements of the type utilized in this analysis are not widely available; this precludes the further testing of the link between the nucleation of a Griffiths-like phase with the phase separated volume fractions in other systems.

4.5 Ferromagnetic Insulator $Pr_{1-x}Ca_xMnO_3$

In contrast with the behavior of the doped manganites discussed above, $Pr_{1-x}Ca_xMnO_3$ is somewhat atypical in that the application of magnetic fields [131], X-ray irradiation [132], high electric fields [133], or laser radiation [134], have reportedly induced "unconventional" responses, making this system one of the more interesting perovskite manganites.

In $Pr_{1-x}Ca_xMnO_3$ compounds, while complications result for the presence of a Pr moment, the mismatch in cationic size is minimized, generating a pronounced orthorhombic distortion which favors the occurrence of charge-localization; $Pr_{1-x}Ca_xMnO_3$, unlike many of its counterparts doped with non-magnetic rare-earth ions, thus exhibits insulating behavior over an extended temperature range and all doping level in zero field [3, 4, 131]. Nevertheless, in all such materials, disorder plays a pivotal role reflecting the occurrence of nearly degenerate (and hence competing) ground states of very different character. In particular, disorder drives first order/discontinuous transitions towards second order/continuous in these systems; $Pr_{1-x}Ca_xMnO_3$, as discussed below, exhibits both types of transitions with changing compositions, x, and the disorder referred to above underlies spontaneous electronic phase separation, a central component in some theories of CMR [3-4].

Given the insulating ground state characteristics of $Pr_{1-x}Ca_xMnO_3$, phase separation scenarios are most frequently discussed in this system in relation to the MIT

accompanying the onset of a CO state, specifically in the higher hole doping range, $x \geq 0.3$ [3-4]. The simplest representation of phase separation envisages "domains" with CO AFM/insulating and FM/metallic characteristics, with the latter being enhanced by applied fields (the conjugate field for ferromagnetism), hence CMR. The onset of CO would also play a role in this context. Guided by the boundaries delineated most recently by the measurements of Lopes et.al., [135], to study the magnetic phase transition, the composition of the present samples was chosen to specifically avoid possible complications arising from a CO AFM contribution.

While at $x = 0.3$ the observation of marked hysteresis in both the magnetization, $M(T,H)$ and the magnetoresistance, $\rho(T,H)$, has led to the associated phase transitions being classified as first order, reflecting the importance of AFM interactions [131], for $x < 0.3$ FM coupling dominates; nevertheless insulating behavior persists even in high magnetic fields. Previous studies of magnetization and ac susceptibility in this doping range were aimed primarily at establishing the relation between ordering/Curie temperatures and doping levels [136], thus the universality class describing such ordering – best found from single crystals samples – has not been widely studied.

The focus of this section is to address this deficiency, and attempt to resolve the interesting question of whether the lack of metallicity in this system influences magnetic critical behavior, a topic that also arose in the $La_{1-x}Ca_xMnO_3$ system discussed earlier in this thesis. To reiterate, in the conventional DE picture, the onset of metallicity is linked with the establishment of an infinite (percolating) pathway of DE metallic

bonds, the same bonds that establish an infinite FM "backbone", so that the emergence of metallicity and ferromagnetism are essentially coincident [3, 4]. This is clearly not the situation encountered in Pr-doped systems; indeed, the insulating ground state characteristics of the specimens investigated here means that any influences of dynamic Mn^{3+}/Mn^{4+} charge fluctuation is more severely curtailed in them compared than even in their $La_{1-x}Ca_xMnO_3$ counterparts.

A summary of analyses of critical behavior in both the ac susceptibility and dc magnetization in single-crystal $Pr_{1-x}Ca_xMnO_3$ (x = 0.27; 0.29) is presented, supplemented by magneto-transport data. The zero field ac susceptibility measurement, Figures 4.30 (a) and (b) enable an estimate for N_D and a preliminary determination of T_C to be made. Theses measurements also indicate the absence of a Griffiths-like phase in both specimens (viz., no characteristic downturn in the inverse susceptibility). The magnetic data indicate that both single crystals exhibit a continuous/second-order PM to FM phase transition (Arrott plots show only positive curvature), with more detailed analysis indicating they display marginally different critical exponents, Figure 4.30. Estimates of the latter for the x = 0.27 sample yield $\delta = 4.81 \pm 0.02$, $\gamma = 1.36 \pm 0.02$, $\beta = 0.36 \pm 0.02$ (consistent with both the predictions for the nearest-neighbor 3-D Heisenberg model and with those reported for its DE dominated metallic counterparts) with $T_C = 127 \pm 0.5$ K, whereas at x = 0.29, $\delta = 4.62 \pm 0.05$, $\gamma = 1.38 \pm 0.01$, $\beta = 0.37 \pm 0.02$, with $T_C = 114 \pm 0.5$ K. The absence of metallicity – and by inference, the suppression of extensive charge fluctuations – does not, therefore, appear to influence

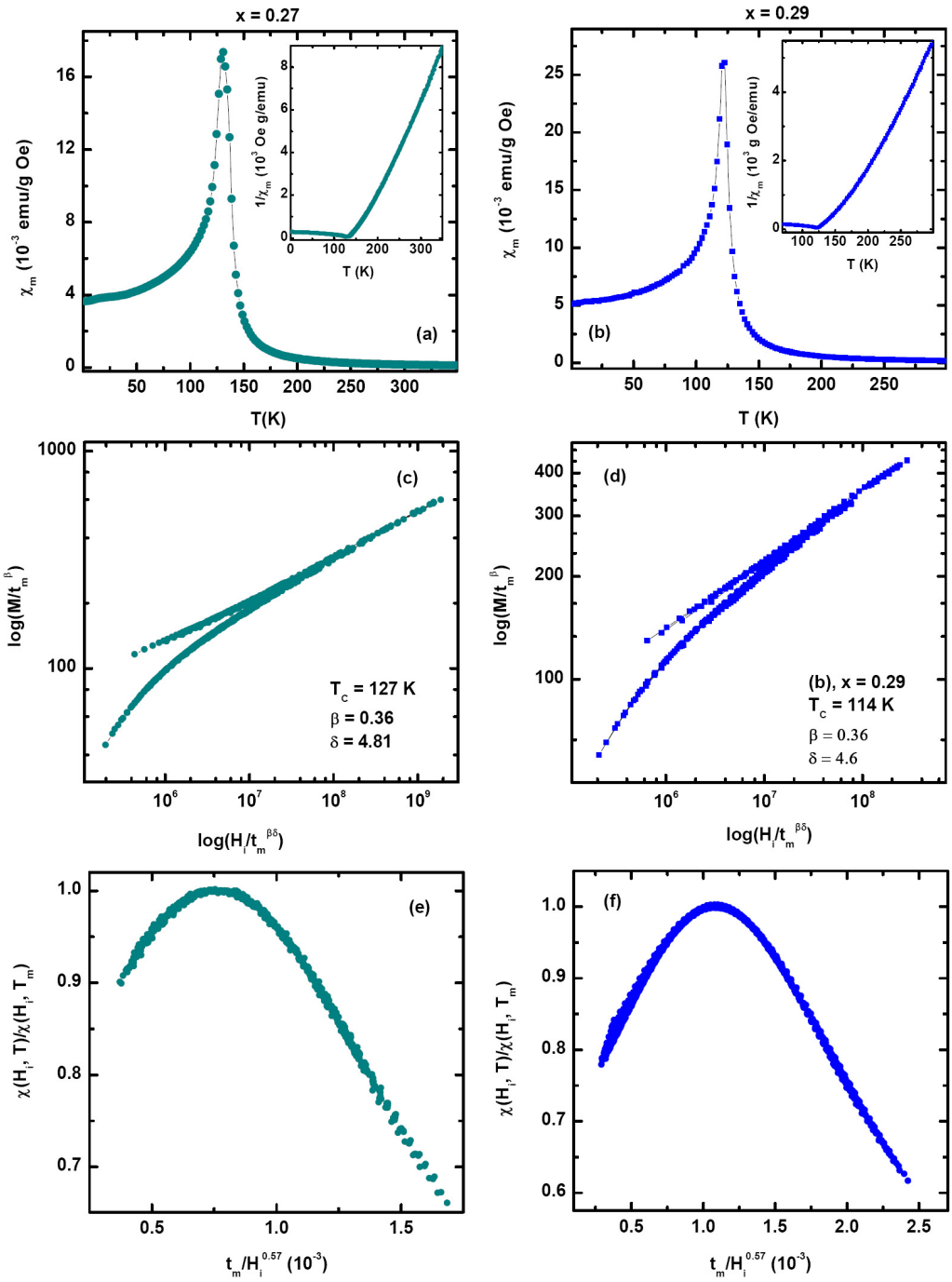

Figure 4.30 *Magnetic critical behavior of single-crystal $Pr_{1-x}Ca_xMnO_3$ (x = 0.27; 0.29). Zero field ac susceptibilities (a) for x = 0.27 and (b) for x = 0.29. Insets are the inverse susceptibilities. Magnetization scaling plots using the critical exponents and T_C values indicated above following equation (2-13). Plots (c) for x = 0.27 and (d) for x = 0.29. Plots (e) and (f) are the ac susceptibility scaling plot using equation (2-23). The good data collapse confirms the reliability of exponents and ordering temperature estimates.*

the universality class of the transition, a result consistent with the earlier data presented on Ca-doped single crystals. The Pr-doped single crystals also display comparable values for the acoustic spin-wave stiffness D ~ 70 meV $Å^2$ (from the Bloch $T^{3/2}$ law), well below that found in the CO, field-induced metallic regime of the same system.

For completeness, the transport behavior of these samples was also investigated. In the strictest sense of CO, no hopping contribution to the conductivity would occur, at least in the conventional DE scenario where uncorrelated hopping via a single intermediate oxygen atom alone is considered. The present specimens lie outside such a regime. Figures 4.31 (a) (x = 0.27) and (b) (x = 0.29) confirm that below the CO regime (x > 0.3) of this system, available field are unable to melt the FM insulating ground state [3, 4, 131]; conversely the retention of insulating characteristics in high applied fields provided indirect evidence against the occurrence of CO.

The continuous, semi-conductor like increase in the samples' resistance with decreasing temperature precluded measurements being carried out below 90 K. Nevertheless, the emergence of a small cusp near T = 125 K (x = 0.27), the previously determined ordering temperature, for H = 0 indicates that magnetic ordering influences the conduction process (albeit not nearly as dramatically as in "conventional" DE systems), an assertion confirmed by the associated magnetoresistance (insert in Figure 4.31).

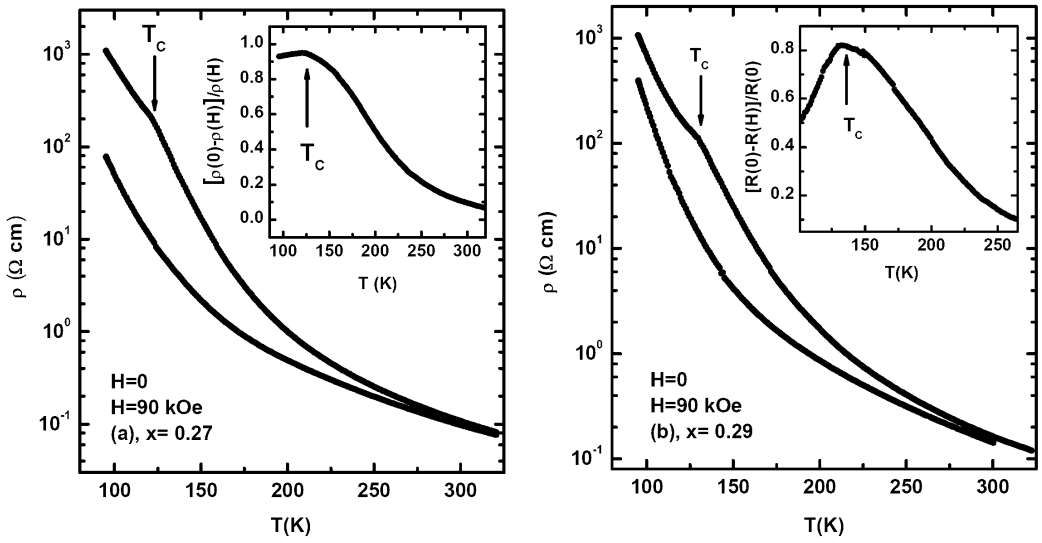

Figure 4.31 *Magneto-transport measurements of single-crystal $Pr_{1-x}Ca_xMnO_3$ (x = 0.27; 0.29). (a) Resistivities for x = 0.27 in zero field (top), 90 kOe (bottom) measured on warming following ZFC; insert, the magnetoresistance $[\rho(0)-\rho(H)]/\rho(0)$, which exhibits a peak near T_C, (b) as in (a) for x = 0.2*

In summary, the detailed magnetic and transport investigations in single-crystal $Pr_{1-x}Ca_xMnO_3$, reveal: (i) the establishment of ferromagnetism with the near-Heisenberg model exponents; (ii) the insulating features are prevailing in the present systems (x = 0.27; 0.29). The combination of these two features again demonstrates that metallicity and ferromagnetism are not coincident; hence confirming that the understanding of CMR in doped Mn perovskites demands a fundamental extension of the conventional DE model. In these Pr-doped specimens, the lack of detailed neutron data of the type discussed in relation to the $La_{1-x}Ca_xMnO_3$ system preclude a definitive identification of the underlying interaction mechanism as being ferromagnetic SE (which appears most likely) in the doping range of interest.

Chapter 5

Correlation Between Magnetism and Transport in $Fe_{0.8}Co_{0.2}Si$ $(Ga_{0.98}Mn_{0.02})As$

Identifying the universality class of magnetic critical behavior is fundamentally important as it reflects principally the range of the underlying interactions [35], from which inferences regarding the likely interaction mechanism(s) can be drawn. Typical experimental techniques used to address this problem involve, as discussed earlier in this thesis, measurements of magnetic isotherms, field-dependent ac susceptibility, heat capacity, etc., in the vicinity of the ordering temperature.

In this chapter, the universality class of magnetic phase transition will be established via scaling the anomalous Hall conductivity. Such a result establishes an AHE based methodology for systematically investigating critical behavior, particularly useful for potential spintronics devices, viz., systems with low dimensionalities/extremely weak magnetic signals.

5.1 Scaling of the Anomalous Hall Effect in $Fe_{0.8}Co_{0.2}Si$

The ferromagnet $Fe_{0.8}Co_{0.2}Si$ was studied in order to investigate this issue in general, and to demonstrate, in particular, the consistency of exponent estimates found using conventional methods with those deduced by scaling the AHE. Several motives underlie this choice. Specifically the large Hall resistivity exhibited by this system [30, 72] together with a transition temperature ($T_C \approx 36$ K) which enables the temperature regime both above and below T_C to be accessed with relative ease. Further, this system is topical, indeed controversial, due to its displaying an extraordinary *positive* MR ($\Delta\rho = [\rho(H) - \rho(0)]/\rho(0) > 0$) [28, 30] around T_C in both PM and FM phases, the origin of which is a subject of ongoing debate [28, 30]. Equally important, both the magnetization and magneto-transport of this system remain unsaturated in available fields, thus complicating subsequent analysis, a difficulty that the approach outlined below comprehensively addresses.

Figure 5.1 reproduces a selection of the temperature/field dependent magnetic and transport measurements. Figure 5.1 (a) displays the zero field ac susceptibility, measured on warming following zero field cooling; the peak evident around 36 K is consistent with previously reported results [28, 30], enabling subsequent measurements to focus on the transition region. Figure 5.1 (b) exhibits the temperature dependent transport data, which again agree overall with previous data reported on both poly- and single-crystal specimens. In particular, the positive MR evident in the inset attests to the

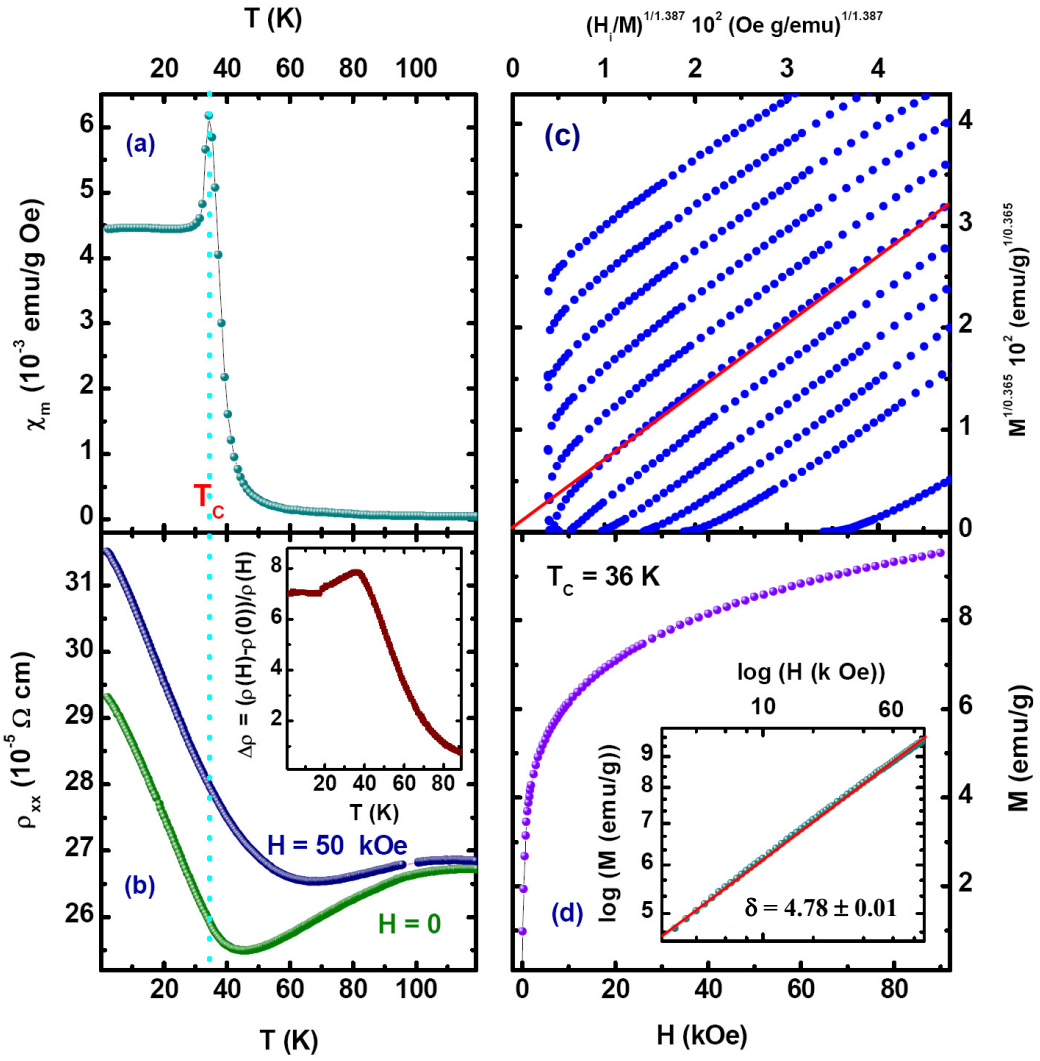

Figure 5.1 *Summary of magnetic and transport measurements on $Fe_{0.8}Co_{0.2}Si$. (a) The zero field ac susceptibility measured on warming following zero field cooling, the peak near 36 K is consistent with previous reports. (b) The temperature dependent transport data, with a positive MR evident in the insert. Figure (c) reproduces magnetization isotherm data close to T_C (i.e., 26 K to 44 K in 2 K steps and 50 K), in the from suggested by a modified Arrott-Noakes equation of state ($(H_i/M)^{1/1.387}$ vs. $M^{1/0.365}$), using Heisenberg model exponent values of $\gamma = 1.387$, $\beta = 0.365$, and $\delta = 4.783$. Figure (d) reproduces the critical isotherm, fitting to which yields $\delta = 4.78 \pm 0.01$.*

high quality of the present specimen. Figure 5.1 (c) reproduces the magnetization as a function of field at various fixed temperatures close to T_C in the form suggested by the modified Arrott-Noakes equation of state [43], viz., $(H_i/M)^{1/1.387}$ versus $M^{1/0.365}$, equation (2-18). The ensuing series of parallel straight lines indicate the applicability of essentially Heisenberg model exponents ($\gamma = 1.387$, $\beta = 0.365$, and $\delta = 4.783$) [51]. The equation-of state exponent determination is presented in Figure 5.1 (d), i.e., from data along the critical isotherm, yielding an experimental estimate for the exponent δ of 4.78 ± 0.01. The remaining individual exponent estimates are presented in Figure 5.2, yielding exponent values of $\gamma = 1.38 \pm 0.02$ from the inverse initial susceptibility, and $\beta = 0.37 \pm 0.01$ from the spontaneous magnetization.

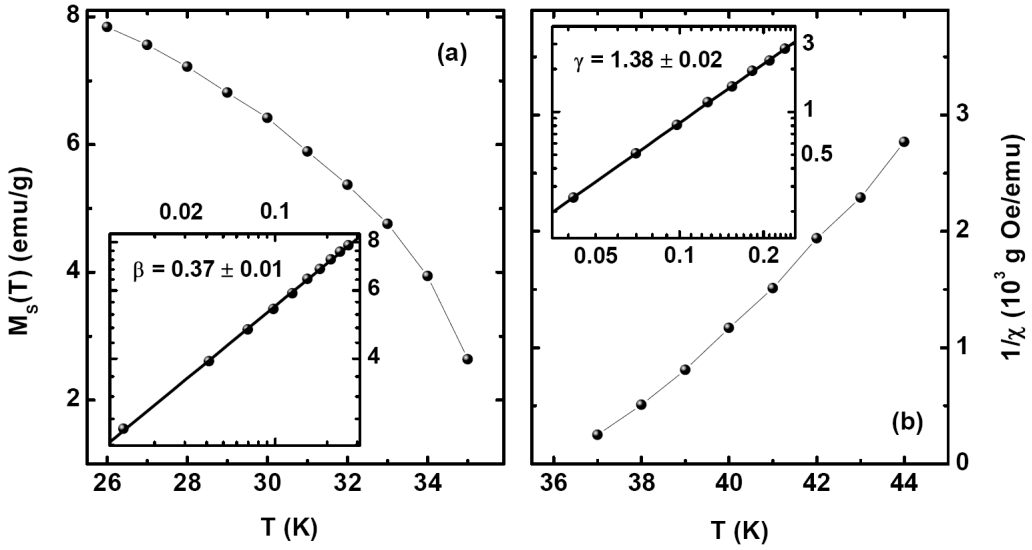

Figure 5.2 *Remaining magnetic critical analyses for $Fe_{0.8}Co_{0.2}Si$. (a) The spontaneous magnetization $M_S(T)$ plotted against temperature T: inset; M_S vs. $t_m = (T_C - T)/T_C$ on a log-log scale, yielding $\beta = 0.37 \pm 0.01$. (b) The inverse initial susceptibility, $1/\chi_i$, plotted against T: inset; $1/\chi_i$ vs. t_m on a log-log scale, yielding $\gamma = 1.38 \pm 0.02$.*

Figures 5.3 (a) and (b) reproduce the field-dependence of the Hall resistivity, ρ_{xy}, and of the longitudinal resistivity, ρ_{xx}. The issue of reliable estimates for the ordinary Hall coefficient, R_0, in this system needs to be addressed first. This can be done with reasonable accuracy in systems where the magnetization can be saturated in available fields. Here, however, such a situation is not realized, as the magnetization does not reach saturation even at 2 K in fields of 90 kOe [28, 30]; it thus needs to be emphasized that conventional approaches are not appropriate for this system. For example, dividing equation (2-38) by H yields $\rho_{xy}/H = R_0 + 4\pi R_S\chi$ (where the susceptibility here is given by $\chi = M/H$), so that plots of ρ_{xy}/H versus χ extrapolated from high field (low susceptibility) onto the ρ_{xy}/H axis yield R_0 [69].

However, under the conditions mentioned above, the values of R_0 so obtained, are overestimated (the carrier density n is underestimated), leading to uncertainties in R_S. Values for R_0 of the appropriate accuracy can be obtained – actually in conjunction with the establishment of the functional dependence for $G(R_S, \rho_{xx})$ – by using the result that irrespective of the precise form of the latter, plots of σ_{xy}^A versus M must extrapolate to $\sigma_{xy}^A = 0$ (as inferred directly from the relationship $\sigma_{xy}^A = \frac{4\pi R_S M}{\rho_{xx}^2}$). This is demonstrated in Figures 5.3 (c) in which plots of $\sigma_{xy}^A = \sigma_{xy} - \sigma_{xy}^O$ versus M in which the above constraint on the intercept have been implemented are reproduced (notice that this procedure *cannot* change any functional dependence of $\sigma_{xy}^A = \sigma_{xy} - \sigma_{xy}^O$ on M or ρ_{xx}). This procedure has broad potential application in other systems which remain unsaturated in high field.

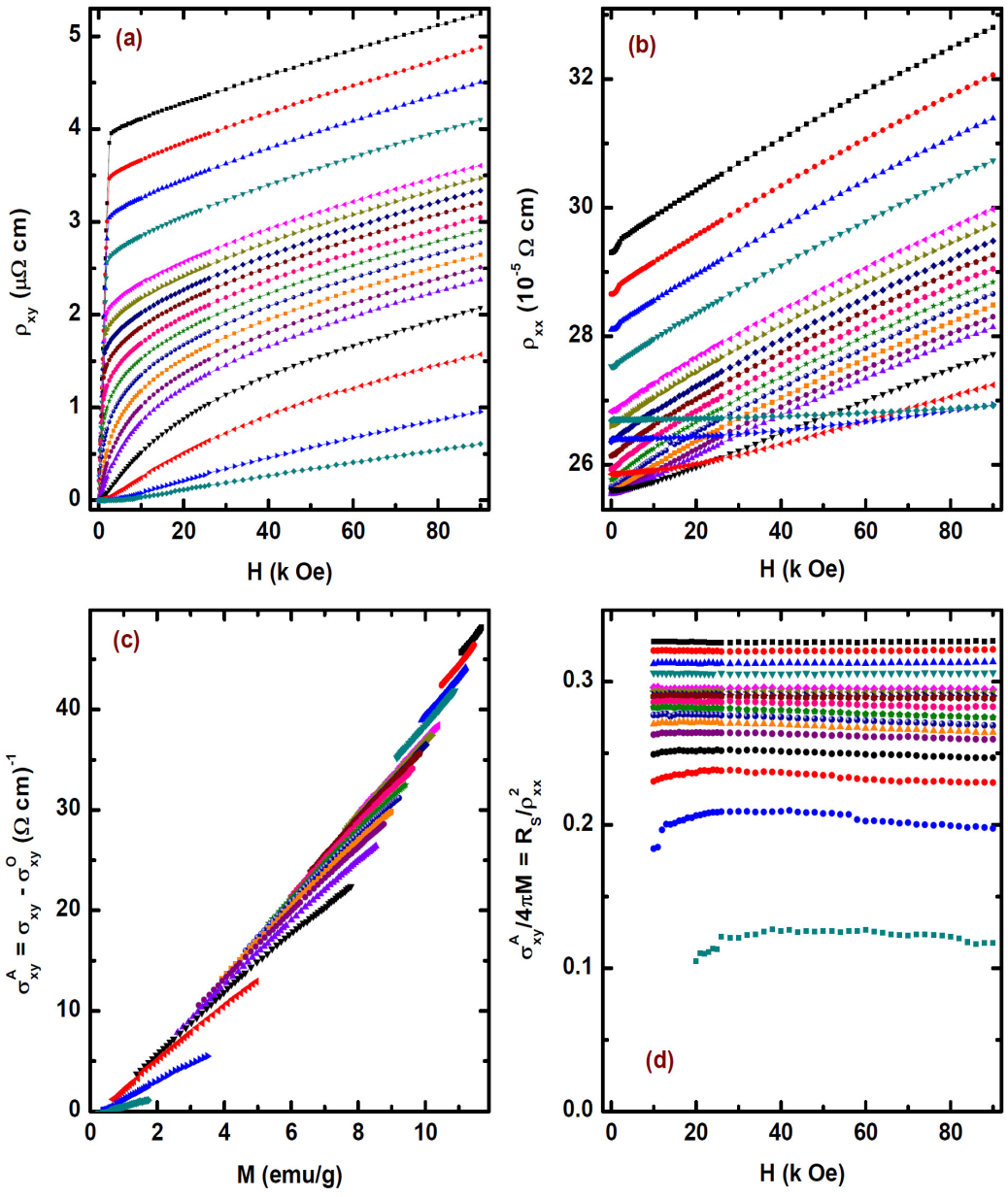

Figure 5.3 *Compilation of magnetization and magneto-transport data in $Fe_{0.8}Co_{0.2}Si$. (a) Selected field dependent isotherms of the Hall resistivity ρ_{xy} and (b) the longitudinal resistivity ρ_{xx} at 2, 10, 15, 20, 26-44 (in 2 K steps), 50, 60, 80, and 100 K in fields up to 90 kOe. (c) Plots of the anomalous Hall conductivity $\sigma_{xy}^{A} = \sigma_{xy} - \sigma_{xy}^{O}$ vs. M, the linear dependences of which (at each measuring temperature) yields $G(R_S, \rho_{xx}) = 4\pi R_S/\rho_{xx}^2$, with the accompanying temperature-dependent proportionality constant, K(T), see text. (d) Plots $\sigma_{xy}^{A}/(4\pi M) = R_s/\rho_{xx}^2$ vs. H demonstrate that R_s/ρ_{xx}^2 is indeed a constant at each temperature, and hence validates the relation $R_s \propto \rho_{xx}^2$ at specific temperatures.*

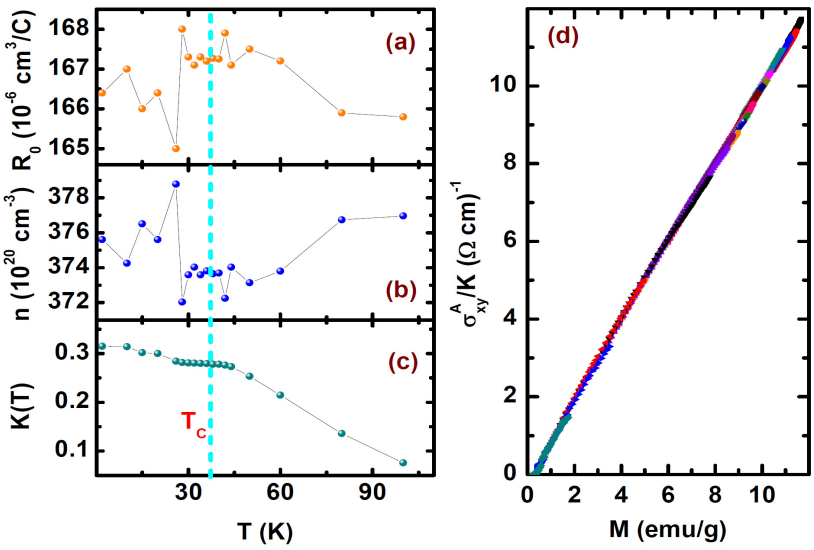

Figure 5.4 *Various parameters related to magnetism/transport scaling. Modified ordinary Hall coefficient R_0 (a), the corresponding carrier density n (b), and the proportionality between anomalous Hall coefficient R_S and magnetization M, K(T). (d) Scaling plot of the normalized anomalous Hall conductivity $\sigma^A_{xy} / K(T)$ vs. M, incorporating the measured values of ρ_{xx}, ρ_{xy}, and M.*

The first consequence of this procedure are improved values for the modified ordinary Hall coefficient, R_0, and correspondingly the hole/carrier density $n = \frac{1}{R_0 e} \approx (3.75 \pm 0.04) \times 10^{22}$ cm^{-3}, corresponding to approximately 0.5 carriers per atom (Figures 5.4 (a) and (b) respectively; note the expanded scale in these figures; the actual estimates vary by only some 2% below 100 K). The carrier density, combined with a finite resistivity at zero temperature indicates semi-metallic behavior, as opposed to the narrow gap semiconducting behavior of the undoped host. The above results indicate that across the FM-PM transition, the ordinary Hall coefficient (R_0) – and hence carrier density (n) – does not exhibit any measurable critical characteristics, at least in the

system studied. The technique utilized above can thus be used to address the question of whether R_0 and n exhibit critical behavior across the essentially coincident FM-PM and Metal-Insulator phase transitions, an issue of importance in the understanding of carrier-mediated ferromagnetism.

The second result, one of fundamental importance, is that Figure 5.3 (c) establishes the functional dependence of σ_{xy}^{A} on M as being linear with considerable accuracy. The function $G(R_S, \rho_{xx})$ is thus a constant at any given temperature, an immediate corollary to which is that $R_S \propto \rho_{xx}^2$ ($R_S = K(T) \cdot \rho_{xx}^2$), Figure 5.3 (d) a functional dependence that cannot be modified by the intercept constrain discussed above.

Prior to a discussion of the physical implications of this result, the linear dependence of σ_{xy}^{A} on M ($\sigma_{xy}^{A} = K(T) \cdot M$) for this system, established above, enables the scaling behavior of the AHE to be established, and from it the universality class of the transition. Specifically, the above results indicate that the normalized anomalous Hall conductivity $\sigma_{xy}^{A} / K(T)$ is simply a linear function of the magnetization M, a relation confirmed in Figure 5.4 (d), which incorporates data between 2 K and 100 K in field up to 90 kOe (further, such scaling incorporates measurements of ρ_{xx}, M and ρ_{xy}, a form more comprehensive than those advocated previously which involve just ρ_{xx} and M [28, 30]). Of particular importance in the present context is that the σ_{xy}^{A} versus M relationship in the critical regime assumes a particularly simple form; here, as Figure 5.4 (c) demonstrates, K(T) is essentially constant in the present system (Since the AHE is proportional to $\lambda \mathbf{E} \times \mathbf{M}$, **E** being the electrical field and **M** the magnetization tensors

[137], the parameter K(T) coupling transport/AHE and magnetism, should reflect the spin-orbit parameter λ, as well as the carrier-local moment or "s-d" coupling constant, depending on the model adopted).

This leads to a direct modification of the conventional Arrott-Noakes equation of state [43] by simply replacing the magnetization, M, by the anomalous Hall conductivity (equation (2-44)), viz., $\left(\frac{\sigma_{xy}^{A}}{\sigma_1}\right)^{1/\beta} = \frac{T_C - T}{T_C} + \left(\frac{H}{\sigma_{xy}^{A}}\right)^{1/\gamma}$. This prediction is tested in Figure 5.5 (a). Here the ensuing series of parallel straight lines resulting from the adoption of 3-D Heisenberg model exponents, together with an ordering temperature T_C = 36 ± 0.5 K (found from the critical anomalous Hall conductivity isotherm, $\sigma_{xy}^{A}(T_C)$, which passes through the origin), confirm the applicability of both equation (2-44) and the exponents mentioned, in describing the AHE data across the critical region. The intercepts of such linearized plots on the perpendicular axis, $(\sigma_{xy}^{A}/\sigma_1)^{1/\beta}$ at H = 0, yield the spontaneous anomalous Hall conductivity $\sigma_{xy-Spon}^{A}$. While the intercepts on the ordinate axis ($(H/\sigma_{xy}^{A})^{1/\gamma}$) yield a quantity analogous to the (inverse) initial susceptibility [$1/\chi_i(T) = (\partial H/\partial M)_{H=0}$]. As in conventional scaling, self-consistency is assured by taking these intercepts and (re)testing them against the analogous power-law relationships based on reduced temperature or field, making *small* adjustments (typically 0.1 K in T_C) until self-consistency is achieved. The final choices are shown in Figures 5.5 (b), 5.5 (c), and 5.5 (d), and their inserts. These yield δ = 4.78 ± 0.01, β = 0.37 ± 0.01, and γ = 1.38 ± 0.01 with T_C = 36 ± 0.5 K (with the latter error arising

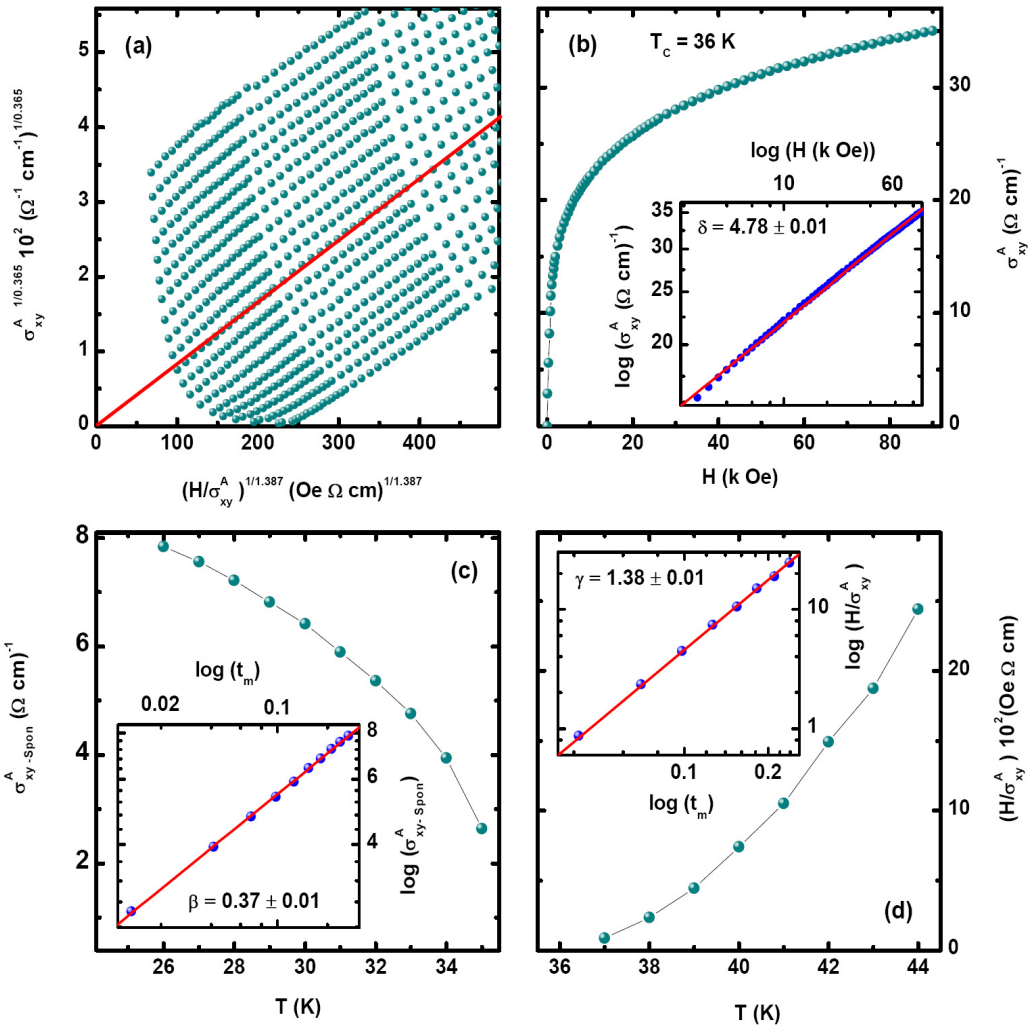

Figure 5.5 *Critical analysis based on the anomalous Hall conductivity* σ_{xy}^{A} *in* $Fe_{0.8}Co_{0.2}Si$. σ_{xy}^{A} *measured between 26 K and 44 K (in 1 K step). (a)* σ_{xy}^{A} *vs. H data reproduced in the form* $\sigma_{xy}^{A\ 1/0.365}$ *vs.* $(H_i/\sigma_{xy}^{A})^{1/1.387}$*; the resulting series of parallel straight lines confirm the exponent assignments, with the line passing through the origin yielding* $T_C = 36 \pm 0.5$ *K. (b) The critical anomalous Hall conductivity* $\sigma_{xy}^{A}(T_C)$ *vs. H; the inset shows the same data replotted on a double logarithmic scale, the slope of which yields* $\delta = 4.78 \pm 0.01$ *for 2 kOe < H < 90 kOe. (c) The spontaneous anomalous Hall conductivity* $\sigma_{xy-Spon}^{A}$ *plotted against T; inset,* $\sigma_{xy-Spon}^{A}$ *vs.* t_m *(reduced temperature) on a log-log scale, the slope of the straight line drawn yielding* $\beta = 0.37 \pm 0.01$*. (d) The quantity* H/σ_{xy}^{A}*, plotted against T; inset,* H/σ_{xy}^{A} *against* t_m*, similarly yielding* $\gamma = 1.38 \pm 0.01$*.*

principally from uncertainties in the absolute – not *relative* – temperature). These values not only demonstrate consistency with those found from the magnetization and ac susceptibility data, but are also very close to 3-D Heisenberg model predictions.

Finally these anomalous Hall conductivity data, σ_{xy}^{A}, have been scaled using the corresponding modification of equation (2-45), i.e., $\sigma_{xy}^{A}(H_i, t_m) = |t_m|^{\beta} \cdot F_{\pm}[H_i/(|t_m|^{\beta\delta})]$. Figure 5.6 (a) demonstrates conclusively that the data in Figure 5.5 (a) can be scaled onto the two expected branches resulting from data acquired below, F_{-}, and above, F_{+}, T_C. This figure confirms the unequivocal reliability of estimates of the critical exponents and the ordering temperature in this system using anomalous Hall conductivity data. The latter show that this system falls into the universality class of the isotropic, near-neighbor 3D Heisenberg model. Confirmation of this conclusion is provided by the more conventional scaling of the corresponding magnetization in Figure 5.6 (b).

The individual power-law dependences from the ac susceptibility data, equations (2-25)-(2-27), support the above assertion, yielding $\delta = 4.78 \pm 0.02$, $\beta = 0.38 \pm 0.01$, $\gamma = 1.37 \pm 0.02$, and $T_C = 35.9 \pm 0.2$ K, as can be seen from Figure 5.7.

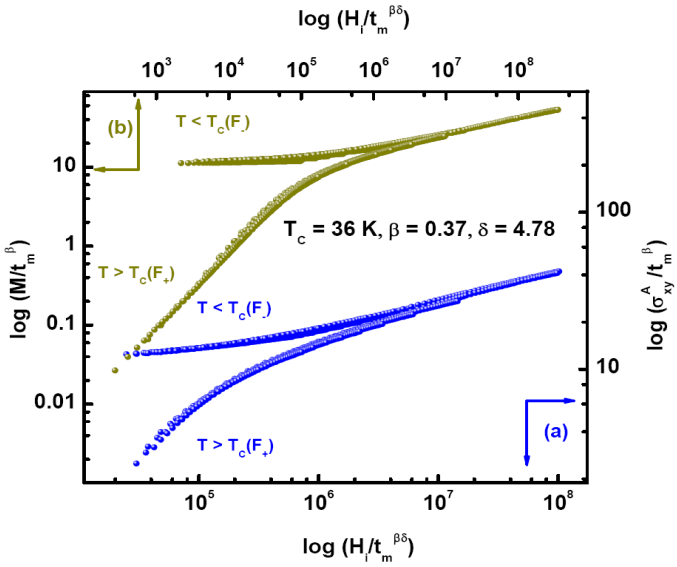

Figure 5.6 *Magnetic and transport scaling in $Fe_{0.8}Co_{0.2}Si$. (a) Novel scaling plot for σ^{A}_{xy}, using the critical exponents and T_C value listed in the figure. Plot of $\log(\sigma^{A}_{xy}/t_m^{\beta})$ vs. $\log(H_i/t_m^{\beta\delta})$ demonstrates convincingly the self-consistent determination of T_C and the critical exponents γ, β, δ. (b) Conventional scaling plot of magnetization M using the same exponent and T_C value. Upper/lower branches in (a) and (b) correspond to data below T_C (F_-)/above T_C (F_+) respectively.*

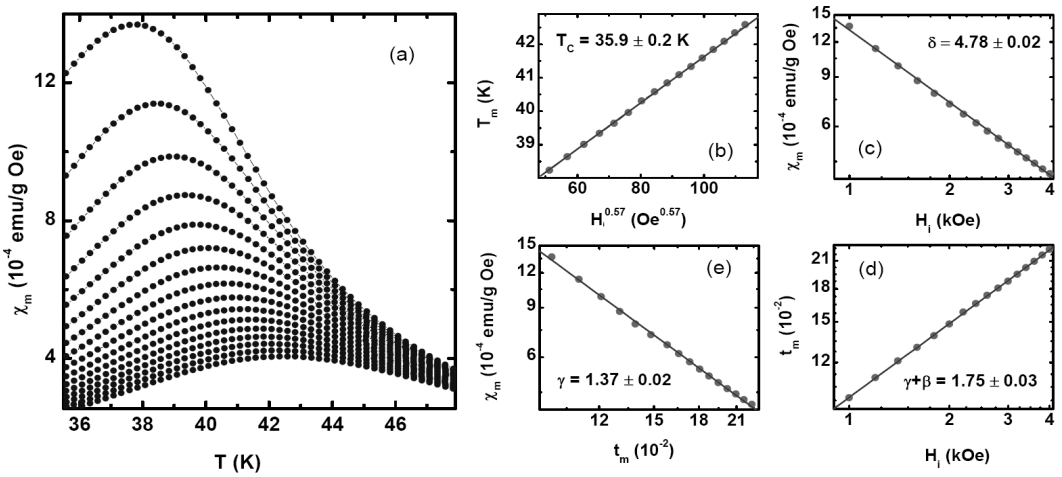

Figure 5.7 *Susceptibility critical analysis for $Fe_{0.8}Co_{0.2}Si$. (a) The critical maxima with increasing static fields from 1 kOe (top) to 4 kOe (bottom) in 0.2 kOe steps, corrected for background and demagnetization effects. Plots (b), (c), (d), (e) are tests of the power-law predictions on a log-log scale. (b) Estimate of critical temperature T_C, using susceptibility peak temperatures (T_m) against ($H_i^{0.57}$). (c) The peak susceptibility (χ_m) against internal field (H_i). (d) The reduced temperature (t_m), against the internal field (H_i). (e) The peak susceptibility (χ_m) against reduced temperature (t_m).*

Note that the field range (> 2 kOe) over which the magnetization and transport data were acquired is one in which the helical phase, present in this system at low temperature, is completely suppressed (H_C < 1.5 kOe at 2 K at this composition, a field that decreases as the temperature is increased towards T_C). Thus no complications/contributions from this phase appear [28, 30] in the field/temperature regime covered in the present experiments; the properties measured are indeed those of the ferromagnetic phase. This conclusion is reinforced by the fact that even in zero field the mean-free path below 100 K is much shorter than the helical period, so that the transport data reflect essentially short range – and hence effectively ferromagnetic – correlations.

The present data also provide information on the specific mechanism responsible for the AHE in $Fe_{0.8}Co_{0.2}Si$. That $R_S \propto \rho_{xx}^2$ excludes the possible of any significant asymmetric skew scattering [74] (for which $R_S \propto \rho_{xx}$), leaving side-jump scattering [75] and/or intrinsic contributions [76] as the underlying sources (both yield $R_S \propto \rho_{xx}^2$, a result of relaxation time τ (hence impurity density) independence [77]). To differentiate between these two possibilities requires the use of previous results acquired at various doping levels in $Fe_{1-x}Co_xSi$ ($0 \leq x \leq 1$); the analysis of the latter concluded that the Hall conductivity σ_{xy} is indeed a measure of the effective spin-orbit interaction, viz., the dominant mechanism is most likely intrinsic (originating as an electronic band structure effect), a result valid for $0 \leq x \leq 0.7$ [30].

Furthermore, the observation that $\sigma_{xy}^A = K(T) \cdot M$ in the current system is also

consistent with a recent theoretical calculation based on the sum of Berry phase curvature, a key prediction of which is that the intrinsic anomalous Hall conductivity $\sigma_{IAH} \propto M$ [138]. Indeed, the approach summarized above enables the normalized anomalous Hall conductivity $\sigma_{xy}^{A} / K(T)$ to be directly correlated with the magnetization, M, over wide temperature (2 K – 100 K) and field (90 kOe) ranges.

In summary, the present results demonstrate unequivocally that scaling behavior can be accurately deduced from measurements of the AHE. The data presented above also raise the possibility of systematically investigating the magnetic behavior of systems with low dimensionality/extremely weak magnetic signals via this technique. The latter could prove pivotal in improving our current understanding of the correlation between magnetism and transport in magnetic metals/semiconductors, particularly future generations of recording materials and spintronic devices. Finally, the present results ($R_S = K(T) \cdot \rho_{xx}^2$) offer support for the emerging consensus that the AHE in this system arises most probably from intrinsic/electronic band structure effects [77].

5.2 Universality Class from the Anomalous Hall Effect for (GaMn)As

Magnetic semiconductors are regarded currently as an important class of materials due, for example, to their potential application as injectors for spintronic devices [6, 27, 31]. In this context, GaAs has been the object of considerable recent interest since the discovery that it becomes ferromagnetic when Ga is replaced by Mn [6, 27, 31]. The study of critical behavior in ferromagnets such as (GaMn)As plays a pivotal role in understanding the physical basis of such behavior [6, 27, 31].

Establishing the universality class of any material provides insight into the range of the underlying interactions [35], from which the dominant interaction can often be inferred, for example, long/infinite range interaction in the case of Mean-Field exponents, as opposed to short range/near neighbor in the case of Heisenberg model values. The present study demonstrates conclusively that an epitaxial (metallic) $Ga_{0.98}Mn_{0.02}As$ microstructure is a Mean-Field ferromagnet by utilizing an unconventional scaling approach based on the AHE presented above.

The occurrence of the AHE in ferromagnetic (III, Mn)V semiconductors has not only been investigated extensively [6, 26, 27, 31, 77, 138-142], but theories for it in the metallic regime have also been proposed recently based on a Mean-Field prescription. In particular, the latter concludes the presence of an impurity scattering-independent *intrinsic* AHE in this regime [77], which yields $R_S \propto \rho_{xx}^2$ [77, 138, 139]. This

dependence is confirmed indirectly by the analysis presented below; subsequent scaling behavior based on the anomalous Hall conductivity demonstrates unequivocally the applicability of a Mean-Field approach. Specifically, inserting the predicted dependence of R_S into equation (2-42) leads to the result that the magnetization is *directly* proportional to the anomalous Hall conductivity, $\sigma_{xy}^{A} \propto M$, enabling the field and temperature variation of M to be extracted form magneto-transport data in a manner similar to that discussed above for $Fe_{0.8}Co_{0.2}Si$.

The onset of ferromagnetism in the low-doped $Ga_{1-x}Mn_xAs$ has been recently confirmed using a SQUID magnetometer [143], revealing the presence of a MIT accompanying the FM-PM phase transition. Figure 5.8 presents the temperature (T) dependent magnetization M(T) (measured at 50 Oe) and resistivity (ρ(T, H)) measured in different static magnetic fields (H). The first order temperature derivative in M(T) exhibits a minimum at T ≈ 56 K, providing a preliminary estimate of the ordering temperature, thus enabling the subsequent measurements to be focused in the critical regime. Following the application of a magnetic field, the peak resistivity decreases in amplitude while the peak temperature increases, a behavior quite similar to that of CMR manganites; here this behavior has been interpreted on the basis of exchange coupled scattering of carriers by magnetic spin fluctuations [27, 62].

The maximum in ρ(T, 0) yields an MIT temperature of T_{MI} = 76 K, In the metallic regime ($T < T_{MI}$), the resistivity can be characterized by the power-law combination: $\rho(T,H) = \rho_0 + \rho_1 T^2 + \rho_2 T^4$, which can be dominated by either electron-electron ($\rho_1 T^2$)

or electron-phonon scattering ($\rho_2 T^4$) [144]; ρ_0 is the residual resistivity arising from impurity scattering. The presence of a resistivity minima near 10 K, evident in Figure 5.8 (b), is intriguing, and was initially explained on the basis of the Kondo effect, which produces a ln(T) increase in the low-temperature resistivity [145, 146]. While the present single crystal sample displays an anisotropy in its low-temperature transport behavior not unlike that reported in other Kondo-like metallic alloys [147], its evolution with field is inconsistent with conventional Kondo behavior. Its origin has been discussed in terms of strong electron-electron interactions [148], reminiscent of the behavior of amorphous alloys [149].

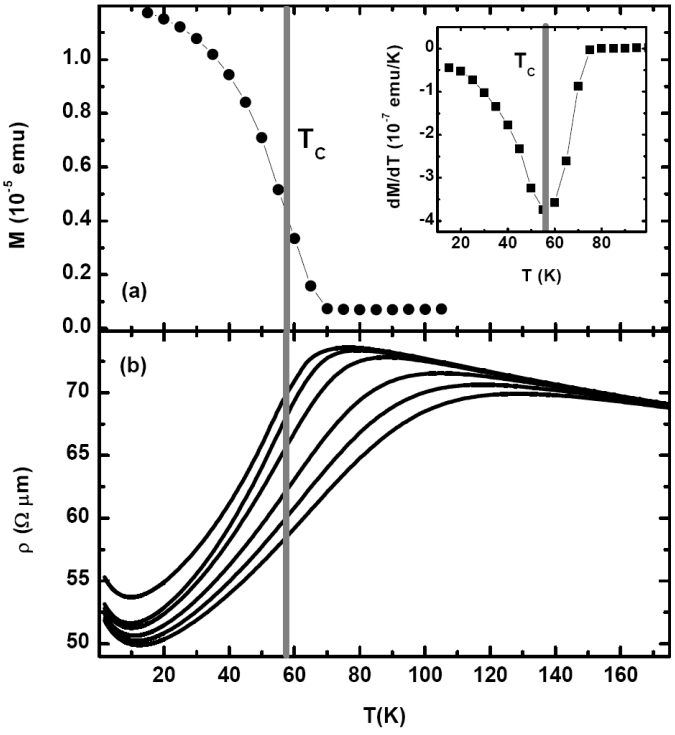

Figure 5.8 *Temperature dependent magnetization and resistivity of $Ga_{0.98}Mn_{0.02}As$. (a) M(T) measured at 50 Oe in a SQUID magnetometer. (b) ρ(T) measured at magnetic fields 0, 2.5, 10, 30, 50, 70 kOe.*

A summary of these magneto-transport data (as a function of field in various static temperatures) in the critical regime is presented in Figures 5.9 (a) and (b). The variation of ρ_{xy} with temperature and field is strongly suggestive of a link with the magnetization, and indeed, far above the ordering temperature (and hence not reproduced here), it exhibits the same linear dependence on field as is well established for M in a wide range of system which also exhibit magnetic ordering. As discussed above in relation to the $Fe_{0.8}Co_{0.2}Si$ system, the first issue that needs to be addressed in evaluating the anomalous Hall conductivity σ_{xy}^{A} as accurately as possible is the accurate determination of the contribution arising from the ordinary Hall conductivity $\sigma_{xy}^{O} = \frac{R_0 H}{\rho_{xx}^2}$.

This was done using the technique advocated in the previous section [69], i.e., the intercept of $d\rho_{xy}/dH = R_0$ extrapolated from high fields (50 kOe < H < 70 kOe) where the susceptibility is expected to vanish. This yields a weakly temperature dependent hole density n ≈ (5.0 ± 0.3) × 10^{20} cm^{-3}, consistent with previous estimates [6]; this result also indicates that in this system the anomalous Hall term is dominant over the entire temperature range studied. Figure 5.9 (c) displays the resulting estimates for $\sigma_{xy}^{A} = \sigma_{xy} - \sigma_{xy}^{O}$.

These latter results were again used in the modification of conventional critical analysis [43] discussed in the preceding section using the direct proportionality between σ_{xy}^{A} and M established above. As in $Fe_{0.8}Co_{0.2}Si$, such proportionality again enables the usual Arrott-Noakes/scaling equation of state to be expressed in terms of the anomalous

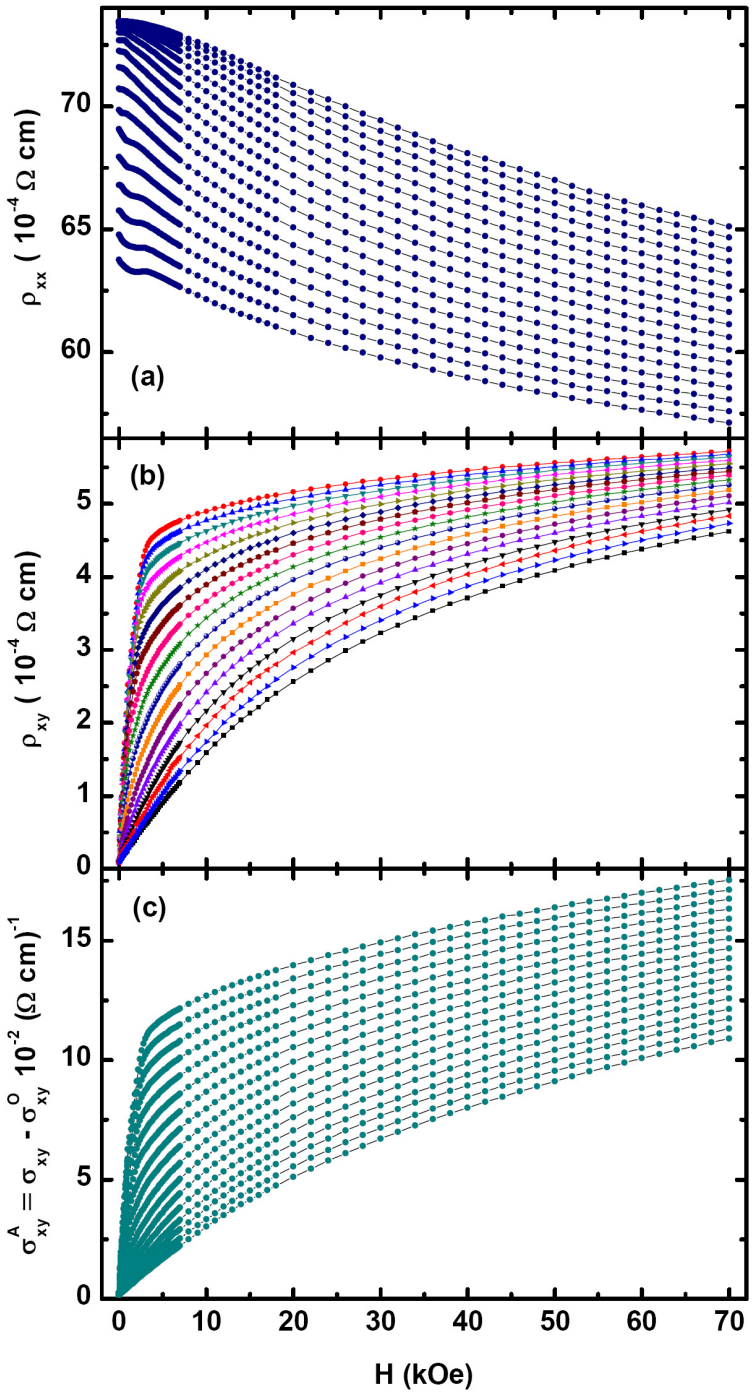

Figure 5.9 *Field dependent magneto-transport measurements on $Ga_{0.98}Mn_{0.02}As$. (a) Hall resistivity ρ_{xy} and (b) longitudinal resistivity ρ_{xx} measured at various fixed temperatures (46 K − 78 K in 2 K steps) in the fields up to 70 kOe. Insert; the corresponding zero field, temperature dependent ρ_{xx}. (c) The corresponding anomalous Hall conductivity σ_{xy}^{A} derived from ρ_{xy} and ρ_{xx} as discussed in the text.*

Hall conductivity σ_{xy}^{A} equation (2-44), viz., $\left(\frac{\sigma_{xy}^{A}}{\sigma_1}\right)^{1/\beta} = \frac{T_C - T}{T_C} + \left(\frac{H}{\sigma_{xy}^{A}}\right)^{1/\gamma}$. The critical exponents appropriate for the corresponding transition are those which linearize the anomalous Hall conductivity – field data plotted in the above form. As Figure 5.10 (a) shows, "conventional" Arrott plots of these data, i.e., H/σ_{xy}^{A} versus $(\sigma_{xy}^{A})^2$, are indeed linear, a result demonstrating the applicability of Mean-Field model exponents ($\beta = 0.5$, $\delta = 3$, $\gamma = 1$ [35]), with the estimate for the ordering temperature being $T_C = 61.5 \pm 0.5$ K (from the critical anomalous Hall conductivity $\sigma_{xy}^{A}(T_C)$; the quoted error in the ordering temperature arises from uncertainties in the absolute temperature, relative temperatures can be determined with much higher precision). This value for T_C confirms indirectly (through a comparison with T_C/x versus n (x being the Mn doping level) phase diagram [6]) that the nominal and actual compositions are very close.

The "spontaneous" anomalous Hall conductivity, $\sigma_{xy-Spon}^{A}$, is found from the intercepts of the linearized plots of Figure 5.10 (a) on the perpendicular axis, i.e., at H = 0. Those on the horizontal axis yield a quantity proportional to the (inverse) initial susceptibility $[1/\chi_i(T) = (\partial H/\partial M)_{H=0}]$. The isotherm that passes through the origin (the "critical" anomalous Hall conductivity isotherm, $\sigma_{xy}^{A}(T_C)$), yields the ordering temperature T_C. Self-consistency is then achieved by applying equations (2-46) – (2-48) to the appropriate intercept values so estimated, and substituting the exponent values deduced from them back into equation (2-44); this process is repeated – with small adjustments to T_C (typically 0.1 K) – until the Arrott plots and the ensuing power-laws yield the same exponent values. The detailed confirmation of these exponent

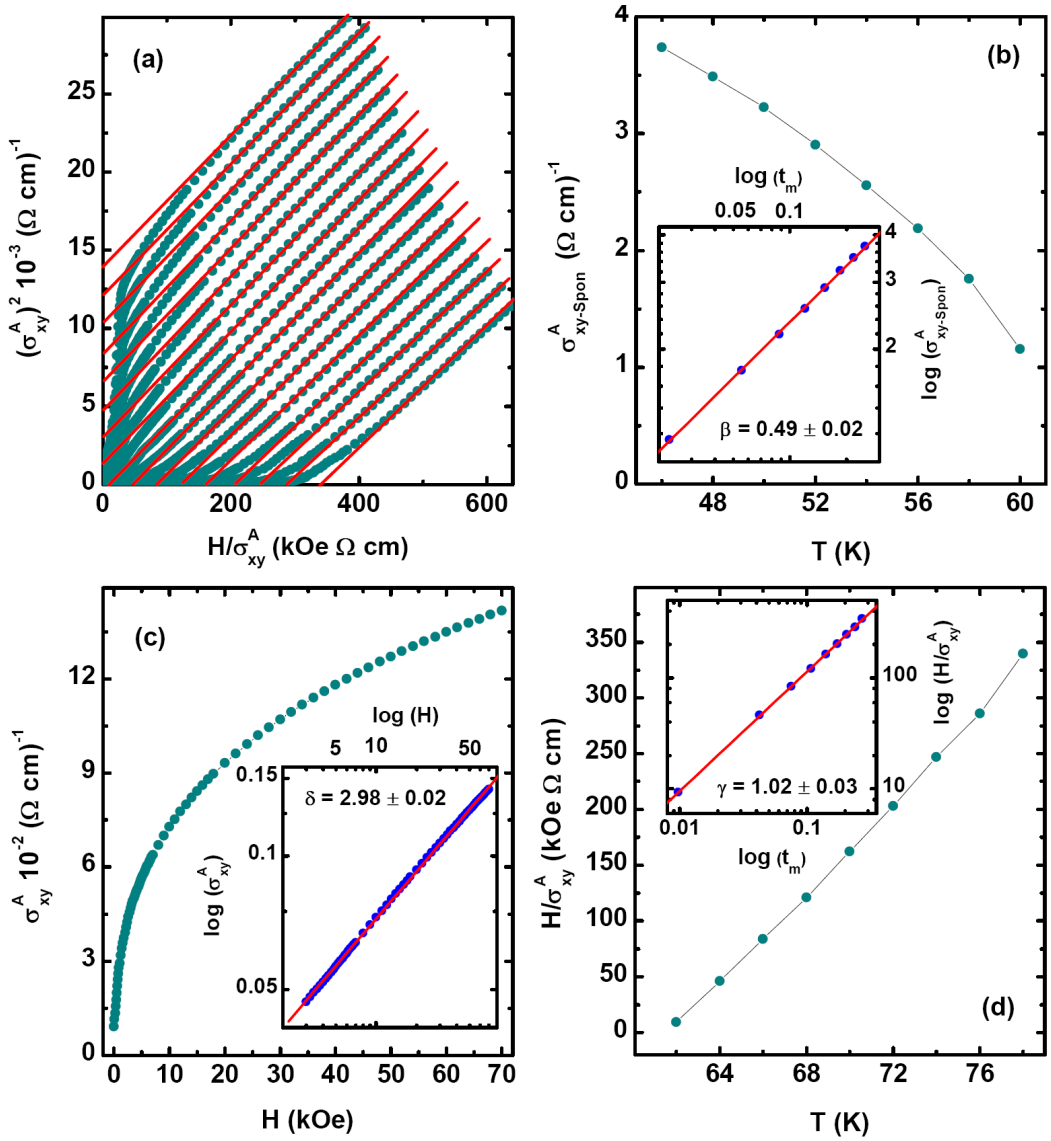

Figure 5.10 *Novel critical analysis based on the anomalous Hall conductivity* σ^A_{xy} *for* $Ga_{0.98}Mn_{0.02}As$. *(a) The "Arrott plot" equivalents –* H/σ^A_{xy} *vs.* $(\sigma^A_{xy})^2$; *the straight line passing through the origin yields the critical temperature* $T_C = 61.5 \pm 0.5$ *K. (b)* σ^A_{xy} *vs. H along the critical isotherm (*T_C*): insert; these same data replotted on a double-logarithmic scale, the slope of the resulting straight line yielding* $\delta = 2.98 \pm 0.02$. *(c) The "spontaneous" anomalous Hall conductivity* $\sigma^A_{xy-Spon}$ *plotted against temperature: insert;* $\sigma^A_{xy-Spon}$ *vs.* t_m *on a double-logarithmic scale, the slope of the straight line drawn yielding* $\beta = 0.49 \pm 0.02$. *(d)* H/σ^A_{xy} *plotted against temperature: insert;* H/σ^A_{xy} *vs.* t_m *on a double-logarithmic scale, the slope of the straight line drawn yields* $\gamma = 1.02 \pm 0.03$.

assignments are provided in Figures 5.10 (b) – (d), particularly their double-logarithmic inserts testing the power-law predictions and yielding $\beta = 0.49 \pm 0.02$, $\gamma = 1.02 \pm 0.03$ and the equation of state critical exponent $\delta = 2.98 \pm 0.02$ (for 2 kOe < H < 70 kOe).

These exponent estimates are consistent with Mean-Field model values, within experimental uncertainty, and thus satisfy the Widom relation $\gamma = \beta (\delta - 1)$ [35]. A final, comprehensive assessment of the applicability of Mean-Field exponents to the anomalous Hall conductivity (σ_{xy}^{A}) data estimates so obtained for $Ga_{0.98}Mn_{0.02}As$ is provided by Figure 5.11. This figure demonstrates unequivocally that the data in Figure 5.10 (a) can be scaled onto two branches, one for data below (F_-) and the other for data above T_C(F_+), using the choice of variables suggested by equation (2-45) and Mean-Field exponents; these branches merge as the temperature approaches T_C (i.e., t_m approaching zero).

Such a result has interesting consequences. Whereas the critical behavior for localized spins coupled via short-ranged (Heisenberg) interactions in insulators is determined by the space/lattice dimensionality, d, and the order parameter/spin dimensionality, k, the corresponding behavior in metallic systems is markedly different. For the latter, renormalization group calculations [150] predict that for long-ranged attractive spin-spin interactions (J(r)) decaying with distance r as $J(r) \approx r^{-(d+k)}$, Mean-Field behavior occurs for $d/2 \leq k \leq 3/2$ (i.e., if, in three dimensions (d = 3), J(r) decreases with r more slowly than $r^{-4.5}$, then k = 1.5). In contrast, for k > 2 short-ranged critical behavior ensues, while in the intermediate regime, $d/2 \leq k \leq 2$, the critical

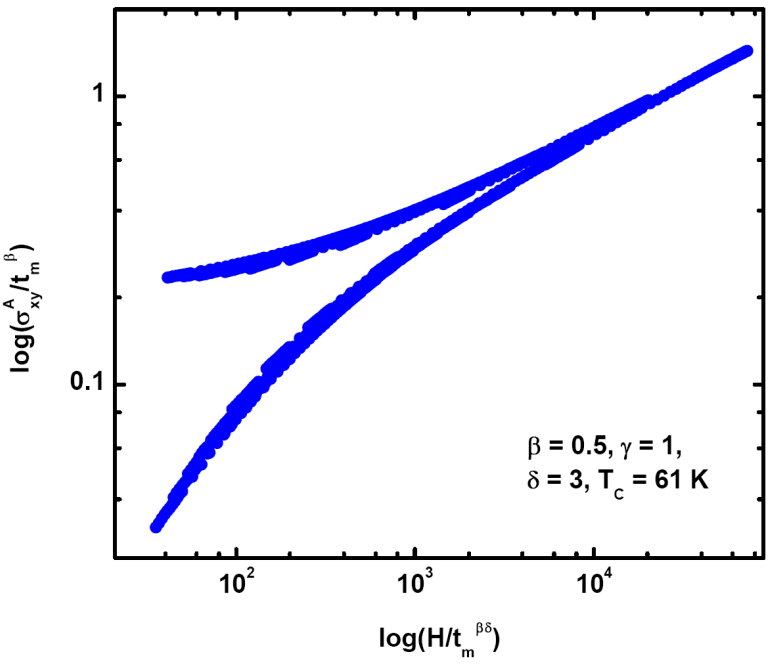

Figure 5.11 *Comprehensive scaling plot for* σ^A_{xy} *in* $Ga_{0.98}Mn_{0.02}As$. *The plot uses the critical exponents and* T_C *listed in this figure. The data collapse on this* $\log(\sigma^A_{xy}/t_m^{\beta})$ *vs.* $\log(H/t_m^{\beta\delta})$ *plot provides confirmation of the validity of the* T_C *and critical exponent(* γ, β, δ*) estimates. The upper branch corresponds to data below* T_C *and the lower branch to data above* T_C.

exponents depend upon the value for k. The immediate inference drawn from the present data is that, in $Ga_{0.98}Mn_{0.02}As$, $(d + k) < 4.5$.

That this result may not hold at all Mn doping levels is not surprising; in particular, at higher doping levels, at which the hole-mediated exchange is weaker, and the probability of near-neighbor AFM Super Exchange Mn-Mn interactions is increased [6]. Thus Mean-Field exponents do not linearize the equivalent plots (indirectly confirmed by the suppression of T_C due to the correlated Mn-moment fluctuations based on the Mean-Field model), i.e., the so-called Arrott plots at x = 0.053 [27] and x = 0.06 [141],

unlike those displayed here, exhibit curvature, indicating a cross-over to a different universality class.

While a more extensive series of experiments covering a wider range of Mn doping would enable such cross-over effects to be investigated in more detail, the importance of the present study is that it demonstrates: first, that accurate exponent values can be extracted from magneto-transport measurements (specifically the anomalous Hall conductivity), admitting its use in a range of other situations, including, as demonstrated here, in low-dimensional spintronic devices where conventional techniques are compromised; and second, in the case of low Mn doped metallic $Ga_{0.98}Mn_{0.02}As$, these exponents are Mean-Field [151], thus validating directly the frequently adopted theoretical approach to ferromagnetic (III, Mn)V semiconductors which predicts the intrinsic origin of the occurrence of AHE in this compound.

Chapter 6

Conclusions and Future Work

In summary, this thesis focuses principally on the magnetic and transport properties of doped CMR manganites and magnetic semiconductors, investigating specifically magnetic phase transitions and related phenomena. A summary of the results of these investigations, followed by proposals for the future work, are presented below.

6.1 Summary and Conclusions

6.1.1 Doped Manganites

The purpose of the present study was to investigate the influence of various doping levels (x) and different doping elements (specifically Pr, Ca and Ba) on the transition from paramagnetism to ferromagnetism, and the attendant metal-insulator phase change, in manganites. Specifically, magnetic and transport measurements on four manganites systems have been performed, namely, $La_{1-x}Ca_xMnO_3$ ($0.18 \leq x \leq 0.27$), $La_{1-x}Ba_xMnO_3$ ($x \leq 0.33$), $(La_{1-y}Pr_y)_{0.7}Ca_{0.3}Mn^{16/18}O_3$ ($y \leq 0.85$), and $Pr_{1-x}Ca_xMnO_3$ ($x = 0.27, 0.29$).

In $La_{1-x}Ca_xMnO_3$ ($0.18 \leq x \leq 0.27$) [15, 19, 55], temperature dependent (magneto)resistance measurements indicate that the compositionally modulated MIT

lies between $0.19 \leq x_c \leq 0.20$ in the single crystal series studied, consistent with numerously reported values in the range $0.18 \leq x_c \leq 0.22$. Magnetization and ac susceptibility measurements were also performed across this MIT in the same single crystal specimens. Subsequent comparisons between these transport and magnetic data enabled several important conclusions to be drawn.

First, regarding the correlation between a Griffiths-like phase and CMR, the experimental data in the vicinity of this MIT boundary indicate that while the x = 0.19 sample exhibits features consistent with the presence of such a phase, CMR is absent; in contrast, data on the x = 0.20 single crystal show no Griffiths-like phase features, but a CMR is present; at x = 0.21, however, both Griffiths-like phase features *and* CMR are observed. Such data enable the following specific conclusions to be drawn for the $La_{1-x}Ca_xMnO_3$ system: viz., the presence of a Griffiths-like phase does not guarantee CMR, nor are the appearance of such features a prerequisite for CMR [18-20].

Second, on the universality class of magnetic phase transition in the same system, the present investigation reveals that whereas continuous magnetic transitions occur for $0.18 \leq x \leq 0.25$, at x = 0.27, features consistent with the simultaneous appearance of both a second order (continuous) and a first order (discontinuous) transition are present. The universality class of these continuous transitions belongs to that of nearest neighbor 3-D Heisenberg model only for $x \leq 0.20$. Beyond x = 0.20, complications due to the emergence of a Griffiths-like phase occur, specifically, the critical exponents these samples do not fall into the universality class of any known model.

Third, the evolution of the MIT with composition supports the assertion that the dominant mechanism underlying ferromagnetism across the MIT boundary changes from FM Super Exchange stabilized by orbital ordering in the insulating phase to Double Exchange in the orbitally disordered metallic regime [15].

In $La_{1-x}Ba_xMnO_3$ ($x \leq 0.33$) [54, 59], detailed magnetic and transport measurements yield critical exponents $\delta = 5.5 \pm 0.3$, $\gamma = 1.41 \pm 0.02$, $\beta = 0.35 \pm 0.04$, with $T_C = 310 \pm 0.5$ K, complemented by the coexistence of a Griffiths-like phase and CMR. The latter, used in combination with previous data, enables a temperature-doping level phase diagram to be constructed delineating specifically the occurrence of a Griffiths-like phase, and facilitating comparisons with the random bond Ising and the $\pm J$ models. Finally, a compilation of various structurally based parameters for both these Ca and Ba-doped systems is presented, and this reveals that not a single such parameter reflects the detailed variations evident in such phase diagrams. The specific disorder from which a Griffiths-like phase originates in these compounds thus remains unidentified, thus requiring further study.

In contrast to the systems discussed above, in $(La_{1-y}Pr_y)_{0.7}Ca_{0.3}Mn^{16/18}O_3$ ($y \leq 0.85$) [60], the correlation between phase competition and nucleation of a Griffiths-like phase has been discussed in combination with previously acquired neutron diffraction data [82]. Using the latter, it was possible to demonstrate that an emergence of a Griffiths-like phase correlates directly with the relative volume fractions of the phase separated AFM and FM components, even when the recently estimated Double

Exchange linked percolation threshold for manganites is exceeded [98]. In this system, a Griffiths-like phase emerges when the relative volume fraction of the FM component is larger than 50%, i.e., when $y \leq y_c = 0.85$. Correspondingly, when $y > y_c$, no Griffiths-like phase is nucleated as the accompanying AFM volume fraction is larger than 50%. In addition, the influence of the electron-phonon coupling on the Griffiths-like phase can also be seen through oxygen isotope effects. Various structural parameters are again shown to display no direct link to Griffiths-like phase behavior in this system.

Finally, in $Pr_{1-x}Ca_xMnO_3$ (x = 0.27, 0.29) [118], the coexistence of ferromagnetism and insulating behavior was investigated. Here magnetic data yield critical exponent estimates consistent with predictions for the nearest-neighbor 3-D Heisenberg model, as in $La_{1-x}Ca_xMnO_3$ for $x \leq 0.19$ [15, 55]; such a result suggests – albeit indirectly, as the corresponding neutron data is currently lacking – that the origin of ferromagnetism in these insulating manganites is again FM Super Exchange, as here Double Exchange cannot be the dominant interaction as metallicity is manifestly absent.

6.1.2 Magnetic Semiconductors

In $Fe_{0.8}Co_{0.2}Si$ and $Ga_{0.98}Mn_{0.02}As$, the relation between magnetization and conductivity has been the subject of ongoing discussion [28, 30], reflecting the broader debate regarding the correlation between magnetism and transport in magnetic materials.

The present study, on the two systems mentioned above, contribute to this debate by demonstrating that the universality class of the magnetic transition in them can be directly established from the anomalous Hall conductivity. The latter result could prove pivotal in improving our current understanding of magnetism, transport, and their correlation in magnetic metals/semiconductors, particularly for the low-dimensional spintronic devices with an extreme weak magnetic response.

In particular, in bulk polycrystalline $Fe_{0.8}Co_{0.2}Si$, this novel scaling between the AHE and magnetization enables the quadratic dependence of the anomalous Hall coefficient R_S on longitudinal resistivity ρ_{xx} ($R_S \propto \rho_{xx}^2$) to be demonstrated conclusively. Furthermore, it shows that the *anomalous* Hall conductivity is the intrinsic parameter linked linearly with the magnetization, rather than the Hall/longitudinal resistivity/conductivity. As a corollary, the universality class can then be established from magneto-transport measurements, specifically, from the anomalous Hall conductivity. The resulting 3-D Heisenberg universality class assignment is confirmed by the analysis of detailed magnetization and ac susceptibility data.

In an epitaxial (metallic) $Ga_{0.98}Mn_{0.02}As$ microstructure [151], using the theoretical prediction (based on a Mean-field approach) of $R_S \propto \rho_{xx}^2$, the magnetization has been extracted indirectly from the AHE. Subsequent analysis yields magnetic critical exponents of $\beta = 0.49 \pm 0.02$, $\gamma = 1.02 \pm 0.03$, $\delta = 2.98 \pm 0.02$, with $T_C = 61.5 \pm 0.5$ K, consistent with the Mean-Field model predictions. *Direct* support for the applicability of the latter had previously been lacking. This in turn, validates the frequently adopted

theoretical approach, specifically, the intrinsic origin of the AHE in ferromagnetic (III, Mn)V semiconductors.

6.2 Future Work

Although several decades of extensive effort have been devoted to CMR manganites and magnetic semiconductors, many open questions remain [152], the answers to which require further study.

6.2.1 Doped Manganites

I: The Physical Origin of Griffiths-like Phase in $La_{1-x}Ca_xMnO_3$ and $La_{1-x}Ba_xMnO_3$.

The nucleation of a Griffiths-like phase in $(La_{1-y}Pr_y)_{0.7}Ca_{0.3}Mn^{16/18}O_3$ ($y \leq 0.85$) has been successfully discussed using the idea of phase competition between the phase separated AFM and FM components [60], a result that draws heavily on neutron scattering data. In contrast, the underlying reasons for the occurrence of a Griffiths-like phase in $La_{1-x}Ca_xMnO_3$ and $La_{1-x}Ba_xMnO_3$ systems are still unclear. What has been established by the present work on these latter systems is that the "disorder" underlying the emergence of a Griffiths-like phase in these two systems is not linked in any direct way to structural disorder (as represented, for example, by the A-site radius and/or its variance). Such a phase most likely results from inhomogeneous competing/phase

separated states in these two systems. However, the current lack of definitive data – particularly those resulting from the application of detailed imaging techniques – makes it difficult to address this issue in a self-consistent manner.

II: On the Random Transition Temperature, T_C^{Rand}, the Griffiths Temperature, T_G, and the 'Exponent' λ.

Experimentally, the Griffiths temperature T_G is often estimated as the onset temperature of deviations in the inverse susceptibility from the conventional CW law, viz., above T_G the system is purely PM while below T_G a downturn consistent with the formation of large clusters/correlated regions occurs. Following this prescription, the inverse susceptibility above T_G obeys a CW law ($\chi^{-1} \propto \frac{1}{T - T_C}$) which, correspondingly, yields the exponent $\lambda = 0$ ($T > T_G$) when T_C^{Rand} is correctly identified. However, recent experiments in the temperature range $T_G < T < 700$ K [20, 96] indicate that such a criterion can be problematic; in the $La_{1-x}Ca_xMnO_3$ system above T_G, the linear behavior expected from a simple CW law in this PM regime is *not* observed. Instead, the inverse susceptibility exhibits curvature; the latter, *possibly* arising from polaron formation [20, 96], results in the exponent λ not necessarily being equal to zero above T_G. While the origin of this curvature needs to be confirmed, its presence underlies the reluctance to initiate a systematic discussion of exponent λ in this thesis.

III: Imaging Investigation on the Manganites.

While the strong correlation between charge, spin, orbital and vibrational degree of freedoms is an important component in understanding CMR, increasing attention has

been focused on the percolative nature of inhomogeneous competing states [3, 4, 21-23]. Theories based on such states indeed seem to capture the essential physics of CMR. In this context, a series of imaging studies might be contemplated in an attempt to unravel the unconventional temperature/field response of manganites, in general, and the origin and evolution of a Griffiths-like phase in particular. Specifically, (1) Magnetic Force Microscopy, with its high spatial resolution, might be used to image this magnetically inhomogeneous competitive state, in both spatial and temporal modes. Such imaging could likely track the effects of the itinerancy of e_g electrons in alternating the valence states of adjacent Mn^{3+} and Mn^{4+} ions. (2) Regarding the origin of a Griffiths-like phase, the application of the same technique might yield direct evidence supporting the existence of so-called correlated magnetic clusters/volumes below T_G, and, further, could lead to a detailed study of their evolution with field and temperature. (3) Spin polarized Scanning Tunneling Microscopy has also been applied to manganites, and has been demonstrated to be sensitive to electronic phase separated states (phase separated regions with high/low resistances) [23]. In this context, the application of both Magnetic Force Microscopy and Scanning Tunneling Microscopy in the same system could resolve issues surrounding the magnetic and electronic nature of these phase separated/correlated states. (4) Tunneling Electron Microscopy experiments have also been performed on manganites, however, such an imaging technique only appears to work with *structural* phase changes (not magnetic phase changes) at higher doping levels, for example, in the charge ordering phase with superlattice reflections [153].

IV: Anomalous Hall Effect in $La_{1-x}Ca_xMnO_3$ (x = 0.18 and 0.20).

The motivation for choosing these two samples for further study is two fold: (1) the magnetic critical behavior can be characterized using 3-D Heisenberg model exponents, with essentially no complications arising from the presence of a Griffiths-like phase; (2) x = 0.18 and 0.20 lie on the either sides of the MIT boundary; Hall effect measurements could, in principle, yield some insights into the different origins of ferromagnetism in these two samples (a project planned for the near future).

In canonical CMR manganites, the hopping of e_g electrons in, for example, $La_{0.8}Ca_{0.2}MnO_3$, plays a fundamental role in the conduction process, leading to the applicability of the spin-dependent DE model. The purpose of performing Hall measurements would be to try to ascertain whether the Hall coefficients (R_0 and R_S) exhibit any kind of critical behavior across the coincidental FM-PM/metal-insulator phase transition regimes, which, in turn might reflect the underlying role of DE in CMR.

6.2.2 Magnetic Semiconductors

I: Origin of the Positive Magnetoresistance in $Fe_{1-x}Co_xSi$

The positive MR in $Fe_{1-x}Co_xSi$ was explained initially using the idea of quantum interference, rather than simple scattering. This was based on the fact that $Fe_{1-x}Co_xSi$ is a highly disordered *ferromagnet* with low carrier density, with the same electrons being

responsible for both electric conduction and magnetic behavior [28]. However, this was later challenged using the concept of Zeeman splitting of exchange split spin up/down bands [30]. The origin of the positive MR in this compound *might* elucidated through substituting the non-magnetic elements Si by Al, Ge, Ga etc., keeping both the atomic radius of the non-magnetic component and the fraction of magnetic elements constant. For example, by changing the non-magnetic doping level, $0 \leq y \leq 1$, in $Fe_{0.8}Co_{0.2}(Si_{1-y}Al_y)$, should the MR change from positive to negative, some possible sources yielding a positive MR could be ruled out. In addition, $Fe_{1-x}Co_xSi$ exhibits a large AHE, and modulating the non-magnetic element substitution level might also yield useful information on the origin of this large AHE.

II: Evolution of the Universality Class in $(Ga_{1-x}Mn_x)As$.

Although Mean-Field behavior has been reported above at $x = 0.02$, this result may not hold at all Mn doping levels. At higher doping levels, the hole-mediated exchange coupling is weaker (due to modification of the RKKY mechanism [6, 27]), and the probability of near-neighbor Mn-Mn AFM Super Exchange interactions is increased. Such effects suggest a more extensive series of experiments covering a wider range of Mn doping levels (from the insulating ($x < 0.02$) to the metallic regime ($0.02 < x < 0.10$)), which might enable cross-over effects to be investigated via changes in the asymptotic critical behavior through measurements of the magnetization in *bulk* samples.

III: Evolution of the Anomalous Hall Coefficients, R_S/R_0, in $(Ga_{1-x}Mn_x)As$.

Using a similar approach to that proposed for $Fe_{0.8}Co_{0.2}Si$, future experiments focusing on the AHE could be performed on a series of $(Ga_{1-x}Mn_x)As$ specimens. First, the scaling between AHE and magnetization could be established, focusing on the evolution of the anomalous Hall coefficient R_S as a function of both temperature and Mn doping level. Second, the critical behavior across the FM-PM/Metal-Insulator transition in the $(Ga_{1-x}Mn_x)As$ system might be investigated, focusing particularly on the possibility of observing critical behavior in the temperature dependence of the carrier density n(T). Such a critical response might provide evidence indicating the importance of the role played by carrier-mediated ferromagnetism in $(Ga_{1-x}Mn_x)As$.

Chapter 7 Bibliography

[1]. J. Orenstein, A. J. Millis, *Science*, **288**, 468 (2000).

[2]. R. von Helmolt, J. Wecker, B. Holzapfel, L. Schultz, and K. Samwer, Phys. Rev. Lett. **71**, 2331 (1993); S. Jin, T. H. Tiefel, M. McCormack, R. A. Fastnacht, R. Ramesh, and L. H. Chen, *Science*, **264**, 413 (1994).

[3]. A. Moreo, S. Yunoki, and E. Dagotto, *Science*, **283**, 2034 (1999); E. Dagotto, *Phase Separation and Colossal Magnetoresistance* (Springer, Berlin, 2002); E. Dagotto, *Science*, **309**, 257 (2005).

[4]. *Colossal Magneto-resistive Oxides*, edited by Y. Tokura (Gordon and Breach Science Publishers, 2000); Y. Tokura, N. Nagaosa, *Science*, **288**, 462 (2000); J. M. D. Coey, M. Viret, and S. V. Molnar, Adv. Phys. **48**, 167 (1999).

[5]. W. Eerenstein, N. D. Mathur, and J. F. Scott, *Nature,* **442**, 759 (2006).

[6]. T. Jungwirth, J. Sinova, J. Masek, J. Kucera, and A. H. MacDonald, Rev. Mod. Phys. **78**, 809 (2006).

[7]. A. B. Pippard, *Magnetoresistance in Metals* (Cambridge University Press, Cambridge, 1989).

[8]. G. A. Prinz, *Scinece*, **282**, 1660 (1998).

[9]. M. N. Baibich, J. M. Broto, A. Fert, F. Nguyen Van Dau, F. Petroff, P. Etienne, G. Creuzet, A. Friederich, and J. Chazelas, Phys. Rev. Lett. **61**, 2472 (1988).

[10]. http://nobelprize.org/nobel_prizes/physics/.

[11]. J. G. Bednorz and K. A. Müller, Zeitschrift für Physik B: Condensed Matter. **64**, 189 (1986).

[12]. C. Zener, Phys. Rev. **81**, 440 (1951).

[13]. P. W. Anderson, Phys. Rev. **79**, 350 (1950); P. W. Anderson and H. Hasegawa, Phys. Rev. **100**, 675 (1955); P. G. de Gennes, Phys. Rev. **118**, 141 (1960).

[14]. A. Millis, P. Littlewood, and B. Shraiman, Phys. Rev. Lett. **74**, 5144 (1995).

[15]. W. Jiang, X. Zhou, G. Williams, Y. Mukovskii, and R. Privezentsev, Phys. Rev. B **79**, 214433 (2009).

[16]. A. J. Millis, *Nature*, **392**, 147 (1998).

[17]. A. Moreo, M. Mayr, A. Feiguin, S. Yunoki, and E. Dagotto, Phys. Rev. Lett. **84**, 5568 (2000); M. Mayr, A. Moreo, J. A. Vergés, J. Arispe, A. Feiguin, and E. Dagotto, Phys. Rev. Lett. **86**, 135 (2001).

[18]. M. B. Salamon, P. Lin, and S. H. Chun, Phys. Rev. Lett. **88**, 197203 (2002); M. B. Salamon and S. H. Chun, Phys. Rev. B **68**, 014411 (2003).

[19]. W. Jiang, X. Zhou, G. Williams, Y. Mukovskii, and K. Glazyrin, Phys. Rev. Lett. **99**, 177203 (2007).

[20]. J. Souza, J. Neumeier, and Y. Yu, Phys. Rev. B **78**, 014436 (2008).

[21]. L. Zhang, C. Israel, A. Biswas, R. L. Greene, and Alex de Lozanne**,** *Science*, **298**, 5594 (2002).

[22]. M. Uehara, S. Mori, C. H. Chen, and S.W. Cheong, *Nature*, **399**, 560 (1999).

[23]. M Fäth, S. Freisem, A. A. Menovsky, Y. Tomioka, J. Aarts, and J. A. Mydosh, *Science*, **285**, 5433 (1999).

[24]. G. M. Zhao, K. Conder, H. Keller, and K. A. Müller, *Nature*, **381**, 676 (1996).

[25]. S. Wolf, D. Awschalom, R. A. Buhrman, J. M. Daughton, S. von Molnár, M. L. Roukes, A. Y. Chtchelkanova, and D. M. Treger, *Science,* **294**, 1488 (2001).

[26]. H. Ohno, D. Chiba, F. Matsukura, T. Omiya, E. Abe, T. Dietl, Y. Ohno, and K. Otan, *Nature,* **408**, 944 (2000).

[27]. H. Ohno, *Science,* **281**, 951 (1998); F. Matsukura, H. Ohno, A. Shen, and Y. Sugawara, Phys. Rev. B **57**, R2037 (1998).

[28]. N. Manyala, Y. Sidis, J. F. DiTusa, G. Aeppli, D. P. Young, and Z. Fisk, *Nature,* **404**, 581 (2000).

[29]. V. Jaccarino, G. Wertheim, J. Wernick, L. Walker, and S. Arajs, Phys. Rev. **160**, 476 (1967); M. Chernikov, L. Degiorgi, E. Felder, S. Paschen, A. D. Bianchi, H. R. Ott, J. L. Sarrao, Z. Fisk, and D. Mandrus, Phys. Rev. B **56**, 1366 (1997);

A.-M. Racu, D. Menzel, J. Schoenes, and K. Doll, Phys. Rev. B **76**, 115103 (2007).

[30]. Y. Onose, N. Takeshita, C. Terakura, H. Takagi, and Y**.** Tokura, Phys. Rev. B **72**, 224431 (2005).

[31]. A. H. MacDonald, P. Schiffer, and N. Samarth, *Nature Materials,* **4**, 195 (2005).

[32]. http://www.ohno.riec.tohoku.ac.jp/.

[33]. J. König, H. Lin, and A. H. MacDonald, Phys. Rev. Lett. **84**, 5628 (2000).

[34]. F. Maccherozzi, M. Sperl, G. Panaccione, J. Minár, S. Polesya, H. Ebert, U. Wurstbauer, M. Hochstrasser, G. Rossi, G. Woltersdorf, W. Wegscheider, and C. H. Back, Phys. Rev. Lett. **101**, 267202 (2008).

[35]. H. E. Stanley, *Introduction to Phase Transitions and Critical Phenomena* (Clarendon, Oxford, 1971).

[36]. K. Huang, *Statistical Mechanics*, (John Wiley & Sons, INC., 1963).

[37]. A. Arrott, Phys. Rev. **108**, 1394 (1957).

[38]. S. K. Banerhee, Phys. Letter. **12**, 16 (1964); H. Kuwahara, Y. Tomioka, A. Asamitsu, Y. Moritomo, Y. Tokura, *Science*, **270**, 961 (1995); J. A. Souza, Y-K. Yu, J. J. Neumeier, H. Terashita, and R. F. Jardim, Phys. Rev. Lett. **94** 207209 (2005).

[39]. V. K. Pecharsky and K. A. Gschneidner, Jr., Phys. Rev. Lett. **78**, 4494 (1997).

[40]. C. Kittel, *Introduction to Solid State Physics* (Wiley, New York, 1976) 2nd Edition.

[41]. E. A. Yelland, S. J. C. Yates, O. Taylor, A. Griffiths, S. M. Hayden, and A. Carrington, Phys. Rev. B **72**, 184436 (2005).

[42]. L. Kadanoff, W. Gotze, D. Hamblen, R. Hecht, E. Lewis, V. V. Palciauskas, M. Rayl, J. Swift, D. Aspnes, and J. W. Kane, Rev. Mod. Phys. **39**, 395 (1967).

[43]. A. Arrott and J. E. Noakes, Phys. Rev. Lett. **19**, 786 (1967).

[44]. B. Widom, J. Chem. Phys. **43**, 3892 (1965).

[45]. C. Domb and D. L. Hunter, Proc. Roy. Soc. **86**, 1147 (1965).

[46]. G. Williams, J. Alloys. Comp. **326**, 36 (2001).

[47]. J. H. Zhao, H. P. Kunkel, X. Z. Zhou, G. Williams, and M. A. Subramanian, Phys. Rev. Lett. **83**, 219 (1999).

[48]. W. Li, H. P. Kunkel, X. Zhou, G. Williams, Y. Mukovskii, and D. Shulyatev, Phys. Rev. B **75**, 012406 (2007).

[49]. N. W. Ashcroft and N. D. Mermin, *Solid State Physics* (Holt, Rinehart and Winton, 1976).

[50]. P. P. Craig, W. I. Goldburg, T. A. Kitchens, and J. I. Budnick, Phys. Rev. Lett. **19**, 1334 (1967).

[51]. M. Campostrini, M. Hasenbusch, A. Pelissetto, P. Rossi, and E. Vicari, Phys. Rev. B **65**, 144520 (2002).

[52]. M. Campostrini, M. Hasenbusch, P. Rossi, and E. Vicari, Phys. Rev. E **60**, 3526 (1999).

[53]. M. Campostrini, M. Hasenbusch, A. Pelissetto, P. Rossi, and E. Vicari, Phys. Rev. B **63**, 214503 (2002).

[54]. W. Jiang, X. Zhou, G. Williams, Y. Mukovskii, and K. Glazyrin, Phys. Rev. B **77**, 064424 (2008).

[55]. W. Jiang, X. Zhou, G. Williams, Y. Mukovskii, and R. Privezentsev J. Phys.: Condens. Matter. **21,** 415603 (2009).

[56]. R. B. Griffiths, Phys. Rev. Lett **23**, 17 (1969); A. J. Bray, Phys. Rev. Lett. **59**, 586 (1987).

[57]. A. Castro Neto, G. Castilla, and B. Jones, Phys. Rev. Lett. **81**, 3531 (1998).

[58]. C. Magen, P. Algarabel, L. Morellon, J. P. Araújo, C. Ritter, M. Ibarra, A. Pereira, and J. Sousa, Phys. Rev. Lett. **96**, 167201 (2006).

[59]. W. Jiang, X. Zhou, G. Williams, Y. Mukovskii, and K. Glazyrin, Phys. Rev. B **76**, 092404 (2007).

[60]. W. Jiang, X. Zhou, and G. Williams, Europhys. Lett. **84**, 47009 (2008).

[61]. C. Jin, J. Zhou, J. Goodenough, Q. Liu, J. Zhao, L. Yang, Y. Yu, R. Yu, T.

Katsura, A. Shatskiy, and E. Ito, Proc. Natl. Acad. Sci. **105**, 7115 (2008).

[62]. V. Novak, K. Olejnik, J. Wunderlich, M. Cukr, K. Vyborny, A. Rushforth, K. Edmonds, R. Campion, B. Gallagher, J. Sinova, and T. Jungwirth. Phys. Rev. Lett. **101**, 077201 (2008).

[63]. M. E. Fisher and L. S. Langer, Phys. Rev. Lett. **20**, 665 (1968); F. C. Zumateg and R. D. Parks, Phys. Rev. Lett. **24**, 520 (1970); G. A. Tomas, A. B. Giray, and R. D. Parks, Phys. Rev. Lett. **31**, 241 (1973).

[64]. A. H. Morrish, *The Principle Physics of Magnetism* (Robert E. Krieger Publishing Company, Inc., New York, 1980).

[65]. S. Chun, M. Salamon, Y. Lyanda-Geller, P. Goldbart, and P. Han, Phys. Rev. Lett. **84**, 757 (2000); M. Salamon and M. Jaime, Rev. Mod. Phys. **73**, 583 (2001).

[66]. E. H. Hall, Am. Journ. Math. **2**, 287 (1879); E. H. Hall, Am. Journ. Sci. **3**, 161 (1880); E. H. Hall, Phil. Mag. 5, 200 (1981).

[67]. T. Lyman, Proc. Natl. Acad. Sci. **74**, 126 (1940).

[68]. Y. Pu, D. Chiba, F. Matsukura, H. Ohno, and J. Shi. Phys. Rev. Lett. **101**, 117208 (2008); S. Onoda, N. Sugimoto, and N. Nagaosa. Phys. Rev. Lett. **97**, 126602 (2006); T. Miyasato, N. Abe, T. Fujii, A. Asamitsu, S. Onoda, Y. Onose, N. Nagaosa, and Y. Tokura. Phys. Rev. Lett. **99**, 086602 (2007).

[69]. C. M. Hurd, *The Hall Effect in Metals and Alloys* (Plenum Press, 1972).

[70]. N. Nagaosa, J. Phys. Soc. Jpn. **75**, 042001 (2006); N. Nagaosa, J. Sinova, S. Onoda, A. Macdonald, and N. Ong. arXiv:0904.4154 (to be published in the Rev. Mod. Phys.).

[71]. M. Lee, Y. Onose, Y. Tokura, and N. P. Ong. Phys. Rev. B **75**, 172403 (2007).

[72]. N. Manyala, Y. Sidis, J. F. DiTusa , G. Aeppli , D. P. Young, and Z. Fisk, *Nature Materials,* **3**, 255 (2004).

[73]. J. M. Lavine, Phys. Rev. **123**, 1273 (1961).

[74]. J. Smit, Physica (Amsterdam) **21**, 877 (1955); **24**, 39 (1958).

[75]. L. Berger, Phys. Rev. B **2**, 4559 (1970).

[76]. R. Karplus and J. M. Luttinger, Phys. Rev. **95**, 1154 (1954); J. M. Luttinger, Phys. Rev. **112**, 739 (1958).

[77]. T. Jungwirth, Q. Niu, and A. MacDonald. Phys. Rev. Lett. **88**, 207208 (2002).

[78]. Quantum Design, *User Manual for PPMS Model 6000.*

[79]. http://www.qdusa.com/products/ppms.html.

[80]. D. Griffiths, *Introduction to Electrodynamics* (Addison-Wesley, 1998), 3rd Edition.

[81]. D. Shulyatev, S. Karabashev, A. Arsenov, and Y. Mukovskii, J. Cryst. Growth. **199**, 511 (1999).

[82]. V. Pomjakushin, D. V. Sheptyakov, K. Conder, E. V. Pomjakushina, and A. M. Balagurov, Phys. Rev. B **75**, 054410 (2007).

[83]. G. H. Jonker and J. H. Van Santen, Physica **16** 337 (1950) ; E. O. Wollan and W. C. Koehler, Phys. Rev. **100**, 545 (1955); S. Wang and C. W. Searle, Can. J. Phys. **49**, 387 (1970).

[84]. P. W. Anderson, Phys. Rev. **79**, 350 (1950); J. B. Goodenough, *Magnetism and the Chemical Bond* (R. E. Krieger, 1976); J. Kanamori, Journal of Physics and Chemistry of Solids, **10**, 87 (1959).

[85]. Y. Tokura and N. Nagaosa, *Science*, **288**, 462 (2000).

[86]. A. Urushibara, Y. Moritomo, T. Arima, A. Asamitsu G. Kido, and Y. Tokura, Phys. Rev. B **51**, 14103 (1995).

[87]. R. D. Shannon, Acta. Cryst. A**32**, 751 (1976).

[88]. J. M. Coey, M. Viret, L. Ranno, and K. Ounadjela, Phys. Rev. Lett. **75**, 3910 (1995).

[89]. J. B. Goodenough, Phys. Rev. **100**, 564 (1955).

[90]. P. G. Radaelli, D. E. Cox, M. Marezio, S -W. Cheong, P. E. Schiffer, and A. P. Ramirez, Phys. Rev. Lett. **75**, 4488 (1995).

[91]. J. M. D. Coey, *Nature*, **430**, 157 (2004).

[92]. P. Schiffer, A. P. Ramirez, W. Bao, and S-W. Cheong, Phys. Rev. Lett. **75**, 3336 (1995).

[93]. T. Okuda, Y. Tomioka, A. Asamitsu, and Y. Tokura, Phys. Rev. B **61**, 8009 (2000).

[94]. T. Holstein, Ann, Phys. (N. Y.) **8**, 325 (1959); **8**, 343 (1959); D. Emin and T. Holstein **53**, 439 (1969); B. I. Shklovskii and A. L. Efros, *Electronic Properties of Doped Semiconductors* (Springer, New York, 1984).

[95]. M. Ziese and C. Srinitiwarawong, Phys. Rev. B **58**, 11519 (1998); D. C. Worledge, L. Miéville, and T. H. Geballe, Phys. Rev. B **57**, 15267 (1998).

[96]. J. M. De Teresa, M. R. Ibarra, P. A. Algarabel, C. Ritter, C. Marquina, J. Blasco, J. García, A. Del Moral, and Z. Arnold, *Nature***, 386**, 256 (1997).

[97]. G. Biotteau, M. Hennion, F. Moussa, J. Rodríguez-Carvajal, L. Pinsard, A. Revcolevschi, Y. M. Mukovskii, and D. Shulyatev, Phys. Rev. B **64**, 104421 (2001).

[98]. J. Deisenhofer, Braak, H.-A. Krug von Nidda, J. Hemberger, R.M. Eremina, V.A. Ivanshin, A.M. Balbashov, G. Jug, A. Loidl, T. Kimura, and Y. Tokura, Phys. Rev. Lett. **95**, 257202 (2005).

[99]. R. M. Eremina, I. V. Yatsyk, Ya. M. Mukovskii, H. -A. Krug von Nidda, and A. Loidl, JETP Letters **85**, 51 (2007); I. V. Yatsyk, R. M. Eremina, Ya. M. Mukovskii, H. -A. Krug von Nidda, and A. Loidl, the International Conference "Modern Development of Magnetic Resonance"- Kazan, Russian Federation, 24-29, September (2007).

[100]. N. Rama, M. S. Ramachandra Rao, V. Sankaranarayanan, P. Majewski, S. Gepraegs, M. Opel, and R. Gross, Phys. Rev. B **70**, 224424 (2004).

[101]. Z. W. Ouyang, V. K. Pecharsky, K. A. Gschneidner Jr., D. L. Schlagel, and T. A. Lograsso, Phys. Rev. B **74**, 094404 (2006).

[102]. L. M. Rodriguez-Martinez and J. P. Attfield, Phys. Rev. B **54**, R15622 (1996).

[103]. J. P. Attfield, A. L. Kharlanov, and J. A. McAllister, *Nature,* **394**, 157 (1998).

[104]. J. H. Zhao, H. P. Kunkel, X. Z. Zhou, and G. Williams, J. Phys.: Condens. Matter. **13**, 5785 (2001).

[105]. H. L. Ju, J. Gopalakrishnan, J. L. Peng, Qi Li, G. C. Xiong, T. Venkatesan, and R. L. Greene, Phys. Rev. B **51**, 6143 (1995).

[106]. W. Li, H. P. Kunkel, X. Z. Zhou, G. Williams, Y. Mukovskii, and D. Shulyatev, Phys. Rev. B **70**, 214413 (2004).

[107]. K. Ghosh, C. J. Lobb, R. L. Greene, S. G. Karabashev, D. A. Shulyatev, A. A. Arsenov, and Y. Mukovskii, Phys. Rev. Lett. **81**, 4740 (1998); D. Kim, B. L. Zink, F. Hellman, and J. M. D. Coey, Phys. Rev. B **65**, 214424 (2002).

[108]. W. Li, H. P. Kunkel, X. Z. Zhou, G. Williams, Y. Mukovskii, and D. Shulyatev, J. Phys.: Condens. Matter. **16**, L109 (2004).

[109]. D. Kim, B. Revaz, B. L. Zink, F. Hellman, J. J. Rhyne, and J. F. Mitchell, Phys. Rev. Lett. **89**, 227202 (2002); C. P. Adams, J. W. Lynn, V. N. Smolyaninova, A. Biswas, R. L. Greene, W. Ratcliff, S-W. Cheong, Y. M. Mukovskii, and D. A. Shulyatev, Phys. Rev. B **70**, 134414 (2004); J. Lynn, R. Erwin, J. Borchers, Q. Huang, A. Santoro, J. Peng, and Z. Li, Phys. Rev. Lett. **76**, 4046 (1996).

[110]. E. Bozin, M. Schmidt, A. DeConinck, T. Chatterji, P. Radaelli, Th. Proffen, and S. Billinge, Phys. Rev. Lett. **98**, 137203 (2007);Y. Jiang, F. Bridges, L. Downward, and J. Neumeier, Phys. Rev. B **70**, 134414 (2007); C. H. Booth, F. Bridges, G. H. Kwei, J. M. Lawrence, A. L. Cornelius, and J. J. Neumeier, Phys. Rev. Lett. **80**, 853 (1998).

[111]. M. Hennion, F. Moussa, P. Lehouelleur, F. Wang, A. Ivanov, Y. M. Mukovskii, and D. Shulyatev, Phys. Rev. Lett. **94**, 057006 (2005).

[112]. Bas B. Van Aken, Oana D. Jurchescu, Auke Meetsma, Y. Tomioka, Y. Tokura, and T. T. M. Palstra, Phys. Rev. Lett. **90**, 066403 (2003).

[113]. S. N. Kaul, Phys. Rev. B **24**, 6550 (1981).

[114]. Y. Motome and N. Furukawa, J. Phys. Soc. Jpn. **68**, 3853 (1999), **69**, 3785, (2000), **70**, 1487, (2001); J. L. Alonso, L. A. Fernández, F. Guinea, V. Laliena, and V. Martín-Mayor, Nucl. Phys. B **596**, 587 (2001).

[115]. T. Brown, Wei Li, H. P. Kunkel, X. Z. Zhou, G. Williams, Y. Mukovskii, and A. Arsenov, J. Phys.: Condens. Matter. **17**, 5997 (2005).

[116]. P. Dai, J. A. Fernandez-Baca, E. W. Plummer, Y. Tomioka, and Y. Tokura, Phys. Rev. B **64**, 224429 (2001); P. Dai, J. A. Fernandez-Baca, N. Wakabayashi, E. W. Plummer, Y. Tomioka, and Y. Tokura, Phys. Rev. Lett. **85**, 2553 (2000); F. Ye, P. Dai, J. A. Fernandez-Baca, H. Sha, J. Lynn, H. Kawano-Furukawa, Y. Tomioka, Y. Tokura, and J. D. Zhang, Phys. Rev. Lett. **96**, 047204 (2006).

[117]. F. Keffer, *Spin Waves* (Handbuch der Physik, VIII/2) (Springer, Berlin, 1966).

[118]. W. Jiang, X. Zhou, G. Williams, Y. Mukovskii, and K. Glazyrin, Phys. Rev. B **78**, 144409 (2008).

[119]. C. Lin and A. J. Millis, Phys. Rev. B **78**, 174419 (2008).

[120]. V. Markovich, I. Fita, R. Puzniak, M. I. Tsindlekht, A. Wisniewski, and G. Gorodetsky, Phys. Rev. B **66**, 094409 (2002); P. Mandal and B. Ghosh, Phys. Rev. B **68**, 014422 (2003); V. Markovich, G. Jung, Y. Yuzhelevski, G. Gorodetsky, A. Szewczyk, M. Gutowska, D. A. Shulyatev and Ya. M. Mukovskii, Phys. Rev. B **70**, 064414 (2004).

[121]. B. I. Belevtsev, G. A. Zvyagina, K. R. Zhekov, I. G. Kolobov, E. Yu. Beliayev, A. S. Panfilov, N. N. Galtsov, A. I. Prokhvatilov, and J. Fink-Finowicki, Phys. Rev. B **74**, 054427 (2006).

[122]. P. Tong, Bongju Kim, Daeyoung Kwon, T. Qian, Sung-Ik Lee, S-W. Cheong, and Bog G. Kim, Phys. Rev. B **77**, 184432 (2008).

[123]. Z. Sun, J. F. Douglas, A. V. Fedorov, Y. -D. Chuang, H. Zheng, J. F. Mitchell, and D. S. Dessau, *Nature Physics*, **3**, 248 (2007).

[124]. V. Laukhin, B. Martínez, J. Fontcuberta, and M. Mukovskii, Phys. Rev. B **63**, 214417 (2001).

[125]. R. Laiho, K. G. Lisunov, E. Lähderanta, M. A. Shakhov, V. N. Stamov, V. S. Zakhvalinskii, V. L. Kozhevnikov, I. A. Leonidov, E. B. Mitberg, and M. V. Patrakeev, J. Phys.: Condens. Matter. **17**, 3429 (2005); P. Mandal and B. Ghosh, Phys. Rev. B **68**, 014422 (2003); R. I. Zainullina, N. G. Bebenin, A. M. Burkhanov, V. V. Ustinov, and M. Mukovskii, J. Alloys. Comp. **394**, 39, (2005); S. N. Barilo, G. L. Bychkov, L. A. Kurnevich, S. V. Shiryaev, L. A. Kurochkin, J. W. Lynn, and L Vasiliu-Doloc, J. Cryst. Growth. **211,** 480 (2000); N. Moutis, I. Panagiotopoulos, M. Pissas, and D. Niarchos, Phys. Rev. B **59**, 1129 (1999).

[126]. T. Chatterji, L. P. Regnault, and W. Schmidt, Phys. Rev. B **66**, 214408 (2002).

[127]. S. J. L. Billinge, R. G. DiFrancesco, G. H. Kwei, J. J. Neumeier, and J. D. Thompson, Phys. Rev. Lett. **77**, 715 (1996).

[128]. A. S. Alexandrov and A. M. Bratkovsky, Phys. Rev. Lett. **82**, 141 (1999); Phys. Rev. Lett. **96**, 117003 (2006); J. Phys. Condens. Matter. **11**, 1989 (1999).

[129]. M. Egilmez, K. H. Chow, and J. Jung, Appl. Phys. Lett. **92**, 162515 (2008).

[130]. F. Rivadulla, M. Otero-Leal, A. Espinosa, A. de Andrés, C. Ramos, J. Rivas, and J. B. Goodenough, Phys. Rev. Lett. **96**, 016402 (2006).

[131]. H. Yoshizawa, H. Kawano, Y. Tomioka, and Y. Tokura, Phys. Rev. B **52**, R13145 (1995); Y. Tomioka, A. Asamitsu, H. Kuwahara, Y. Moritomo, and Y. Tokura, Phys. Rev. B **53**, R1689 (1996).

[132]. V. Kiryukhin, D. Casa, J. P. Hill, B. Keimer, A. Vigliante, Y. Tomioka, and Y. Tokura, *Nature,* **386**, 813 (1997).

[133]. A. Asamitsu, Y. Tomioka, H. Kuwahara, and Y. Tokura, *Nature*, **388**, 50 (1997).

[134]. K. Miyano, T. Tanaka, Y. Tomioka, and Y. Tokura, Phys. Rev. Lett. **78**, 4257 (1997).

[135]. A. M. L. Lopes, J. P. Araújo, V. S. Amaral, J. G. Correia, Y. Tomioka, and Y. Tokura, Phys. Rev. Lett. **100**, 155702 (2008).

[136]. R. Kajimoto, H. Mochizuki, H. Yoshizawa, S. Okamoto, and S. Ishihara, Phys. Rev. B **69**, 054433 (2004); L. M. Fisher, A. V. Kalinov, I. F. Voloshin, N. A. Babushkina, K. I. Kugel, and D. I. Khomskii, Phys. Rev. B **68**, 174403 (2003).

[137]. W. Lee, S. Watauchi, V. Miller, R. Cava, and N. Ong, *Science,* **303**, 1647 (2004); J. Stankiewicz and K. P. Skokov. Phys. Rev. B **78**, 214435 (2008).

[138]. C. Zeng, Y. Yao, Q. Niu, and H. Weitering, Phys. Rev. Lett. **96**, 037204 (2006).

[139]. S. H. Chun, Y. S. Kim, H. K. Choi, I.T. Jeong, W. O. Lee, K. S. Suh, Y. S. Oh, K. H. Kim, Z. G. Khim, J. C. Woo, Y. D. Park, Phys. Rev. Lett. **98**, 026601 (2007).

[140]. G. Mihály, M. Csontos, S. Bordács, I. Kézsmárki, T. Wojtowicz, X. Liu, B. Jankó, and J. K. Furdyna, Phys. Rev. Lett. **100**, 107201 (2008).

[141]. Stolichnov, S. W. E. Riester, H. J. Trodahl, N. Setter, A. W. Rushforth, K. W. Edmonds, R. P. Campion, C. T. Foxon, B. L. Gallagher and T. Jungwirth, *Nature Materials*, **7**, 464 (2008).

[142]. H. X. Tang, R. K. Kawakami, D. D. Awschalom, and M. L. Roukes, Phys. Rev. Lett. **90**, 107201 (2003).

[143]. B. L. Sheu, R. C. Myers, J.-M. Tang, N. Samarth, D. D. Awschalom, P. Schiffer, and M. E. Flatté, Phys. Rev. Lett. **99**, 227205 (2007).

[144]. P. A. Lee and T. V. Ramakrishnan, Rev. Mod. Phys. **57**, 287 (1985).

[145]. J. Kondo, Prog. Theor. Phys. **32,** 37 (1962).

[146]. H. He, C. Yang, W. Ge, J. Wang, X. Dai, and Y. Q. Wang, Appl. Phys. Lett. **87**,162506 (2005).

[147]. M. J. Press and F. T. Hedgcock, Phys. Rev. Lett. **23**, 167 (1969).

[148]. D. Neumaier, K. Wagner, S. Geißler, U. Wurstbauer, J. Sadowski, W. Wegscheider, and D. Weiss, Phys. Rev. Lett. **99**, 116803 (2007).

[149]. R. W. Cochrane, and J. O. Strom-Olsen, Phys. Rev. B **29**, 1088 (1983).

[150]. M. E. Fisher, S.-K. Ma, and B. G. Nickel, Phys. Rev. Lett. **29**, 917 (1972).

[151]. W. Jiang, A.Wirthmann, Y. S. Gui, X. Zhou, M. Reinwald, W. Wegscheider, C.-M. Hu, and G. Williams, Phys. Rev. B **80**, 214409 (2009).

[152]. E. Dagotta, New J. Phys. **7**, 67 (2005).

[153]. J. Tao, D. Niebieskikwiat, M. Varela, W. Luo, M. Schofield, Y. Zhu, M. Salamon, J. Zuo, S. Pantelides, and S. Pennycook, Phys. Rev. Lett. **103**, 097202 (2009).

Publication List:

Papers listed below are discussed in the **Chapter 4**:

1. Mechanisms Underlying Ferromagnetism Across the Compositional Metal-Insulator Transition in $La_{1-x}Ca_xMnO_3$
   Wanjun Jiang, Xuezhi Zhou, Gwyn Williams, Y. Mukovskii, and R. Privezentsev
   Physical Review B, 79, 214433 (2009).
2. The evolution of Griffiths-phase-like features and colossal magnetoresistance in $La_{1-x}Ca_xMnO_3$ ($0.18 \leq x \leq 0.27$) across the compositional metal-insulator boundary
   Wanjun Jiang, Xuezhi Zhou, Gwyn Williams, Y. Mukovskii, and R. Privezentsev
   Journal of Physics: Condensed Matter, 21, 415603 (2009).
3. Correlation between the Nucleation of a Griffiths-like Phase and Colossal Magnetoresistance Across the Compositional Metal-Insulator Boundary in $La_{1-x}Ca_xMnO_3$
   Wanjun Jiang, Xuezhi Zhou, Gwyn Williams, Y. Mukovskii, and R. Privezentsev
   Journal of Physics: Conference Series, 200, 012072 (2010).
4. Coexistence of Colossal Magnetoresistance, a Griffiths-Like Phase, and a Ferromagnetic Insulating Ground State in Single Crystal $La_{0.73}Ba_{0.27}MnO_3$
   Wanjun Jiang, Xuezhi Zhou, Gwyn Williams, Y. M. Mukovskii, and R. Privezentsev
   Journal of Applied Physics, 107 09D701 (2010).
5. Griffiths Phase and Critical Behaviour in Single Crystal $La_{0.7}Ba_{0.3}MnO_3$: Phase Diagram for $La_{1-x}Ba_xMnO_3$, $x \leq 0.33$
   Wanjun Jiang, Xuezhi Zhou, Gwyn Williams, Y. M. Mukovskii, and K. Glazyrin
   Physical Review B, 77, 064424 (2008).
6. Critical Behavior and Transport Properties of Single Crystal $Pr_{1-x}Ca_xMnO_3$ (x=0.27; 0.29)
   Wanjun Jiang, Xuezhi Zhou, Gwyn Williams, Y. M. Mukovskii, and K. Glazyrin
   Physical Review B, 78, 144409 (2008).
7. Correlation Between Phase Competition and the Nucleation of a Griffiths-like Phase in $(La_{1-y}Pr_y)_{0.7}Ca_{0.3}Mn^{16/18}O_3$
   Wanjun Jiang, Xuezhi Zhou, and Gwyn Williams
   Europhysics Letters, 84, 47009 (2008).

8. Extreme Sensitivity of the Griffiths Phase to Field in Single Crystal $La_{0.73}Ba_{0.27}MnO_3$
   Wanjun Jiang, Xuezhi Zhou, Gwyn Williams, Y. M. Mukovskii, and K. Glazyrin
   Physical Review B, 76, 092404 (2007).
9. Is a Griffiths Phase a Prerequisite for Colossal Magnetoresistance?
   Wanjun Jiang, Xuezhi Zhou, Gwyn Williams, Y. M. Mukovskii, and K. Glazyrin
   Physical Review Letters, 99, 177203 (2007).

Papers listed below are discussed in the **Chapter 5**:

10. Critical Behavior from the Anomalous Hall Effect in (GaMn)As
    Wanjun Jiang, André Wirthmann, Y. S. Gui, X. Z. Zhou, M. Reinwald, W. Wegscheider, C.-M. Hu, and Gwyn Williams
    Physical Review B, 80, 214409 (2009).
11. Scaling the Anomalous Hall Effect
    Wanjun Jiang, Xuezhi Zhou, Gwyn Williams
    Under Review (2010).

Other papers listed below are not covered in this thesis:

12. Field-dependent ac susceptibility of Ce_2Fe_{17}
    Xuezhi Zhou, **Wanjun Jiang**, and Gwyn Williams
    Journal of Physics: Condensed Matter, 21, 026018 (2009).
13. Entropy changes accompanying the magnetic phase transitions in low Si-doped $Ce_2Fe_{17-x}Si_x$ Alloy
    Xuezhi Zhou, **Wanjun Jiang**, Henry Kunkel, and Gwyn Williams
    Journal of Magnetism and Magnetic Materials, 320, 930 (2008).
14. Anomalous Field Dependence of the Inverse Magnetocaloric Effect in $Ce(Fe_{0.93}Ru_{0.07})_2$
    Wanjun Jiang, Xuezhi Zhou, Henry Kunkel, and Gwyn Williams
    Journal of Magnetism and Magnetic Materials, 320, 2144 (2008).